DISSERTATION

CONSTRAINTS ON THE GALACTIC MAGNETIC FIELD WITH TWO-POINT CUMULATIVE AUTOCORRELATION FUNCTION

Submitted by

Yevgeniy Petrov

Department of Physics

In partial fulfillment of the requirements

For the Degree of Doctor of Philosophy

Colorado State University

Fort Collins, Colorado

Spring 2012

Doctoral Committee:

Advisor: John L. Harton

Miguel A. Mostafá
Bruce Berger
Patrick J. Burns

ABSTRACT

CONSTRAINTS ON THE GALACTIC MAGNETIC FIELD WITH TWO-POINT CUMULATIVE AUTOCORRELATION FUNCTION

The fact that ultra high energy cosmic rays are charged particles complicates identification of their sources due to deflections by the intervening cosmic magnetic fields. The information about the fields is encoded in the amount of deflection experienced by a charged particle. Unfortunately, the positions of sources are unknown as is the structure of the magnetic field. However, it is possible to deduce the most favorable galactic magnetic field by examining the parameter space of different models of the GMF. The method presented in this work is valid under some plausible assumptions, such as extragalactic origin of the UHECR, pure protonic composition above 50 EeV and sufficiently weak randomly oriented galactic and extragalactic components of the magnetic field. I use a two point cumulative autocorrelation function combined with the backtracking method to find regions in the parameter space that are compatible with statistically significant clustering on the extragalactic sky. This approach is independent of any catalog of sources. The ratio between the number of pairs within a certain angular window at the Earth sky and at the extragalactic sky after backtracking serves to indicate focusing or de-focusing properties of a particular field configuration. The results suggest that among several tested fields, the Harari-Mollerach-Roulet model with a bi-symmetric spiral and even vertical symmetry favors clustering of arrival directions at the extragalactic sky with the probability of 2.5% being from an isotropic distribution. Addition of the toroidal halo field improves clustering for the Harari-Mollerach-Roulet field for both bi-symmetric and axisymmetric spirals with even vertical symmetry, and the isotropic probabilities are 2.5% and 5.3% correspondingly. The bi-symmetric and axisymmetric spirals with odd vertical symmetry are disfavored, as well as the models with annular structure.

TABLE OF CONTENTS

Chapter 1

Ultra High Energy Cosmic Rays

1.1 Discovery of Cosmic Rays and History of Their Studies

One of the first appearances of the term "cosmic rays" was in the book by an American naturalist and philosopher Stanton Davis Kirkham "The ministry of beauty," published in 1905, where it says, "To be wise and kind is to enlist the universe in our behalf, to focus *cosmic rays* of love in our hearts" [1]. The term would however change its meaning soon from being a metaphor to a pure scientific one.

At the beginning of the 20th century, experiments with electroscopes inside fully sealed glass containers revealed that they were discharging. In 1903, British physicists McLennan and Burton [2], and Rutherford and Cooke [3] reported that leakage of a sealed electroscope could be noticeably reduced by surrounding it with metal walls several centimeters thick. Thus, radioactivity, which just had been discovered 10 years before that, was the first candidate to blame. However, several studies by Theodor Wulf, Domenico Pacini, Victor Hess and Werner Kolhrster showed that it was not the case. Victor Hess, especially, showed in a series of careful balloon experiments that the ionization levels decreased as a function of altitude up to 1 km but then started increasing again, at 5 km becoming as much as four times larger than the value at the sea level [4]. He proposed that the ionization was caused by highly penetrating

particles coming from the outer space. For this work Hess was later awarded a Nobel prize for the discovery of what we now know as cosmic rays.

In 1925 Millikan published a paper [5] in which he introduced the term "cosmic rays" for the first time referring to the highly penetrating radiation of cosmic origin. He made measurements of the air ionization rates in high altitude lakes in California at different altitudes, and the results showed that the ionization levels at different water depths in both lakes could be matched by taking into account the thickness of the atmosphere corresponding to the altitude difference between the lakes. Thus he unambiguously proved that air ionization was caused by some radiation coming from above and could not be attributed to any sources of natural radioactivity in the soil or in the layer of atmosphere under consideration.

With the development of more advanced experimental tools such as cloud chambers, Geiger counters and nuclear emulsions the existence of different kind of particles with different energies bombarding the Earth's atmosphere was beyond any doubt. In the 1930s Bruno Rossi and Pierre Auger independently discovered that sometimes signals from Geiger counters triggered by cosmic rays happen in coincidence even if the counters are separated by significant distances in the horizontal plane. After some detailed investigation, Auger came to conclusion that the phenomenon is explained by an extensive air shower (EAS) generated by a high-energy primary cosmic ray at the top of the Earth's atmosphere. The cosmic ray would disintegrate an air nucleus at the top of the atmosphere, producing a cascade of secondary interactions that ultimately yield a shower of electrons, photons, and muons that reach ground level at the same time making coinciding signals in the Geiger counters.

It is interesting to note that scientists from Colorado were also involved in the cosmic ray research of the 1930s when Dr. Joyce B. Stearns and Dr. Fred D'Amour

Figure 1.1 Early laboratory to study cosmic rays on top of Mt. Evans, Colorado. Taken from [6].

of the University of Denver built a laboratory on top of Mt. Evans which was completely screened with copper sheets all connected to the cable anchored into the rock underneath to make a Faraday cage. They used Geiger counters for detection and also studied the effect of cosmic rays on living organisms observing a population of white rats which they brought to the observatory. Figure 1.1 shows a photo from Popular Science [6] of how it looked in 1936.

Cosmic rays with their relatively high energies were used by particle physicists until the first accelerators were built in the 1950s which provided well-defined beam energies. Since then, cosmic ray physics has concentrated on studying fundamental questions of the origin and composition of cosmic rays as well as the limit of their energy. The flux of cosmic rays falls approximately three orders of magnitude as their energy increases by one order of magnitude which makes it significantly harder, and at

the highest energies, even impossible to study primary cosmic rays directly. Therefore detection of the EAS was the next stage in the development of the experimental techniques.

The first detector of EAS was built in New Mexico, USA. It was called *Volcano Ranch* [7]. The detector was composed of an array of nineteen scintillators with an area of 3.3 m^2 each. The array had a hexagonal shape and the total area of 8 km^2. The very first EAS with energy more than 10^{20} eV was detected by Volcano Ranch. After Volcano Ranch several more ground arrays were built in different countries with larger areas and constantly improving electronics. They were *SUGAR* in Australia [8], *Haverah Park* in England [9], *Yakutsk* in the Soviet Union [10] and the largest of its time, *AGASA*, in Japan [11].

It turns out that the cascade of particles is not the only effect which the primary particle initiates in the atmosphere. The electromagnetic component of an EAS consiting of electron-positron pairs and gamma rays causes nitrogen in the atmosphere to excite along the shower axis. The nitrogen then fluoresces as ultraviolet light which could be detected by a telescope on a moonless dark night. This type of detection technique has been in use since the early 1980s when it was pioneered by the *Fly's eye* [12] project which evolved into *HiRes* experiment [13].

Nowadays, both techniques are combined together in hybrid detectors such as *Pierre Auger Observatory* [14], which is currently operating in the southern hemisphere in Argentina, and *Telescope Array* in the northern hemisphere [15]. I use the dataset collected by the Pierre Auger Observatory in the current work. The descripition of the observatory is given in Chapter 2.

1.2 Main Aspects of Cosmic Ray Physics

1.2.1 Energy Spectrum and Composition

Cosmic rays are truly universal and complex phenomenon which reflect processes happening in cosmos in a broad range of spatial, time and energy scales. This fact finds its confirmation in the energy spectrum of cosmic rays which spans over 14 orders of magnitude with the lowest energies of 10^8 - 10^9 eV attributed to solar flares, and the highest ones, at 10^{20} eV, still being a mystery. The composition of cosmic rays depends on the energy and is well known in the energy region where direct measurements are possible, up to 10^{15} eV. Let us now review what is known about cosmic rays across this broad energy range.

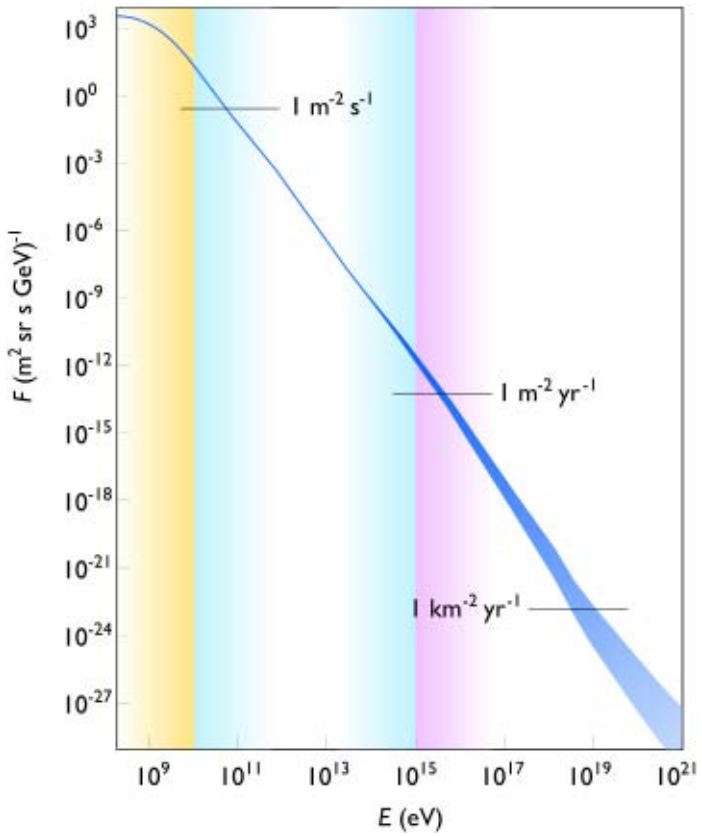

Figure 1.2 Cosmic ray energy spectrum. Source: Wikipedia

Figure 1.2 shows the energy spectrum of cosmic rays in the form of differential flux expressed in number of particles per m^2 per second per steradian per energy per nucleon. The spectrum is approximately a power law with the spectral index of 2.7. The majority of particles come from the solar activity at about 1 GeV and the flux is about 1000 particles$\cdot m^{-2} \cdot s^{-1} \cdot sr^{-1}$. At this energy 90% of the cosmic rays are protons, 9% are helium nuclei and the rest are electrons and heavier nuclei.

From 1 GeV and up to 10^6 GeV the spectrum continues without any features with the spectral index of 2.7-2.75. After the initial bulk of solar cosmic rays at the lowest energies, the rest of the spectrum in this region of energies consists of the galactic cosmic rays, most probably accelerated in the shock fronts of supernova remnants (SNR) [16]. The spectral index changes to about 3.1 at about 1-3$\times 10^6$ GeV. This feature in the spectrum is called "knee" and has been measured by many experiments. At about these energies the flux drops to 1 particle$\cdot m^{-2} \cdot year^{-1} \cdot sr^{-1}$ so that direct measurements, such as ballon and satellite experiments, become impossible due to low statistics. Figure 1.3 shows the compilation of the measurements by different experiments. As one can see the last data point from the direct experiment is at about 10^{15} eV, all the data at higher energies come from air shower experiments (see details about air showers in the next subsection). Unfortunately, differences in the energy estimates between different experiments lead to the difference in the measured flux up to a factor of two. As can be seen on the figure, the exact position on the energy scale where the transition happens also varies from experiment to experiment as well as the shape.

The most common theoretical explanation for the appearance of the "knee" is based on the assumption that cosmic rays are accelerated in the shocks of SNR. As reviewed in [17] there are many works [18–22] suggesting that the maximum energy of the particles with charge Z is limited by the lifetime of the shock front, and turns

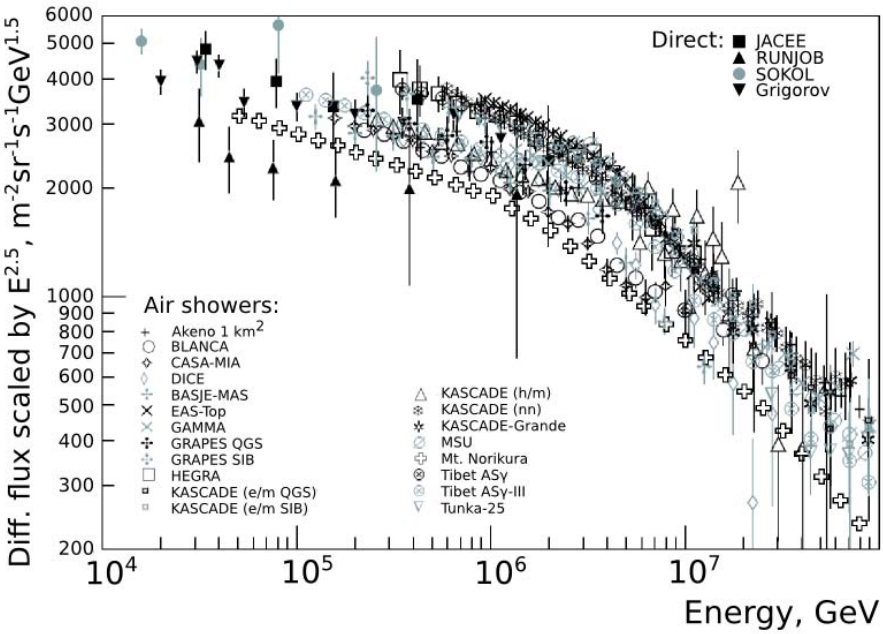

Figure 1.3 Knee region of the cosmic ray spectrum. The flux is multiplied by $E^{2.5}$ to make features more pronounced. Adapted from [17]

out to be in the following range: $E_{max} \approx Z(0.1-5) \times 10^{15}$ eV. Heavier elements reach the cutoff later than lighter ones due to magnetic confinement and that leads to the steepening of the spectrum. An example from [22] is given in the Figure 1.4, where the knee appears at about $2-3 \times 10^{15}$ eV as the result of adding contributions from different nuclei. According to the model in [22] the knee is explained by acceleration of different nuclei in some particular types of supernovae, namely SNIbc1, SNIIn.[1] The character of propagation of different nuclei through the Galaxy might contribute as well. As the energy increases cosmic rays start leaking from the Galaxy depending on their energy and the magnitude of the galactic magnetic field. Lighter nuclei escape first followed by heavier nuclei so that the net effect can produce the shape of the knee [23–27]. For comprehensive reviews of the status of the studies of the "knee" region see [17, 28].

[1]Supernovae of type Ibc1 are the brightest. Type IIn is for supernovae that are very bright in the ultraviolet part of the spectrum.

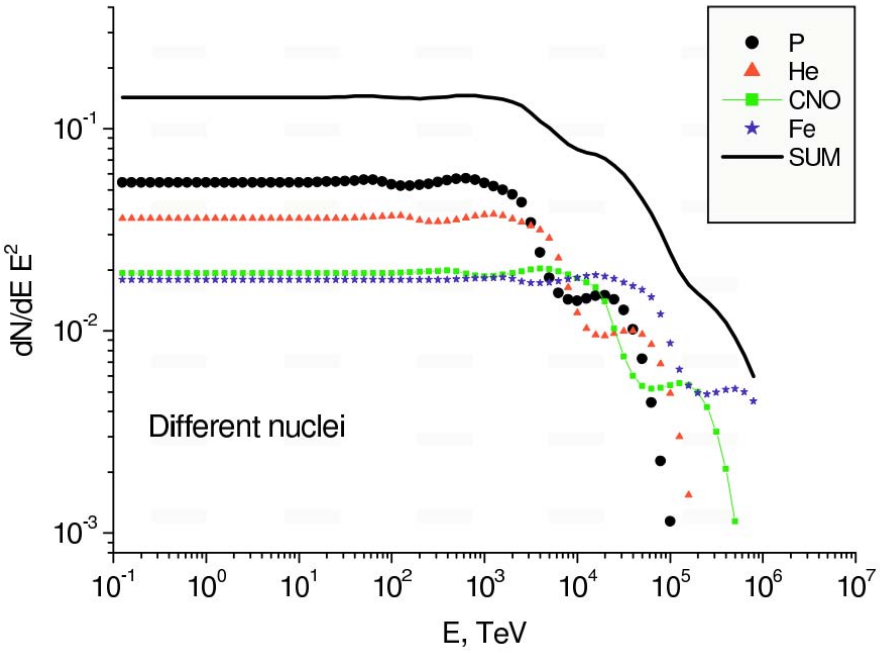

Figure 1.4 Spectra of different cosmic ray nuclei. Taken from [22]

Let us now move on in energy and consider what happens after the knee. If the scenarios described above are valid, the galactic component of cosmic rays is predicted to end from 30 to $92 \times E_{p,cut}$, where $E_{p,cut}$ is the cut-off energy of protons, $\approx 3.0 \times 10^{15}$ eV. The higher value is obtained if super heavy stable elements are included as it is done in [29]. The presence of a so-called "second knee" in the spectrum motivates such kind of theoretical studies. The second knee is located at about 4×10^{17} eV, where the spectrum steepens slightly more. Besides the explanation that galactic accelerators run out of power, there is an alternate explanation for the second knee and a dip in the spectrum right after it by Berezinsky et al. in [30, 31]. The model requires proton dominance in the composition. Protons, and cosmic rays in general, in this energy region are believed to be of the extragalactic origin. Protons at 10^{17}-10^{19} eV lose their energy through two mechanisms: adiabatic losses due to expansion of the Universe and electron-positron pair production when interacting with photons

from the cosmic microwave background. The maximum loss is at about 2×10^{18} eV which explains the dip and the steepening at the second knee before that.

Finally, the end of the cosmic ray spectrum as it has been measured upto now is located at energies of 10^{18} eV and above, with only handful of events above 10^{20} eV. The statistics in this energy range become as low as 1 particle$\cdot$km$^{-2}\cdot$year$^{-1}\cdot$sr^{-1} at 10^{18} eV and even 1 particle$\cdot$km$^{-2}\cdot$century$^{-1}\cdot$sr^{-1} above 10^{20} eV. The cosmic rays in this energy range are called ultra-high energy cosmic rays (UHECRs), and analysis of their arrival directions and energies with connection to their propagation in the cosmic magnetic fields is the topic of the current dissertation. UHECR energy is usually expressed in the units of EeV = 10^{18} eV.

The spectrum (taken from [17]) scaled by E^3 is shown on the Figure 1.5. It has been measured by several experiments: AGASA, Yakutsk, HiRes and the Pierre Auger Observatory; among which the Pierre Auger Observatory has the largest exposure and is currently the only one collecting data. As can be seen there is a discrepancy which is due to the difference in the energy scale of the experiments. All of the spectra from the experiments above can be brought into agreement by proper rescaling as shown on the right plot of the figure. After such a procedure one can see that all spectra have a very similar shape up to $\approx$30 EeV. There is a dip in the spectrum between 1 and 10 EeV and then the spectrum flattens making a feature which is called the "ankle".

The UHECR domain of energies is in a region where we know little about their origins and composition. It is generally believed that UHECRs come from extra-galactic sources since the galactic accelerators are not capable of accelerating to such high energies as discussed above. Interactions of both protons and heavier nuclei with the cosmic microwave background, in which they lose energy as they propagate in intergalactic space, lead to the conclusion that the cosmic ray spectrum should

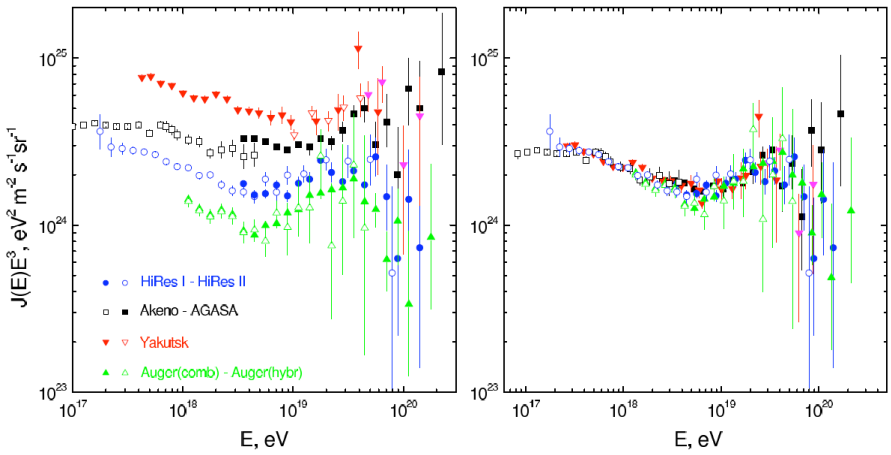

Figure 1.5 The end of the cosmic ray spectrum. Taken from [17]

not extend beyond 10^{20} eV (see section 1.4 below for details). The flux suppression has not been seen by AGASA as one can see on the Figure 1.5. However, HiRes and more recently Pierre Auger Observatory confirm existence of the flux suppression with higher statistics. It is however still unclear if this suppression is due to the pure propagation effect, the GZK cutoff (see section 1.4 below), or is it due to the extragalactic sources running out of power, or it could be the combined effect.

The composition of UHECR is not known. There is however an indication in the recent results by the Pierre Auger Observatory that the composition becomes heavier starting from 3 EeV. The difficulties of determining both the energy and composition come from the necessity of making indirect measurements via detection of the air showers of secondary particles in the atmosphere and also of having to rely on simulations of particle interactions in the air in the energy range where the cross-sections have to be extrapolated from lower energies, where they have been measured at accelerators. The next sections gives the details of the air shower physics.

1.2.2 Extensive Air Showers

An extensive air shower (EAS) starts at the altitudes of 15 – 35 kilometers when a cosmic ray particle interacts with a nucleus in the Earth's atmosphere. A shower could be purely electromagnetic if it was initiated by a gamma ray or it could be hadronic when started by a nucleon or a heavier nucleus. A cascade process starts after the first interaction as more and more nuclei disintegrate into secondary particles. The secondary particles include baryons, charged and neutral pions, and charged kaons. Two components of the shower start developing at this stage: electromagnetic and hadronic unless the shower has been initiated by a gamma-ray. The shower develops in both lateral and longitudinal directions with respect to the velocity direction of the initial particle. A useful quantity, called slant depth or column density or atmospheric depth, is introduced for the analysis of how the density of the secondary particles changes laterally and longitudinally. The slant depth is defined as an integral of the atmospheric density, ρ, along the shower trajectory l: $\int \rho(l)dl$. It is usually measured in g/cm^2.

Let us consider the electromagnetic phenomena first which describe the electromagnetic parts of the hadronic showers and showers initiated by gamma rays. Neutral pions have a very short lifetime of 8.4×10^{-17}s, and so they cannot travel more than several micrometers even in the laboratory frame with the special relativity time delay accounted for. Neutral pions decay via an electromagnetic interaction into a pair of gamma rays or a gamma ray and an electron-positron pair ($\approx$2% branching ratio). Gammas, electrons and positrons continue the electromagnetic cascade until their energy drops below some critical energy, E_c, when the corresponding cross-sections become zero: pair-production cross-section for gamma rays and bremsstrahlung cross-section for electrons and positrons. On each generation new neutral pions are produced in the hadronic interactions and then add to the electromagnetic component

by decaying.

A simple cascade model was suggested in the 1930s in [32, 33], it is called the Heitler model. After traveling one interaction length λ (measured in units of g/cm^2), a particle with energy E_0 is converted into two particles of the same type each carrying half of the original energy. They travel for another interaction length, produce 4 particles and so on. The cascade keeps growing until the energy of each particle becomes equal to the critical energy, and therefore the maximum number of particles is $N_{max} = E_0/E_c$. The number of particles, N, in any generation at some depth X then equals to $2^{X/\lambda}$. It then follows that the atmospheric depth where the maximum happens can be simply written as $X_{max}^{(e.m.)} = \lambda \log_2(E_0/E_c)$. This simple model does not describe what happens after the maximum has been reached although it turns out that more elaborate models based on the solutions of the transport equations [34] or Monte Carlo simulations [35] confirm the results above that the number of particles at the maximum is proportional to the energy of the primary particle, and that the depth of the maximum depends logarithmically on the primary energy.

Another important point regarding the electromagnetic component of EAS is that it carries away approximately 90% of the primary energy [36] and then deposits it in the atmosphere via ionization processes. As reviewed in [37], one can understand what happens in the following way: most of the particles, which are born in the hadronic processes of a shower, are two charged and one neutral pion. Thus, after decaying, neutral pions transfer one third of the energy to the electromagnetic component, and another third of the energy left in the hadronic part will be transfered after the next interaction and so on. Therefore after n generations the fraction of the energy transferred into the electromagnetic component will be $(1 - (2/3)^n)$. It is shown in [38] that charged pions decay into muons after 5-6 interactions when their energy becomes insufficient to travel more in the lab frame. Plugging 5-6 in the fraction

above we can see that the fraction of the electromagnetic energy varies between 87% and 91%. Details of how the electromagnetic energy is deposited in the atmosphere and how the fluorescence detectors of the Pierre Auger Observatory collect it will be given below in Chapter 2.

The hadronic part of an extensive air shower is another important component which not only feeds the electromagnetic part as explained above but also determines the number of muons that ultimately reach the ground and get detected by a ground array. The hadronic cascade starts with the first interaction where the primary nucleon or nucleus losses about 50% of its energy (see [39] and [40, p. 38])in an inelastic collision and produces secondary hadrons, mostly charged and neutral pions and kaons. Charged pions and kaons produce more hadronic cascades until their energy becomes low enough so that they do not have time to produce more cascades and decay into muons and neutrinos (charged kaons decay into charged pions as well). As described above, the charged pions interact 5-6 times producing next cascades and then decay into muons.

Generalization of the simple model for electromagnetic showers has been done for hadronic showers in [41]. The energy of a nucleon before interaction is divided between n_{sec} secondary particles. Since approximately 2/3 of the secondary particles are charged pions the fraction of the primary energy left in the hadronic component after n generations is $(2/3)^n$. The number of muons in the shower is parametrized as $N_\mu = (E_0/\epsilon_\pi)^\beta$ where ϵ_π and β are effective parameters related to the energy and multiplicity of the charged pions. Details of how the muonic and electromagnetic components are detected by means of the surface detectors of the Pierre Auger Observatory will be given in Chapter 4.

The electromagnetic component determines the depth of the maximum for the case of hadronic showers too. In the simple view of the Heitler model only the first

generation neutral pions is considered. The primary nucleon loses 50% of its energy and produces n_{sec} particles (pions) so the energy per pion after the first interaction is $E_0/(2n_{sec})$ and approximately one can write (see [41]) the expression for the depth of the maximum as

$$X_{max}^{(had.)} \approx \lambda_{had} + X_0 \ln\left(\frac{E_0}{2n_{sec}E_c}\right), \tag{1.1}$$

where X_0 is called the radiation length, and it is the amount of matter in g/cm^2 traveling over which an electron loses 1/e of its energy through bremsstrahlung. X_0=37 g/cm^2 for air. λ_{had} is the hadronic interaction length. So qualitatively the $X_{max}^{(had.)}$ behavior does not change for hadronic showers and is still proportional to the logarithm of the primary energy.

Summarizing, the picture of the development of an extensive air shower is shown on the Figure 1.6.

1.2.3 Air Fluorescence and Cherenkov Light from Extensive Air Showers

Another very important aspect of the shower development in the atmosphere is transfer of energy from the electromagnetic component of the shower into fluorescence and Cherenkov radiation. Charged particles of the shower (mostly electrons and positrons) excite nitrogen molecules in the atmosphere which then de-excite by emitting fluorescence light in the ultraviolet part of the spectrum between 300 and 430 nm. The number of emitted photons is proportional to the energy deposited in the atmosphere [42]. Another important property of the fluorescence light is that it is emitted in an isotropic manner, and that allows one to collect the light by looking from the side and observing a large volume of the atmosphere with a wide angle telescope.

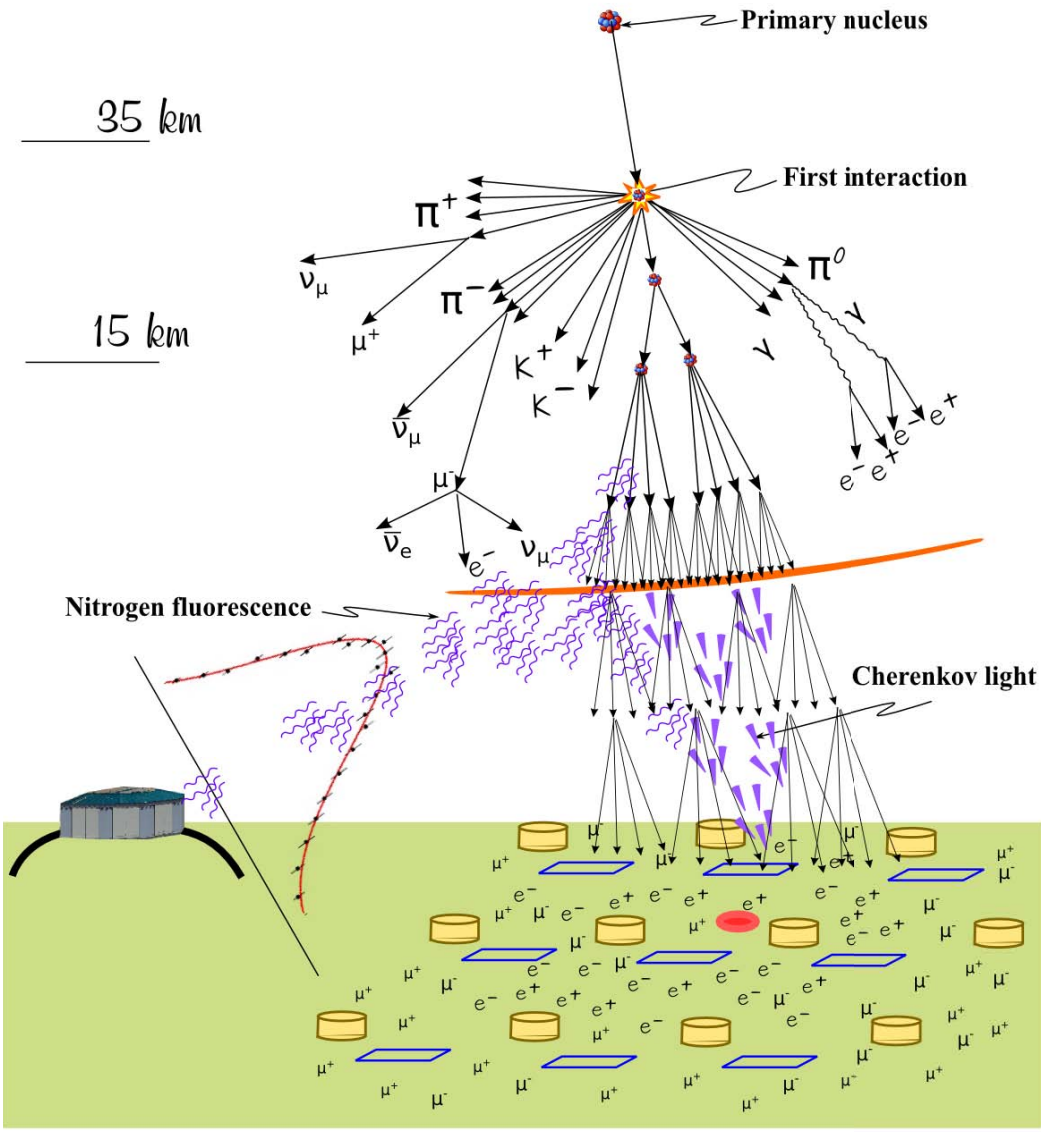

Figure 1.6 An extensive air shower and its detection with a hybrid technigue combining a fluorescence detecetor and an array of ground detectors. The shower core on the ground is depicted as a red spot.

If one detects all the fluorescent light emitted by the shower electromagnetic component along its axis, it is possible to make a nearly calorimetric measurement and calculate the total amount of the energy deposited in the atmosphere, which is then directly related to the energy of the primary particle. The only correction is that some of the primary energy is carried away by the hadronic component and neutrinos. This fraction decreases with the primary energy since the increased energy of the secondary mesons allows them to last longer in the lab frame and therefore they tend to interact instead of decaying. The fraction becomes approximately 10% at energies above 1 EeV [40].

It is also important to monitor atmospheric conditions at the time of measurement since one needs to know the transmission properties of the atmosphere as well as the so called fluorescence yield, which is defined as the number of photons emitted per unit wavelength per energy loss by charged particles. The yield depends on the temperature, pressure and humidity of the air, and the transmission includes effects of optical absorption, Rayleigh scattering and Mie scattering. The absolute fluorescence yield in air could be estimated to be ≈ 5 photons per MeV of energy deposited at normal conditions at 337 nm, at the peak of the nitrogen spectral output.

As the shower propagates in the atmosphere, Cherenkov light is emitted due to superluminal speed of the shower particles in the air. The Cherenkov light, as opposed to fluorescence light, has directionality. It has an opening angle, θ, with respect to the path of the particle which is related to the refractive index of the medium as $cos(\theta) = 1/(n\beta)$, where both n and β are very close to 1 in the case of air and ultra high energy showers. Thus, the Cherenkov light propagates in a direction close to the shower axis. By having an array of detectors on the ground one can register the light and measure the lateral distribution of the light on the ground, and from that it is possible to calculate X_{max} and the energy of the primary. See [43] for details.

Pierre Auger Observatory does not collect Cherenkov light directly in its telescope measurements. The biggest currently running experiment that collects Cherenkov light for detection of EAS is Tunka-133 in the Tunka valley in Siberia [44].

1.3 Origin of Ultra High Energy Cosmic Rays

With statistics so low at the highest energies, UHECR are measured by indirect observational techniques through detection of the extensive air showers (EAS) in the atmosphere. The cascade character of the shower and the presence of a clearly defined axis leaves no doubt that the showers are initiated by some single original particle which hits the upper layer of the atmosphere, but the nature of this original particle remains unknown. However, there are several plausible hypotheses and some are favored by recent measurement performed by the Pierre Auger Observatory [45–48].

There are two distinct approaches to explain the UHECR origin. One, which is called "bottom-up," describes a scenario in which cosmic rays are ordinary charged particles such as protons and heavier nuclei being accelerated in astrophysical sources. The other one is called "top-down." The latter scenario suggests that UHECR appear as the result of decay of so-called "exotic" particles, relics of the early Universe, such as topological defects or super heavy dark matter with rest masses as high as 10^{25} eV. The process of decay produces quarks and leptons. Quarks give birth to hadronic jets mainly consisting of pions and some amount of baryons. Pions, in turn, decay to UHE photons, neutrinos (or antineutrinos) and electrons (positrons). UHE (anti)neutrinos can annihilate with relic neutrinos (antineutrinos) producing so-called "Z bursts" which then decay to UHE photons and nucleons.

Recent results by the Pierre Auger Observatory set an upper limit on the UHE photon flux and photon fraction at EeV energies. The upper limits on the photon

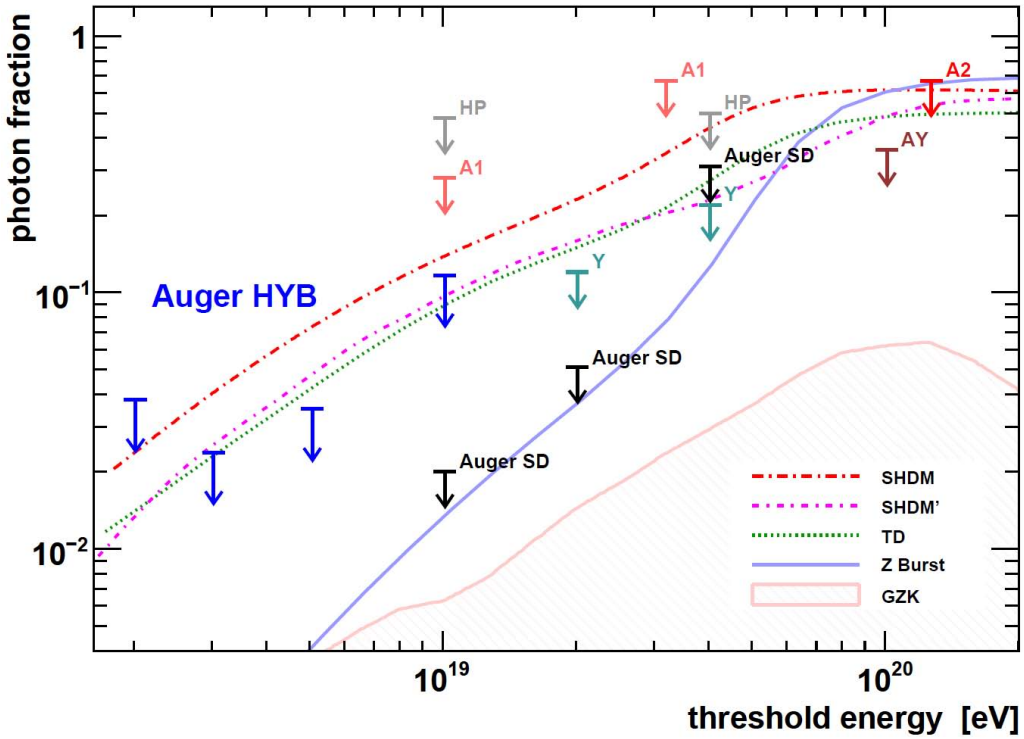

Figure 1.7 Upper limits on the photon fraction in the integral cosmic-ray flux for different experiments: AGASA (A1, A2) [50, 51], AGASA-Yakutsk (AY) [52], Yakutsk (Y) [10], Haverah Park (HP) [53, 54]. In black the limits from the Auger surface detector (Auger SD) [55] and in blue the limits above 2, 3, 5, and 10 EeV (Auger HYB) from [49]. The shaded region shows the expected GZK photon fraction as derived in [56]. Lines indicate predictions from top-down models, see [57, 58] and [59]. Figure from [49]

fraction are set at 3.8%, 2.4%, 3.5% and 11.7% (at 95% confidence level) above 2, 3, 5 and 10 EeV respectively. The limits are shown in Figure 1.7 which is taken from [49] along with the description. As one can see, super heavy dark matter models and topological defects are ruled out. In the light of these recent results, "bottom-up" scenarios are considered much more favorable and will be described in more detail below.

In 1949, Fermi proposed the idea of stochastic acceleration of charged particles. In the original paper, Fermi considered how particles interact with interstellar clouds containing turbulent magnetic fields [60]. It is possible for a charged particle to gain

energy on average in the process of multiple scattering in the clouds. This conclusion follows from simple considerations of special relativity. Scattering centers in this case are irregularities of the magnetic field.

Let us consider a relativistic particle with momentum p_0 and energy $E_0 = p_0 c$ in the laboratory frame. It collides with a cloud moving, say, towards it with speed v_{cl}. Having applied Lorentz transformation, we can easily see that the energy of the particle in the frame of the cloud is

$$E_0 = \gamma_{cl} E_0 (1 + \beta_{cl}), \tag{1.2}$$

where γ_{cl} is the Lorentz factor of the frame of the cloud and $\beta_{cl} = v_{cl}/c$ as usual. For simple illustrative purposes, let us assume that after multiple scatterings inside the cloud the particle exits in the direction opposite to its initial direction. In this case, applying the Lorentz transformation once more gives the energy of the particle in the laboratory frame as it exits the cloud

$$E_1 = \gamma_{cl} E_0 (1 + \beta_{cl}) = \gamma_{cl}^2 E_0 (1 + \beta_{cl})^2, \tag{1.3}$$

As one can see, the particle therefore gains energy after interacting with the cloud. If the final scattering happens in the forward direction, the energy of the particle stays the same since there would be a factor of $(1-\beta_{cl})^2$ in (1.3) instead which would cancel out with the square of the Lorentz factor.

The general result, after averaging over all entry and exit angles, is that there is relative energy gain of $\eta = 4\beta_{cl}^2/3$ on average per cloud. Thus, this mechanism is called stochastic acceleration of the second order. It turns out that the acceleration time is proportional to the energy and therefore the acceleration is a very slow process to reach high energies considering that β_{cl}^2 is of the order of 10^{-7}. Another, but similar, mechanism was therefore proposed to explain charged particle acceleration in the case

of galactic cosmic rays, and then was extended for UHECR of extragalactic origin. It is called shock acceleration or first-order Fermi acceleration.

As opposed to collisions with randomly moving interstellar clouds, the first order Fermi acceleration considers particles scattering on the scattering centers which move through the interstellar medium in some definite direction determined by a moving astrophysical shock wave. For example, such shock waves form ahead of expanding supernova remnants moving with supersonic sound in the interstellar medium. Let us consider a simple one-dimensional picture following explanation by Stanev in his book [40].

Qualitatively, we can imagine the process as follows. Let us assume that velocity distribution of the cosmic rays in the interstellar gas ahead of the shock is random. Some particles cross the shock and move downstream with their velocities still being random due to multiple scattering. Some of them are scattered back and cross the shock again moving upstream until a new scattering. Thus any particle experiences only head-on collisions when crossing the shock plane in either the lab frame or the frame of the shock, and therefore it gains energy until the energy becomes enough to escape the acceleration site. Averaging over all exit and entry angles gives that there is an energy gain of $\eta = 4/3\beta_d$ after each crossing of the shock front, where $\beta_d = v_d/c$ and v_d is the speed of the downstream plasma flow after the shock has passed. This is the reason why the process is called acceleration of the first order. This process is orders of magnitude more efficient and much faster because of the first order and also because the shock speed is much higher than the speed of random molecular cloud motion.

The rate of energy gain is proportional to the frequency of collisions and the energy gained in each of them, so we have

$$\frac{dE}{dt} = \nu_{col}\Delta E = \frac{\eta E}{t_{cr}}, \tag{1.4}$$

where t_{cr} is the crossing time which can be taken as the mean free path for magnetic scattering, λ_s, divided by the shock speed v_s. The particle escapes as its gyroradius, r_g, exceeds λ_s so we can estimate the maximum energy from (1.4) which now becomes

$$\frac{dE}{dt} \leq \frac{\eta E v_s}{r_g} = \frac{v_s}{c} ZeBv_s, \tag{1.5}$$

and by integration we get that the maximum achievable energy is

$$E_{max} = \frac{v_s}{c} ZeBv_s t = \frac{v_s}{c} ZeBr_s. \tag{1.6}$$

(1.6) is valid for a freely expanding supernova remnant. More rigorous estimates of the maximum energy attainable during the full stage of supernova remnant expansion have been done in [61] and more recently [62].

$$E_{max} = Z \times (2.4 - 5.0) \times 10^2 \text{ TeV}. \tag{1.7}$$

One can see that heavier nuclei can achieve higher energies than protons.

The mechanism above is responsible for acceleration of the galactic cosmic rays, and it is natural to extend it to try to explain acceleration of the UHECR. The main requirement is that a charged particle has to be confined inside the region in order to keep getting more energy. If the gyroradius of the particle, $r_g = \gamma mc^2/eB$, becomes such that $2r_g > R$ where R is the linear dimension of the acceleration site then it escapes. From this requirement and simple dimensional arguments one can derive a lower limit on the spatial dimension and magnetic field of an acceleration site that would be required in order to accelerate charged particles up to some maximum energy E. Hillas, in his paper [63], also takes into account the average velocity of the scattering centers and then by generalizing (1.6) we have

$$\left(\frac{B}{\mu\text{G}}\right)\left(\frac{R}{\text{kpc}}\right) > 200 \left(\frac{E}{10^{20}\text{eV}}\right) \frac{1}{Z\beta_{sc}}. \tag{1.8}$$

By applying this requirement to different astrophysical objects it is possible to construct a so-called Hillas plot orginally made by Hillas in the paper cited above. It is

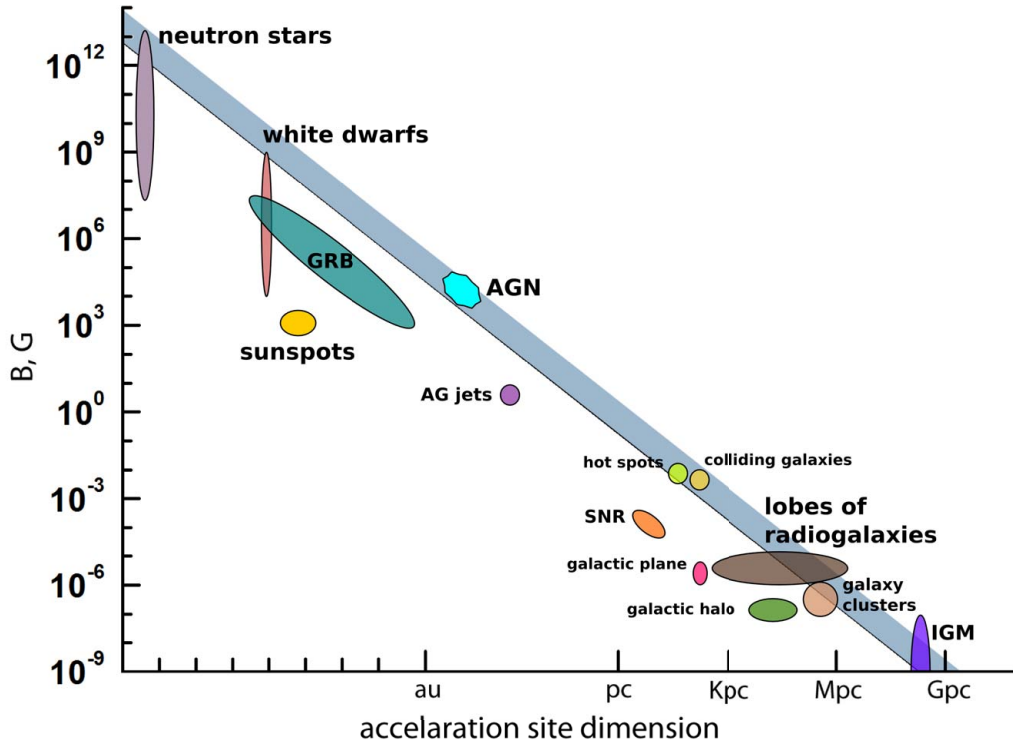

Figure 1.8 The size and magnetic field strength of astrophysical accelerators. The shaded band is possible region of acceleration of protons to an energy of 10^{20} eV and the thin black line, which limits the shaded band, is for iron nuclei accelerated to the same energy. Adapted from [40] and [64]

presented in Figure 1.8. As can be seen from the plot, there are several candidates capable of accelerating protons up to 10^{20} eV. They are neutron stars with very high magnetic field, active galactic nuclei (AGN), lobes of radio galaxies, hot spots at the end of the lobes where the jet shock fronts are stopped by the intergalactic medium, colliding galaxies, clusters of galaxies and gigaparsec scale shocks in the intergalactic medium. Let us consider an acceleration process for one of the promising candidates in more detail.

Hot spots in radio galaxies are one of the most attractive candidates. Fanaroff-Riley (FR) type II radio galaxies are giant galaxies with two jets going in the opposite directions and hot spots are formed at the end of the jets where the termination shock

happens. In two papers, Rachen and Biermann [65] and Biermann and Strittmatter [66] consider the acceleration in the presence of synchrotron losses, diffusion losses and photon interactions. The main advantage of hot spots, besides satisfactory spatial dimensions and magnetic field values, is that they are already located in the intergalactic space and therefore UHECR do not lose that much energy when escaping the region as compared to acceleration in AGN.

Following the BS-87 model developed in [66] and the general theory of diffusive shock acceleration reviewed by Drury [67] the acceleration time for strong shocks is given by

$$\tau_{acc} \sim \frac{E}{(dE/dt)} \sim \frac{80}{3\pi}\left(\frac{c}{v_u^2}\right)\left(\frac{r_g}{b(p-1)}\right)\left(\frac{r_{g,max}}{r_g}\right)^{p-1}, \tag{1.9}$$

where v_u is the upstream velocity in the shock frame, and "strong shock" means that the compression ratio is about 4. The compression ratio is the ratio between components of the upstream and downstream velocities normal to the shock plane. $r_{g,max}$ corresponds to the gyroradius of the most energetic protons. The acceleration time depends on the spectrum of the magnetic energy density of the shock turbulent magnetic field, and in deriving (1.9), the Kolmogorov type of the spectrum was assumed in the form of $I(k) = I_0(k/k_0)^{-p}$ with the spectral index $p = 5/3$, where k is the wavenumber and k_0 corresponds to the outer scale of the turbulence, or approximately to the gyroradius of the most energetic protons that can still stay inside the field. Finally, coefficient b represents the ratio between turbulent and regular magnetic field energy density, and the exact form of it is not important since it becomes unity in the limiting case for our purpose of estimating the maximum proton energy. The upper energy limit for protons is obtained from the condition that the energy loss time is equal to the acceleration time. Proton energy losses in hot spots are combined from synchrotron losses and interactions with photons. The energy loss time is given

by

$$\tau_{loss} = \frac{\tau_{syn}}{1 + Ka}, \tag{1.10}$$

where K represents the relative strength of photon-proton interactions compared to synchrotron radiation and a is the ratio of energy density of the photon field and that of the magnetic field. For hot spots the typical values are $K \approx 200$ and $0.01 \leq a < 0.1$, and the synchrotron loss time, τ_{syn}, is

$$\tau_{syn} = \frac{6\pi m_p^3 c}{\sigma_t m_e^2 \gamma B^2}, \tag{1.11}$$

where σ_t is Thompson cross section and B is the magnitude of the total magnetic field in the hot spot region.

Finally, the following expression for the proton Lorentz factor is obtained by equating τ_{acc} and τ_{loss}:

$$\gamma = \left(\frac{27\pi b}{320}(p-1)^{1/2}\frac{e}{r_0^2 B}\right)^{1/2}\left(\frac{v_u}{c}\right)\left(\frac{m_p}{m_e}\right)\left(\frac{1}{1+Ka}\right)^{1/2}, \tag{1.12}$$

where e is the electron charge, r_0 is the classical electron radius. For the limiting case, when a proton reaches the maximum energy, the ratio $r_{g,max}/r_g$ becomes unity obviously which was taken into account when deriving (1.12). Following [65], the typical hot spot field strength is $B \approx 0.5$ mG and $v_u/c \approx 0.3$. Thus, after plugging in all the numerical values we get $\gamma = 8.06 \times 10^{11}$ which corresponds to the maximum proton energy of 7.6×10^{21} eV.

Active galactic nuclei are another plausible candidate for acceleration with the dimension of the central parts of 0.02 pc across and containing magnetic fields of 5 G according to estimates from [68] so that the Hillas criteria are satisfied. On the other hand, the active acceleration region and its surroundings, unlike hot spots, are permeated with dense radiation and therefore the losses of energy of the protons are much bigger on their way to escape. Norman et al. [69] give simple estimates as

follows. Assuming equipartition of the radiation energy density and energy density of the magnetic field we obtain that

$$\frac{L}{4\pi R^2 c} = \frac{B^2}{8\pi}, \tag{1.13}$$

where L is the luminosity and R is the source radius. Plugging the magnetic field strength from (1.13) into (1.6) and assuming that the shock radius is approximately the same size as the source region we get

$$E_{max} = Ze\left(\frac{v_s}{c}\right)\left(\frac{2L}{c}\right)^{1/2} = 2.5 \times 10^{19}\beta_{-1} Z L_{46}^{1/2} \text{ eV}, \tag{1.14}$$

where $L_{46} = L/10^{46}$ ergs s^{-1} and $\beta_{-1} = v_s/0.1c$. So AGN with $L \geq 10^{44} - 10^{46}$ ergs s^{-1} and fast jets with $v_s/c \geq 0.1$ can produce protons with energies of $10^{18.5}$ eV and above. However, analysis of the losses due to synchrotron radiation and inverse Compton effect shows that the final energy is much less than the one predicted by (1.14). The following estimate of the limiting energy for a nucleus of atomic mass A and charge Z is obtained in [69] on the basis of standard theory of shock acceleration

$$E_{syn,com} \sim 3.5 \times 10^{18}\beta_{-1}\frac{A^2}{Z^{3/2}}\frac{L_{46}^{1/4}}{l^{1/2}} \text{ eV}, \tag{1.15}$$

where $l = \sigma_t L/4\pi m_e c^3 R$ is so-called compactness parameter which is ≥ 1 for most AGN. Using other typical values for AGN already cited above we see that the limiting energy from (1.15) for protons is 3.5×10^{18} or less. Photo-pion production losses are also significant and become dominant if the AGN compactness parameter satisfies the following condition

$$l \geq 10^{-6}\beta_{-1}^2 L_{46}^{1/2}\left(\frac{\epsilon}{0.1 \text{ eV}}\right)^2, \tag{1.16}$$

where ϵ is the mean photon energy.

In conclusion, the central regions of AGN are capable of accelerating the UHE protons, but they cannot escape the acceleration region without significant losses. As

a possible solution it was proposed that neutrons born in photoproduction interactions can escape and then decay back into protons. But neutrons are capable of escaping even with the energy of 10^{18} eV which is unsatisfactory to explain the origin the highest energies of UHECR. Other possible candidates listed above can all accelerate protons up to $10^{19} - 10^{20}$ eV and above, assuming the most favorable parameters and very efficient acceleration. Unfortunately, current observational data are not sufficient to develop more detailed models.

The Hillas plot suggests that acceleration of heavy nuclei can happen at the same site candidates as for protons, and condition (1.8) implies that it can happen easier than for protons due to a factor of Z. More detailed analysis, however, shows that there are additional factors affecting the maximum energy limit for heavy nuclei. The energy limit for photomeson production at the cosmic microwave background (CMB) [70] is increased by a factor of A. On the other hand, heavy nuclei can photo-disintegrate even before reaching this limit. A recent analysis by Allard and Protheroe [71] uses modeling to study diffusive acceleration process thoroughly for both protons and heavy nuclei taking into account all relevant interactions with photon backgrounds including infrared, optical and ultraviolet. For protons, these interactions are pair production, and pion photoproduction with several channels (direct pion production, resonances, multi-pion production). For nuclei, they are pair production, photo-disintegration (the giant dipole resonance in particular), and pion photoproduction (baryon resonance). Some of the interactions are considered in more detail in the next section. In conclusion, if protons can be accelerated to 10^{19} eV then nuclei are guaranteed to be able to gain the same or greater energy at the same acceleration site. This makes the pure proton scenario unlikely from the acceleration point of view unless protons are the only particles injected in the first place. If the maximum proton energy is below 10^{20} then the maximum energy of other nuclei

is proportional to the charge even for high photon backgrounds - the result which correlates with recent findings by the Pierre Auger Observatory [72].

1.4 GZK Cutoff and Propagation of Ultra High Energy Cosmic Rays

Once an UHECR is born at some extragalactic acceleration site it has to travel through intergalactic space before reaching the Earth. Discovery of the CMB by Penzias and Wilson [70] in 1965 led to a drastic impact on the theory of propagation of charged particles through space. In almost simultaneous publications, Zatsepin and Kuzmin in the USSR [73] and Greisen in the USA [74] predicted the end of the cosmic ray spectrum due to interactions of protons and heavier nuclei with the CMB: they cannot reach the Earth with energies above some cutoff energy if the sources are far enough away.

NASA satellite missions COBE and WMAP [75–77] measured CMB to have a perfect black body spectrum with temperature of 2.725 K. The background is universal and isotropic with the temperature variations on the 10^{-5} level. The average energy of the microwave photons is $\epsilon = 6.34 \times 10^{-4}$ eV.

If the total energy in the center of mass frame equals or exceeds the sum of the proton and pion masses then the photo-pion production reaction is possible with the threshold energy for a proton in the laboratory frame of

$$E_p = \frac{m_{\pi^0}}{4\ \epsilon}(2m_p + m_{\pi^0}) \quad 5 \times 10^{19}\ \text{eV}, \tag{1.17}$$

where a head-on collision is assumed. The average photon energy is used for the calculation in (1.17), but interactions can happen for a spectrum of threshold energies since the the microwave spectrum covers wide a range of photon energies. In the

proton rest frame the photon threshold energy turns out to be 145 MeV and the photoproduction reaction cross section reaches the maximum for 340 MeV photons where the Δ^+ resonance production occurs:

$$p + \gamma_{CMB} \qquad \Delta^+(1232) \qquad \pi^0 + p. \tag{1.18}$$

This cross section region is the most important due to its astrophysical implications. The spectrum of protons with energies around 10^{20} eV falls steeply with the spectral index of approximately 3 and this fact ensures that almost no interactions happen with more energetic photons. In our region of interest, 10^{20}-10^{22} eV protons lose from 17% up to 50% of their energy where the Δ^+ resonance process is the main channel for 10^{20} eV protons; whereas multiparticle production dominates for 10^{22} eV protons.

Besides photoproduction losses protons traveling in intergalactic space experience continuous energy losses due to electron-positron pair production with a proton threshold energy of 4×10^{17} eV. In each interaction in this case a proton loses approximately a thousandth of its energy.

Given knowledge of the interaction cross sections and the spectrum of the CMB one can calculate the details of UHECR propagation in the Universe. In particular, such calculations were carried out for protons in [65, 78–80]. The main parameter which determines the propagation picture is the mean energy loss length which is defined as

$$L_{loss} = \frac{E}{dE/dx} = \frac{\lambda_{free}(E)}{K_{inel}(E)}, \tag{1.19}$$

where λ_{free} is the mean free path (see the definition in [80]) of a particle as it propagates through the CMB and K_{inel} is the inelasticity, or the fraction of the particle's energy that goes to the energy of the leading recoiling particle. So the loss length is a measure of the distance at which the initial energy of a particle is decreased. Figure 1.9 shows the total loss length for a UHE proton. As one can see, the energy losses

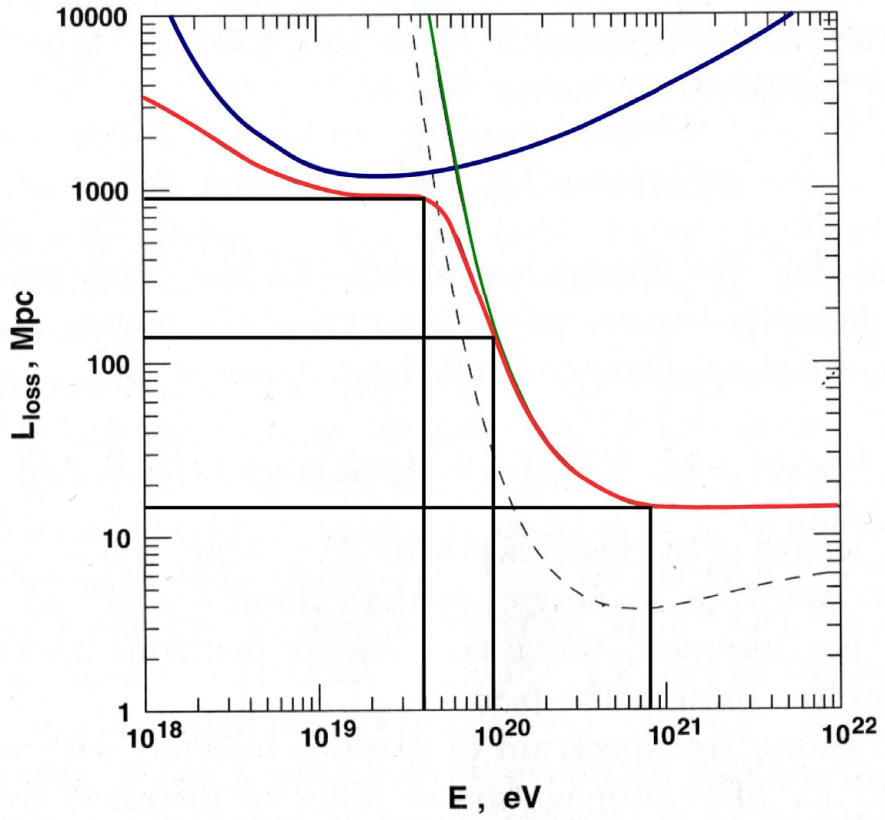

Figure 1.9 Proton energy loss length from photoproduction of pions (green), pair production (blue) and the total loss length (red). The dashed lines shows the proton interaction length. Adapted from [40, p. 229]

above 8×10^{20} eV are dominated by photoproduction, and protons can travel about 11 Mpc before loosing some fraction of their initial energy. As they travel further protons lose more and more energy so that at 10^{20} eV they can travel about 110 Mpc without further losses and then more losses happen, so that finally the losses are dominated by pair production at 3×10^{19} eV and the loss distance approaches 1 Gpc. Finally, the lowest energy protons on the plot lose their energy due to expansion of the Universe.

As was already mentioned above in 1.3, nuclei heavier than protons experience photo-disintegration in addition to pair production losses and pion production. Giant

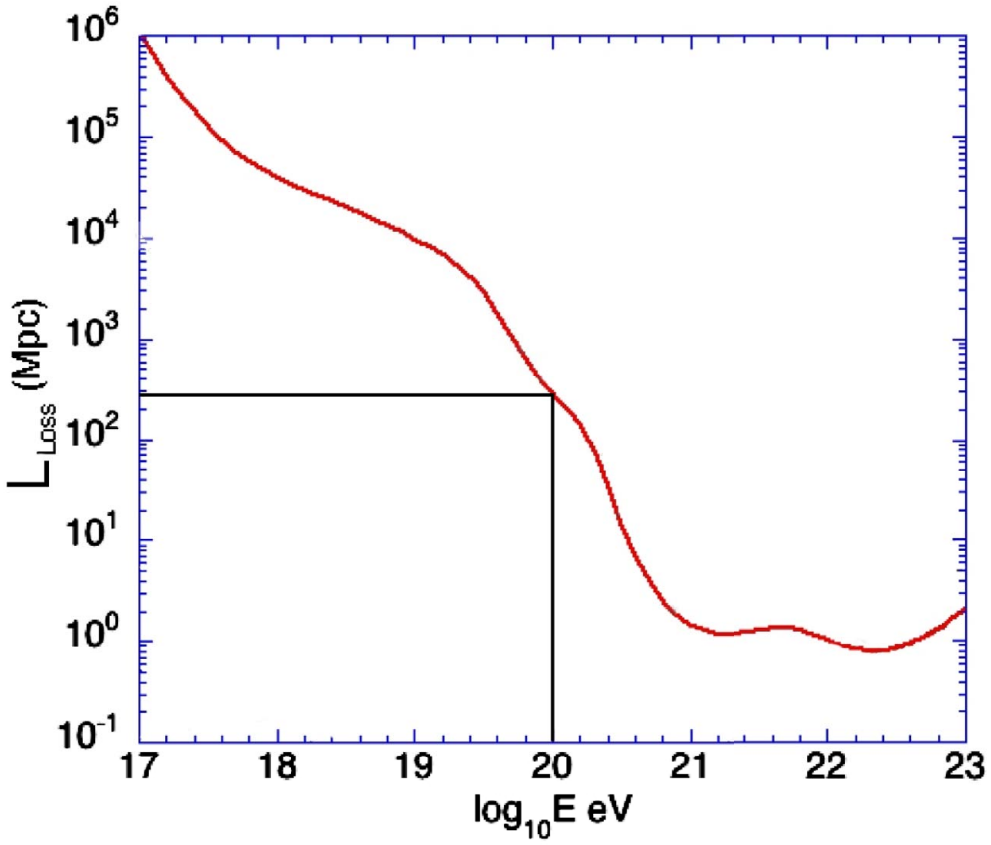

Figure 1.10 ^{56}Fe total energy loss length including intergalactic infrared, optical and ultraviolet background in addition to CMB. Adapted from [71]

dipole resonance (GDR) is the lowest energy photo-disintegration process induced by CMB or other backgrounds such as infrared, optical, or ultraviolet. It has the highest cross section and the lowest threshold for all nuclei for photon energies between 10 and 20 MeV in the nucleus rest frame [71]. The photon gets absorbed by the nucleus and then the nucleus decays by emitting nucleons and lighter nuclei. Thus nuclei, as opposed to single protons, not only lose energy as they propagate through intergalactic space but change their species as well producing a whole chain of decay products.

In general, it is harder to disintegrate stable nuclei. Allard and Protheroe [71] calculate the total energy loss length by nuclei as they propagate in the intergalactic medium. All types of photon backgrounds are taken into account. Figure 1.10 shows

the result for iron. The energy loss for nuclei happens at slightly higher energies compared to protons for the same traveled distance. As one can see, for 10^{20} eV iron nuclei the loss length is 120 Mpc as opposed to 110 Mpc for the proton case, and the loss length of 110 Mpc corresponds to a nucleus with energy of $\approx 10^{20.1}$ eV. Conversely, for the same initial energy of 3×10^{19} eV a proton can travel 900 Mpc; whereas iron travels "only" 500 Mpc illustrating that nuclei lose energy more rapidly than protons at this lower energy.

In conclusion, both protons and iron nuclei of ultra high energies cannot come from sources much further away than 100 Mpc. The above calculations of propagation of protons and nuclei consider energy losses only, but in addition to that there is the extragalactic magnetic field which must be taken into account since it can cause longer traveling paths and time delay both for protons and even more for nuclei. This fact is closely related to the notion of the GZK horizon - a virtual sphere inside of which all the astrophysical UHECR sources must be located in order for a particle of specific energy (usually 10^{20} eV is taken) from them to be capable of reaching us within Hubble time. More detailed consideration of the GZK horizon as well as effects of the extragalactic magnetic field will be given in Chapter 6.

1.5 Importance of Study

Studies of the cosmic rays, their origins and composition, started as early as 1900-1920s when it became evident that there exists a highly penetrating radiation coming from outer space. Advances in experimental techniques led to a series of advances, such as the discovery of the positron, the first evidence for antimatter, in the cosmic rays. This illustrates how this field of astrophysics helped in experimental confirmation of the quantum field theory, and played a major role in experimental particle

physics until particle accelerators were developed to study different particles in controlled environments. Nevertheless, even today detection and identification of ultra high energy cosmic rays remains a unique tool to learn about the interaction of particles at the highest energies possible to achieve in the Universe, the region of energies which none of the man-made accelerators could in principle achieve as it would require building a Large Hadron Collider of the size of the Milky Way.

Even though the field of experimental particle physics and astrophysics seems to be distant from producing practical applications to the everyday life, it surely needs to be considered in the broad context of the complex entanglement of all fields of science and industry nowadays. Advances in accelerator science made initially for the sole purpose of progress in fundamental physics led to the development of the World Wide Web as a by-product and to medical and material science applications such as cancer treatment with proton or fast neutron beams. This interconnectivity between particle physics, accelerator physics and astrophysics might lead to applications that are not conceivable at the present time, but might reveal themselves unexpectedly in the future.

As a possible example of such a link one can turn their attention to the intriguing field of solar physics. Solar activities, such as flares and coronal mass ejections, affect many sides of life on Earth without any doubt starting from the disruptions of satellite services to a possible cause of total black outs over areas as large as the United States. Prediction of the Sun's behavior is therefore a very important and complex task that mostly depends on our understanding of the solar magnetic field and the dynamo mechanism that is responsible for its formation. The direct approach to the problem through developing extensive simulations of the Sun and its observations constitutes an evident path to solve the task, but that does not eliminate other possibilities such as providing better understanding of the dynamo mechanism at galactic scales

so that it can be then re-applied towards Solar physics or the magnetic field of the Earth. Constraining galactic magnetic fields with cosmic ray data serves this goal in an implicit way by eventually, along with other astronomical techniques, providing the best field candidates which will need to be explained by dynamo theory.

Chapter 2

The Pierre Auger Observatory

2.1 Main Components

The Pierre Auger Observatory is a complex hybrid detector of extensive atmospheric showers initiated by the UHECRs. As it follows from the physics of the shower development in the atmosphere, the observatory has two main components: an array of ground detectors spread over a large area and a set of telescopes for detection of the fluorescent light produced by nitrogen atoms excited due to passage of charged particles along the shower axis. The overview of both systems could be found in [81] and [82]. Figure 2.1 shows a satellite image by Google Earth [83] superimposed with both surface and fluorescence detectors of the Pierre Auger Observatory. One can observe an event that lands in the middle of the array and produces enough light to be seen by all of the four telescope buildings, triggering a large number of the surface stations. In the next two subsections I give a brief overview of the main parts of the observatory.

2.1.1 Surface Detector

The array of ground detectors, or otherwise called the surface detector (SD), consists of over 1600 water Cherenkov detectors (WCDs). Each WCD is located in a node of a triangular grid with the distance of 1.5 km between adjacent detectors. A WCD is made of rotationally molded polyethylene resin and has a Tyvek® liner inside

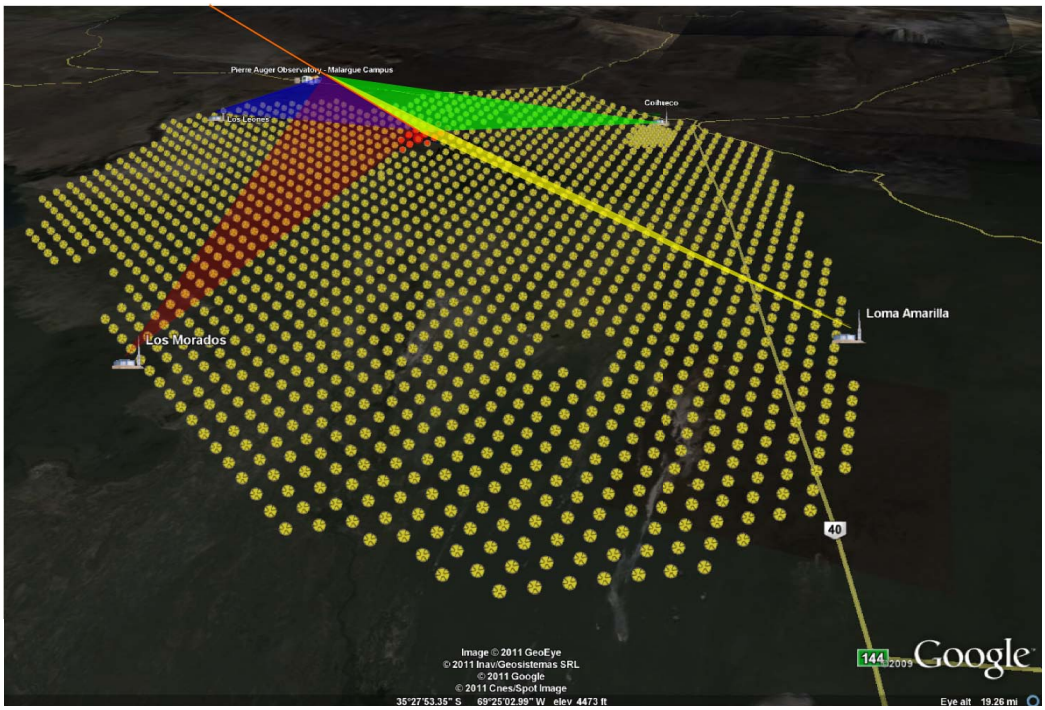

Figure 2.1 Pierre Auger Observatory

which is filled with 12 tons of purified water. The water undergoes several stages of purification including reverse osmosis, destruction of organic carbon and bacteria by ultra-violet light, and electro-deionisation, so that it should remain ultra-pure for the whole lifetime of the experiment – two decades. The Cherenkov light, which is produced in the water by the shower muon and electrons, is reflected from the liner walls and collected by three photomultiplier tubes (PMTs) installed at the top of the liner. The signal from them is then digitized with time bins of 25 ns and is sent via a radio-link to the radio towers built next to each fluorescence detector site and from them to the central data acquisition system. Each WCD has its own GPS receiver for time stamping.

Depending on where the core of an EAS is located with respect to a WCD, the number of particles coming through the water volume could vary by three orders of magnitude, from 1 particle per μs to 1000 particles per μs. This requires a large

dynamic range which is provided by the PMT base electronics. The calibration of the signal happens individually at each WCD by measuring the distribution of the collected charge and pulse height at the peak of a signal due to atmospheric muons. The peak position of the charge distribution is proportional to the charge produced in the PMT by a single vertical muon which can be measured separately. Thus the signal in the WCDs is measured in units of vertical-equivalent muons (VEM), which the average signal in 3 PMTs produced by a vertical muon going through the center of a WCD. The accuracy of the calibration is 2%. The calibration happens once per minute. See [84] for details.

The signals in the PMTs come from low energy cosmic ray muons at a large rate of 3 kHz [81] so a hierarchical trigger is implemented to reduce the background rate significantly and select the true shower event candidates which are stored for further offline processing. The first level trigger is called T1. T1 is implemented at the level of an individual WCD. T1 has several modes programmed for selecting signals from EAS of different geometrical nature. One mode (threshold trigger, TH) looks for time coincidence of the signals in three PMTs, each signal being at the level of more than $1.75 I^{peak}_{VEM}$, where I^{peak}_{VEM} is the height of the single muon pulse peak. This mode is aimed at selecting the muonic signals from an inclined EAS, a shower with a zenith angle[1] larger than 75°. Another mode of the T1, which is called "Time-over-threshold" (or ToT), selects signals from the vertical (zenith angle is less or equal 60°) low energy showers with a close core, or very high energy showers with a distant core. The electromagnetic component is mixed with muonic in this case, and the signal appears to be spread in time significantly due to different time of arrival of the photons and other particles. The ToT trigger then selects signals at the level of

[1]The zenith angle is an angle between the vertical direction and an arrival direction of an extensive air shower.

$0.2I_{VEM}^{peak}$ spread over time of at least 325 ns.

The next level trigger is T2. It reduces the rate of events from a single WCD to 20 Hz to comply with the limitation of the transfer rate of the radio communication system. T2 passes all ToT-T1 triggers whereas it requires TH-T1 triggers to pass a higher threshold of $3.2I_{VEM}^{peak}$. The timing information of T2 is sent to the central data acquisition system (CDAS) where it is analyzed to form the next level trigger, T3. T3 has two modes with one of them intended for selection of vertical showers whereas the second one is for inclined ones. In the first mode, ToTs passed to CDAS by T2 are searched through to find spatial and temporal coincidence. To look for vertical showers the following spacial coincidence criterion is applied: a triggered detector must have one of its closest neighbors and one of its second closest neighbors to be triggered with ToT. As for inclined showers, the spatial criterion is less strict in comparison with the previous criterion, with the only difference that any of the third or the forth triggered closest neighbors is required. The temporal condition for T3 is the same for both modes: all of the T2's from triggered stations which satisfy the spatial criterion must be within (6+5n) μs interval from the first one, where n corresponds to the n-th set of neighbors. Figure 2.2 shows the illustration of both modes of the T3 trigger. 90% of T3 triggers in the first regime correspond to real showers whereas only 10% does so in the second regime.

Those event candidates that pass T3 and are saved by CDAS undergo a further series of selections to choose real shower events for further analysis. Two last triggers, T4 and T5, are applied to them. T4 is a dual trigger. 3ToT-T4 trigger requires three neighbor stations that form a triangle to have T2-ToT triggers, and also the signal timing in all of those stations must be within the time interval that is needed for a shower plane to pass them at the speed of light. For vertical events this ensures 98% effectiveness of selection. Some of the candidates might have triangular pattern of

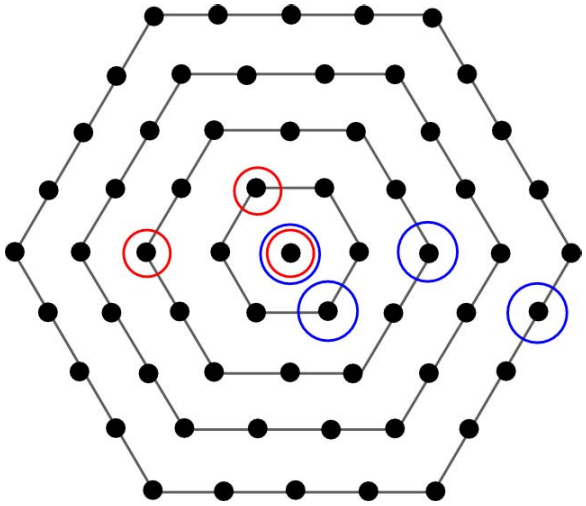

Figure 2.2 Examples of two modes of the T3 trigger. Red circles show stations triggered that would be selected by the first regime of T3, and blue circles show the second regime of T3 correspondingly

the triggered tanks but not all of them being ToT. Those kind of events are selected with 4C1-T4 trigger, which requires 4 triggered nearby stations without specifying the type of T2, but the signal timing must also satisfy the fit for a plane shower front moving at the speed of light. Thus the combined T4 ensures almost 100% efficiency of shower selection below 60°.

Finally, T5 is the fiducial trigger which is aimed to select only events with the shower core contained inside the array. It ensures then proper reconstruction of the shower energy and other parameters. T5 requires that the station with the highest signal must be surrounded by 6 other active stations. T5 also excludes events that land close to non-working stations which are expected to be present at a 1% level for a normally operated, well-maintained array. T5 allows for calculation of the surface detector acceptance based on the effective area which saturates to the geometrical area above some energy. All the events in the dataset used in this work have passed the T5 quality trigger.

The acceptance of the surface detector for vertical showers becomes greater than

97% at the energy of 3×10^{18} eV, verified using three different approaches. In the first one, the data from the surface detector are used to produce mock events with random arrival times and amplitudes so that the trigger probability is determined by applying the full trigger and event selection chain. Another approach uses the hybrid dataset from both fluorescence and surface detector to calculate the surface detector trigger probability by looking at the percentage of the events that became hybrid out of the total number of events registered by the fluorescence detector. Finally, full shower and detector simulations are done for different primary particles. All three methods agree on the threshold value above.

Knowing that the surface detector is fully efficient above 3 EeV, one can calculate the exposure based purely on the geometrical aperture and observational time. If we take into account only events with T5 triggers, then the geometrical aperture can be merely represented by a sum of hexagonal elemental cells. The number of active cells is recorded continuously so that the total exposure of the surface detector above 3 EeV can be easily calculated at any given moment. The total exposure was 20,905 $km^2 \cdot sr \cdot year$ in the period from January 1st, 2004 and December 31st, 2010. The uncertainty is 3%.

2.1.2 Fluorescence Detector

The purpose of the fluorescence detector of the Pierre Auger observatory is to detect fluorescence from atmospheric nitrogen molecules excited by the electromagnetic component of an EAS. The detector represents four separate sites situated on the elevated terrain so that they overlook the surface detector from four sides. The sites have their own names: Los Leones, Los Morados, Loma Amarilla and Coihueco in counter-clockwise order if one starts with the most southern site, Los Leones. Figure 2.1 shows an example of a shower which was energetic enough for its fluorescence to

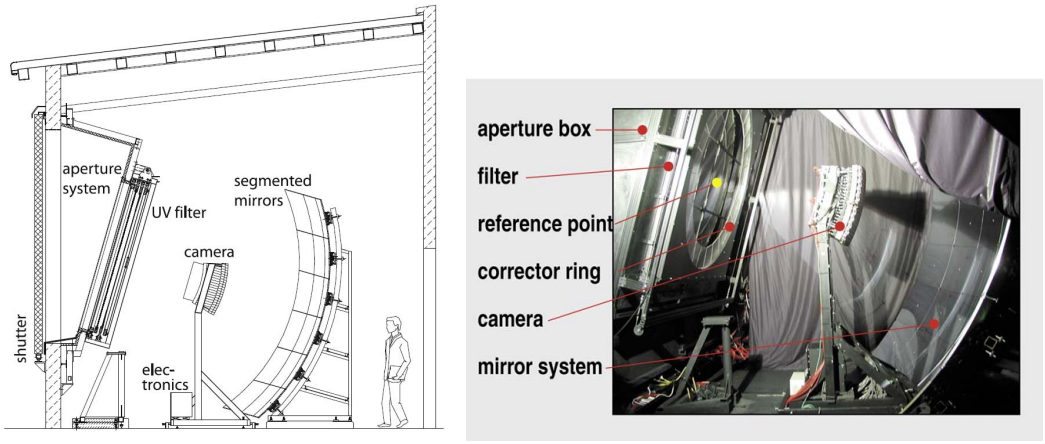

Figure 2.3 Schematic side view of a fluorescence telescope (left). Picture of the telescope from inside (right). Taken from [14]

be seen by all four sites. Each of the sites consists of six telescopes with a field of view of $30^\circ \times 30^\circ$ so that the azimuthal coverage of each site is 180°. This coverage proves to be enough for the whole detector to be fully efficient for the primary energies above 10 EeV.

Each site building has a climate control system to sustain normal operating conditions inside. There are six separate spaces in each building called "bays." There is a telescope in each bay. Figure 2.3 shows the profile of a telescope. I will describe the components and their purpose following the path of light propagation. First of all, there is a shutter which opens the aperture when the outside meteorological and light conditions are satisfied for observations. The next component of the telescope is a filter window made of MUG-6 glass which has a spectral transmittance such that it only allows ultra-violet photons between 280 and 420 nm to pass in the part of the spectrum where the fluorescence emission occurs. There is a broad range of wavelengths above 680 nm where MUG-6 is transparent to light but the quantum efficiency of the PMTs used in the camera is practically zero in that region. Without the filter, the background from optical wavelengths would be so large that it would

be impossible to filter out any fluorescence signal.

After passing through the filter, the light goes through the circular aperture. The next component is the corrector ring at the edges of the aperture. This ring serves the purpose of eliminating coma aberration and substantial reducing of the spherical aberration. The telescope utilizes the Schmidt scheme [85] with the requirement for an image from an infinite light source to be no larger than 15 mm in diameter for any source location inside the field of view. This spot size corresponds to 0.5° of angular spread, less than the field of view of a single camera pixel which is 1.5°. The corrector ensures the above requirement and almost doubles the aperture. See [82,86] for details. Also, there is a curtain after the MUG-6 window and corrector ring which can close automatically in the case of an emergency to prevent too much light getting inside the bay and causing damage to the photomultipliers under high voltage.

The light is reflected by a spherical mirror with a height of 3.6 m and a radius of curvature of 3.4 m. Such a large mirror was manufactured by segments to maintain low cost and weight. There are two different designs of the mirror segments that are used in different telescope buildings. One design utilizes 36 rectangular pieces of anodized aluminum with $AlMgSiO_5$ reflective coating covered with aluminum-oxide for protection, and another one uses 60 hexagonal glass mirrors with pure Al as the reflective layer covered by SiO_2 for protection. The curvature of the segments is the same as that of the whole mirror, and their reflectivity exceeds 90%.

The mirror focuses light on the focal surface of the optical system which is a spherical surface with the radius of curvature of 1.743 m. An array of photomultiplier tubes is mounted to coincide with this surface. Each PMT is called a pixel, and there are 440 pixels in total forming a camera. There are 22 rows and 20 columns of pixels in one camera. The centers of the pixels form a hexagonal grid of cells which are precisely milled in a solid aluminum block with the dimensions of 930×860×60 mm

which forms the camera body. The body is positioned very precisely in order for the PMT cathodes to be on the focal surface. The precision of ± 1 mm in positioning and angular precision at the level of one millirad ensure that the image spot size is kept within the required specification of occupying an area no larger than 15 mm in diameter. Different verifications have been made to check the stability of the camera and mirror alignment: repeatable measurements of the images of bright stars, laser shots from the Central Laser Facility (CLF), and stable reconstruction of the hybrid and stereo events.

Once all PMTs are installed in the camera body there is still a space between them which could cause unnecessary reflections and reduce the light collection in general. In order to avoid that, light collectors, shaped as "Mercedes stars," are installed in between the PMTs. Each plastic star is coated with aluminized Mylar^{TM} foil and has a cross section of an equilateral triangle so that there is a sharp border of the adjacent pixels in terms of light collection. The light collectors allow for an increase in the collection efficiency by 24% compared to an efficiency of 70% in the case of no collectors so that the efficiency becomes 94%.

Each PMT is a XP3062 photomultiplier unit with 8-stage multiplication and a standard bialkaline photocathode with the maximum of quantum efficiency being approximately in between 350 and 410 nm. The nominal gain is 50000. There is a stabilization of the high voltage on the anode to ensure it does not change by more than 1% even in the case of anode currents reaching up to 10 μA due to moonlight background for example (the dark sky background is usually close to 0.8 μA).

As for the processing of PMT signals, a three-stage trigger system is used. The readout of a signal starts from the head electronics which is composed of several boards mounted on the back of the PMTs themselves. A driver board receives the anode signal though an AC-coupling and supplies it to the next stage which is the

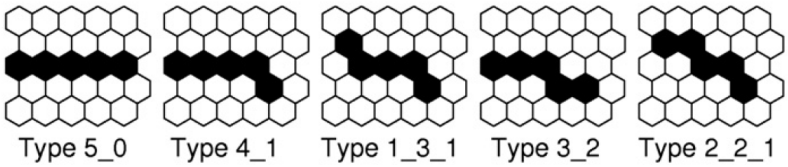

Figure 2.4 Elemental patterns of the triggered pixels to be considered by the SLT

front-end electronics. The front-end electronics consists of 20 analog boards, one per column of 22 pixels. The boards deal with high dynamic range of the signals requiring 15 bits and 100 ns timing. Each analog board prepares the analog signal for digitization at the next stage. It applies an anti-aliasing filter to the signal so that it matches the 10 MHz digitization. At the next stage of processing, a compression is done on the signal so that it is digitized with 12-bit analog-to-digital converters (ADCs). This digitization is done in the first level trigger module. The module saves ADC values continuously for the previous 100 μs. The first level trigger (FLT) is generated when the sum of the last n ADC values exceeds the threshold value, where $5 \leq n \leq 16$. The threshold is adjusted so that the FLT rate is constant at 100 Hz. The number of triggers happening within a 100 ns time window in each pixel column is recorded to be further analyzed by the second level trigger.

The second level trigger (SLT) analyzes the patterns of the triggered pixels. An EAS going through the atmosphere generates a linear track of triggered pixels in the camera. Figure 2.4 shows the basic patterns that SLT electronics looks for. All of the rotated and mirrored combinations of those 5 basic patterns are allowed. Also, to account for faulty pixels or pixels that have not triggered, only four pixels from the possible five are required to be triggered for any pattern. That makes the total number of different pattern combinations to be 108, and the full scan of the whole camera lasts 1 μs.

The third level trigger (TLT) is implemented for the events that pass the SLT. The

TLT aims at removing noise events such as lightning events, events caused by cosmic ray muons interacting with the cameras, and randomly triggered pixels. Lightning events form the bulk of the noise events. The TLT has been adjusted based on the true showers and noise events so that it rejects 99% of the lightning events without reading out complete ADC traces allowing for very fast decision time. When combined with other type of noise, the TLT rejects 94% of known background signals.

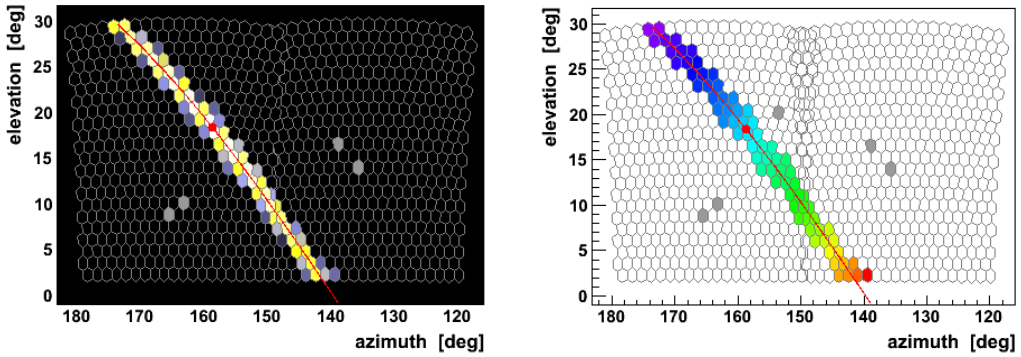

(a) Signal level **(b)** Timing

Figure 2.5 An example of a shower triggering a track of pixels in two cameras of an FD site. The colors correspond to the relative signal levels in the pixels on the left plot, and to the relative times of the signal appearance on the right plot.

Events that passed the TLT from different cameras are analyzed by software running on the machine called EyePC to merge events from adjacent cameras if they were triggered by the same EAS crossing the field of view of the both cameras. More importantly, EyePC is responsible for forming the hybrid trigger, T3. T3 is sent to the CDAS and then triggers the surface array so that the signal even from a single tank triggered by that event could be recorded as long as it happens in the time window calculated based on the impact time prediction from the corresponding FD site. This trigger is needed to record hybrid events even below the energy of 3×10^{18} EeV, the energy of full efficiency for the surface array. Figure 2.5 shows an example of a shower

that triggered pixels in two cameras at the same time so that the EyePC views from both cameras together. There are also 4 pixels that triggered far away from the real event track and are discarded in the event energy and X_{max} reconstruction.

2.1.3 Recent Extensions

I described two main parts of the Pierre Auger observatory in the previous two sections. There are recent improvements and extensions that have been made and are currently in progress which will expand capabilities of the project. A brief description of those extensions is given below.

HEAT. The Pierre Auger observatory was originally designed to investigate the UHECRs at the energies above 10 EeV where the GZK cutoff and possibly the end of the cosmic ray spectrum occurs. On the other hand, the region of energies between 10^{17} eV and 10^{19} eV is where the transition between galactic and extragalactic sources should happen, which is therefore a very interesting region of energies for astrophysics. Three high-elevation Auger telescopes (HEAT) have been deployed recently as an extension of the observatory in order to detect showers at those energies by the fluorescence technique.

There are several related reasons why a separate telescope site was needed for showers of lower energies: they cannot be seen from far away due to light attenuation in the atmosphere; also they develop earlier in the atmosphere and therefore their maximum cannot be seen with a telescope that does not have enough field of view in elevation (as is the case with the regular telescopes of the observatory with 30° field of view above the horizon); finally, there would be a statistical bias in the selection of such showers due to the previous reason. Three telescopes of HEAT have essentially the same design of a regular telescope but there is an ability to tilt the whole telescope building up by 29° so that they can look at higher elevations from 30° to 60°. They

have been built close to one of the regular FD sites, Coihueco and also overlook another extension, the infill surface array. Such location ensures an ability for hybrid reconstruction of the showers of lower energies as well as the cross-calibration between the Coihueco cameras and HEAT cameras as some of the showers are detected in both detectors as one event happens across the cameras. HEAT started full scale operation in September 2009 and will undoubtedly extend the sample of high quality hybrid data to much lower energies. One can find the latest review of HEAT in [87].

AMIGA. Auger Muons and Infill for the Ground Array (AMIGA) constitutes another extension project which is aimed at lowering the energy of detected showers for the same physical reasons that are outlined above in the section about HEAT. AMIGA consists of two parts: the infill array with smaller spacing in between the WCDs as compared to the main array, and an array of underground scintillators to count muons.

The infill array exploits the same hexagonal grid as the main surface detector with some of the stations belonging to both. There are two scales for the hexagonal grid: 750 m in between stations and 433 m. The total area of the infill array is 23.5 km^2 for the bigger scale and 5.9 km^2 for the smallest one in accordance with the steep growth of the cosmic ray flux as the energy of the primary decreases. The full efficiency of detection is reached at 3×10^{17} eV for the large scale infill and at 10^{17} eV for the small scale. Close similarity between the main surface array and its "little brother" allow for the same trigger and reconstruction concepts to be applied to the latter one with corresponding modification of some parameters.

Muon detectors are planned to be installed at each WCD. There are three of them deployed at present as a part of a prototype unit hexagon cell of seven stations and seven muon detectors. A muon detector is made of a scintillator consisting of two 10 m^2 modules and two 5 m^2 modules buried 2.3 m (540 g/cm^2) below the surface. The

trigger will be supplied by the WCD on the surface. Using the preliminary data from the prototype detectors, it has been shown that there is a time correlation between the WCD trigger and hits in the muon detector corresponding to the same event so it is possible to discriminate them from the random muon background. The latest review could be found in [88].

AERA. It has been known since the works by Askaryan [89, 90] in the 1960s that EAS generate radio signals as they propagate through a medium. One of the reason is that there is a net negative charge due to annihilation of positrons which propagates in the medium and produces Cherenkov radio-waves. This was shown to be true for dense media. On the other hand, there is also a synchrotron radio emission by shower particles that form an electric dipole due to separation in the Earth's magnetic field. The synchrotron emission occurs at frequencies of 10-100 MHz and was proven to be coherent by experiments such as LOPES [91] and CODALEMA [92]. Complementary detection of radio-waves from EAS could improve the overall reconstruction quality of showers.

Auger Engineering Radio Array (AERA) is an extension of the Pierre Auger observatory aimed at the detection of the radio-waves from EAS in the "self-triggering" mode, i.e. without any external trigger from the other components of the detector. The ultimate goal is to cover 20 km^2 with an array of antennas arranged on a triangular grid with different spacing ranging from 150 m to 375 m. There are 21 antennas already installed with the spacing of 150 m that has already detected the first shower which is also detected by the surface and fluorescence detectors. The energy threshold is 10^{17} eV. More detailed information about the project can be found in [93].

2.2 Overview of Results

In this section I give a brief review of the main results obtained by the Pierre Auger observatory and how some of them are related to the topic of this dissertation.

2.2.1 Energy Spectrum

Measuring the energy spectrum of UHECRs is one of the main tasks of the Pierre Auger observatory. The latest published energy spectrum is based on the dataset collected from 1 January 2004 and 31 December 2010 with the exposure of 20,905 $km^2 \cdot sr \cdot year$. All of the events are "vertical" with the zenith angle of 60° or less and have passed the T5 fiducial trigger. The spectrum is derived in the region of full efficiency above 3 EeV where the total number of events that passed the above criteria is 64,000. On the other hand, there are also hybrid events with smaller statistics but better quality of the reconstruction. The details of the reconstruction procedure for both SD and FD will be given in Chapter 4. The final result, the combined spectrum, is obtained using both spectra. Figure 2.6 shows the combined spectrum which is multiplied by E^3 to make the features stand out. Two different fits, a piecewise and a continuous, are done to stress the spectrum features.

One can see both ankle and suppression of the flux in the spectrum. Without detailed mass composition knowledge and source distribution, it is impossible to give an unambiguous interpretation of the features. The ankle could be related to the the transition between galactic and extragalactic sources, but on the other hand it is possible that the transition happens at lower energies (see Chapter 1 for the discussion about the second "knee"), and in this case the ankle is explained by the electron-positron pair-production by UHE protons at the CMB. The suppression in

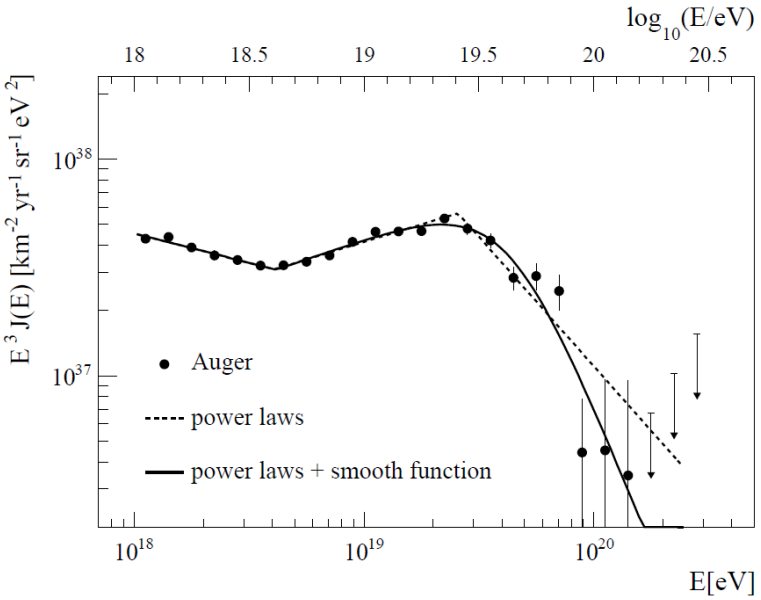

Figure 2.6 The combined energy spectrum from [94]. The shown uncertainties are statistical. The overall systematic uncertainty is 22% (see Chapter 3 for details).

the spectrum might indicate the GZK cut-off but it needs to be confirmed by the composition measurements and observation of the GZK photons and neutrinos, otherwise there is an alternative that accelerator sites just run out of power at this energy.

2.2.2 Composition

The fluorescence detector measures how an EAS develops in the atmosphere in time. It turns out that this development is directly related to the mass (atomic number A) of the primary particle. The position of the maximum of the shower cascade in the atmosphere, X_{max}, is the parameter that bears this information. The result of the FD measurements is a distribution of X_{max} from individual showers. The distribution is a convolution of fluctuations of the first interaction depths from individual showers, of fluctuations in the cascade development and, finally, of the detector resolution.

As a simple, but useful, model one can imagine a heavy primary of energy E just

as a collection of A nucleons since we can neglect the bounding energy as compared to the kinetic energy in the energy region under consideration. In this case, a shower initiated by a primary of mass A can be treated as a superposition of A proton showers with the energy of the primary proton of E/A. As shown in the previous chapter, X_{max} is proportional to the logarithm of the primary energy, and so the maximum of a shower initiated by a heavier primary occurs at shallower depths in the atmosphere than the one by a lighter primary. Also, the fluctuations in the shower development get reduced by a factor of $\overline{A}$ for the heavier nuclei as compared to proton showers since there are now A independent cascades. The fluctuations are higher in reality due to interactions between the nucleons of the primary but they are smaller than for proton showers.

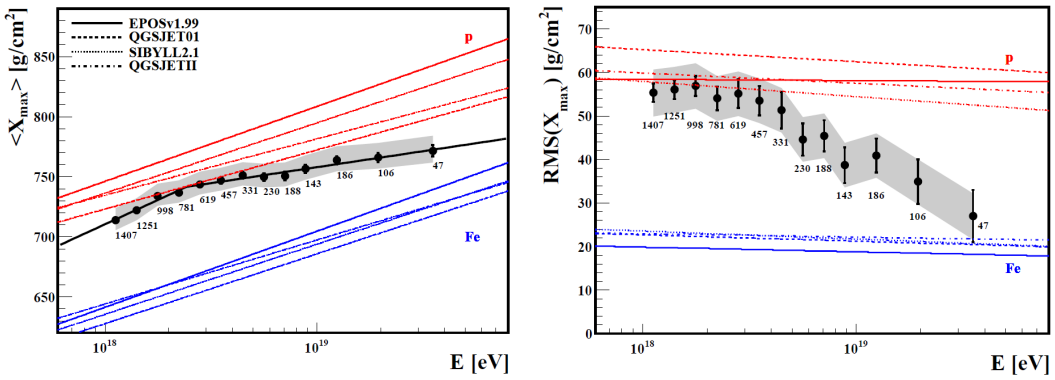

(a) X_{max} **(b)** RMS(X_{max})

Figure 2.7 X_{max} and its RMS inferred from the nitrogen fluorescence measurement by the Pierre Auger observatory. From [95].

Figure 2.7 displays the X_{max} and a measure of its fluctuations, which is the root mean square (RMS) of its distribution. The X_{max} is reconstructed from the measurements by following a careful event selection procedure. A series of data reductions (or "cuts") is applied to hybrid events so that it only leaves the events for which the current aerosol content of the atmosphere was well measured and there were no clouds in

the field of view. Those events when the shower axis made an angle with the telescope axis of less than 20° are rejected as well due to large fraction of the Cherenkov light. The fiducial cut is made as well so that only events with the maximum in the field of view are left and also only for those geometries where the full range of X_{max} values could be observed. A possible bias in composition is avoided by making sure that the trigger is saturated for both possible proton and iron showers. The uncertainty of the detector of 20 g/cm^2 is calculated based on detailed MC simulations and on the data from stereo events so that the events with uncertainty large than 20 g/cm^2 are rejected as well. In summary, there are 6,744 events above 1 EeV that are used to produce the results shown in Figure 2.7. All the details and actual distributions for the different energy bins could be found in [95].

The results show a steady composition change from light to heavy primaries in the energy region under consideration. However, this conclusion is based on the comparison with different models of the air shower development as can be seen on Figure 2.7. On the other hand, laboratory measurements of the cross-section for proton-proton interaction have been done at Tevatron and LHC at much smaller energies of 10^{15}-10^{16} eV, whereas the models use extrapolated values of the cross-section at 10^{19}. This opens a possibility of an alternative explanation that the cross-section at this energy changes dramatically for protons without necessitating a change in the composition. All of the events considered in this dissertation have energies above 50 EeV where the statistic of the fluorescence detector is too low to measure X_{max}, and therefore the assumption of pure proton composition is still legitimate even though somewhat diminished by the plots of Figure 2.7.

2.2.3 Arrival Directions

The mystery of the sources of the UHECRs has remained one of the biggest puzzles in fundamental science since their discovery. The Pierre Auger Observatory has been built to solve it. The search for sources translates into a search for some features, hot spots or large scale anisotropy on the observed sky of arrival direction taking into account the exposure of the observatory.

It turns out that there are several factors that can lead to a large scale anisotropy in the arrival directions of cosmic rays at the "ankle" energies. If one assumes that cosmic rays at this energy are galactic, then it is possible to make a prediction for the distribution of arrival directions on the Earth's sky starting from an assumed source distribution, composition and galactic magnetic field. Such modeling usually predicts existence of a dipole anisotropy in the arrival directions. On the other hand, if the transition between galactic and extragalactic cosmic rays happens at lower energies than the ankle, and most of the cosmic rays observed by the Pierre Auger observatory are of extragalactic origin, then there could be a dipole due to relative motion of the Galaxy with respect to the fixed extragalactic sources assuming their isotropic distribution. Both possibilities are analyzed and compared with the results of the analysis of the Pierre Auger observatory dataset above 2.5×10^{17} eV. The amplitude of the first harmonic is measured to be less than 2% at 99% confidence level for all energies above the considered threshold. This result eliminates some particular scenarios of source distribution and specific galactic magnetic field symmetries but the collected statistics are not enough yet to discriminate between some variations in the leaky box model and full confinement models (see [96]) as well as models with purely extragalactic flux.

As energies of the primary cosmic rays increase one can naively assume that the deflection by the intervening extragalactic and galactic magnetic fields gets small

enough to be neglected. In this case it is reasonable to search for correlation of the arrival directions with the location of extragalactic sources on small angular scales. The technique for such study is based on a prescription for different cuts that are established based on an early exploratory dataset. Once a maximum correlation is established for a particular set of cuts and source catalogs one starts running the analysis on the future independent dataset until some pre-established significance threshold has passed. Such analysis has been done with the Pierre Auger observatory data at the highest energies and the prescription cuts have been established based on the dataset up to May 2006. The energy cut was set at 55 EeV for Veron-Cetty & Veron (VCV) catalog [97] of active galactic nuclei (AGN) and the maximum correlation between AGN positions and arrival directions of cosmic rays was found for an angular distance of 3.1°. The new dataset that was searched for correlation with the prescription parameters above passes the significance threshold in August 2007 and the results can be found in [98]. The full dataset contains 20 correlating events out of 27 in total above 55 EeV, or a fraction of 0.74, whereas only 0.21 is expected from an isotropic distribution. See [46].

More collected data have shown that the results above turned out to be an upward fluctuation. Updated analysis published in [48] shows that for the data up to 31 December 2009, the number of correlated events became 21 out of 55, or a fraction of 0.38. Nevertheless, arrival directions still remain anisotropic both intrinsically and with respect to the catalog. Figure 2.8 shows the sky map of the arrival directions in galactic coordinates (see Chapter 5 for the updated result. There is 0.3% chance that 21 or more events correlate with the VCV catalog on random being drawn from an isotropic distribution. The case of intrinsic anisotropy will be considered in Chapter 6 in detail.

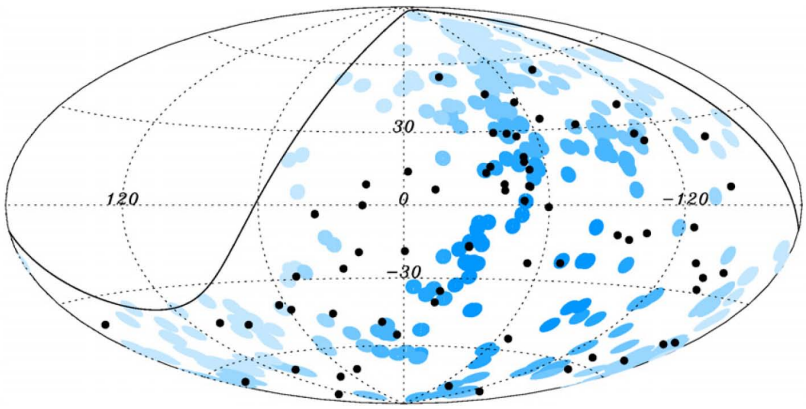

Figure 2.8 Black dots are 69 arrival directions of UHECRs in galactic coordinates with the energy above 55 EeV detected by the Pierre Auger Observatory from 1 January 2004 upto 31 December 2009. There is an AGN from VCV catalog in the center of each blue circle of radius 3.1°. The paling shades of blue color show decrease of the exposure towards the border represented as a solid line. Taken from [48].

2.2.4 Limits on Gamma Ray and Neutrino Fluxes

As described in Chapter 1 photons with ultra-high energies can form as a result of decay of super-heavy relic particles, or they can also be produced in interactions of the UHE protons with CMB. Simulations of the photon showers predict that their average X_{max} value of 900 g/cm^2 corresponds to much deeper showers than for proton or iron showers. Figure 1.7 in Chapter 1 shows the limits for photon primaries set with the Pierre Auger observatory from [49]. The result rules out some of the exotic models and helps to eliminate systematic uncertainties in measuring the cosmic ray spectrum since it limits the amount of possible photon background.

Finally, the Pierre Auger observatory has an ability to register showers initiated by neutrinos. Neutrinos of ultra high energies are thought to be produced in acceleration processes or during propagation when charged particles such as protons or heavier nuclei interact with photon backgrounds and produce pions which in turn decay producing neutrinos. To search for showers initiated by neutrinos one has to look

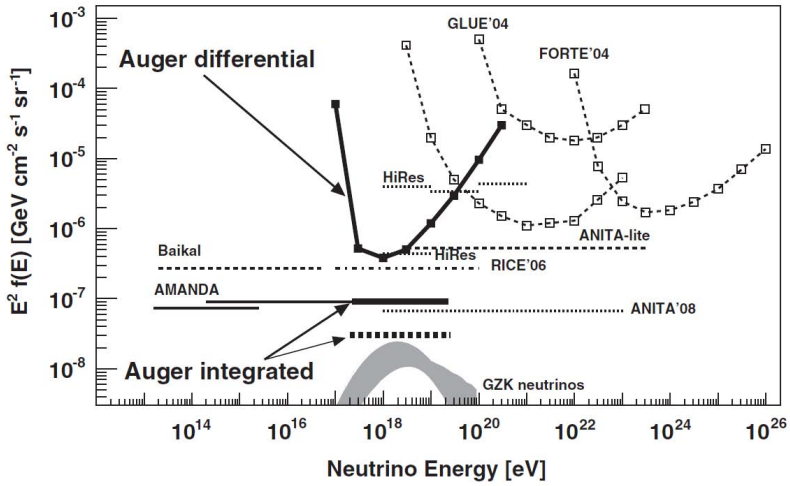

Figure 2.9 Limits on neutrino fluxes assuming equal mixing due to neutrino oscillations. The solid line represents the most conservative case with the worst systematic errors whereas the dashed line is for the smallest systematic error. Adopted from [99].

for horizontal showers that develop deeply in the atmosphere with zenith angles of 75° or more since any other known particle would interact at a much shallower slant depth. Deep horizontal development ensures that there would be a difference between neutrino induced showers and regular hadronic events: the electro-magnetic component of a horizontal hadronic shower would be attenuated by the atmosphere leaving only the muonic component that reach the surface detectors, whereas a neutrino horizontal shower could be initiated close to the array due to neutrino's extremely small cross section so that it has both of the components present. No neutrino showers have been detected but the limits were set in [99]. Figure 2.9 shows the limits of the neutrino flux at 90% confidence level for any of neutrino flavors assuming that they are equally mixed by the time of arrival to Earth. The gray shaded area shows the predicted flux for neutrinos coming from the GZK interaction of protons with CMB.

Chapter 3

Absolute Calibration of Fluorescence Detector with Pulsed LED

3.1 Calibration Systems of Fluorescence Detector of Pierre Auger Observatory

Along with proper calculation of the Cherenkov light yield and, especially, of fluorescence yield in the atmosphere [100], absolute calibration of the fluorescence detector of the Pierre Auger Observatory is the most important task to establish the proper energy scale of the whole experiment. One needs to know the conversion factor between the digitized signal from the telescope photo-multiplier tubes and the real number of photons that hit the tube at any given wavelength in the region of interest which is between 290 and 430 nm, where fluorescence of nitrogen occurs. In this section I give a general description of the whole calibration system including the relative calibration as well. The following sections will give more details on the absolute calibration technique.

There are several approaches that one can utilize to preform the absolute calibration of a fluorescence telescope. As described in section 2.1.2, the telescope consists of

several optical components. Fluorescence light has to go through an MUG-6 window, and perhaps a corrector ring, and reflect from the mirror before hitting the array of the PMTs. It implies that one can convolute transmittance and reflectance of each component measured in a lab and do geometrical ray tracing as well to get the spectral dependence of the camera efficiency. This was done in [101] with a claimed uncertainty of 20%.

The uncertainty above is not satisfactory, and optical properties of the whole system cannot be guaranteed to be stable against aging. The problems above dictated another approach which was developed by the members of the calibration task within the Pierre Auger collaboration. It is a paradigm of an end-to-end calibration of the whole telescope by one procedure using a well known source of light which is calibrated under laboratory conditions. The light source can then be put in the aperture of the telescope and emit a known number of photons so that one can measure the response of all PMTs and get the conversion factor (calibration constant) for each pixel. The detailed description of the light source will be given in the next section.

On the other hand, it is also possible to simulate fluorescence light from a cosmic ray shower by using a laser beam at a wavelength close to one from the nitrogen fluorescence spectrum. The laser is mobile and can be put in the field at some appropriate distance from a telescope eye. Members of the calibration task team of the Pierre Auger observatory performed laser calibration for several eyes of two telescope buildings in May 2005 and August 2006 using unpolarized laser light at 337 nm. The laser beam can only illuminate one column of pixels so it can only be used as an additional cross-check to the main calibration procedure described above. The uncertainties in the laser calibration add up to 12% including Mie and Rayleigh scattering and laser positioning and the biggest one of 11% being the laser energy. The laser calibration showed agreement with the main calibration within the uncertainty

above.

Relative calibration systems are implemented at each telescope to track time evolution of the calibration constants and provide calibration constants for any measurement night for any pixel. The relative calibration system for each mirror consists of three light sources (calibrations A, B and C) located at different points of the optical system. Calibration A has a Teflon diffuser installed in the middle of each mirror with the light being provided by a 470 nm LED via 6 optical cables to each of the mirrors. Calibration A is run before and after each night of data taking and consists of 50 rectangular pulses with the width of 57 μs. Calibration A provides tracking of the PMT response evolution.

The light sources for calibrations B and C are xenon flash lamps providing continuous spectrum. The light is focused with a lens and distributed via cables again to a certain position in the optical system. The fibers for calibration B split and end in two Teflon diffusers located on the sides of every camera, and the light from them is therefore directed towards mirrors and reflected back to be detected by cameras. The system for calibration B includes a filter wheel which approximates the full spectral acceptance of the telescopes with the filter centered at 330, 350, 370, 390 and 410 nm. Fibers for calibration C go outside the aperture so that the light is reflected back from some Tyvek® sheet reflectors positioned on the inside of the shutter. The light then goes back through the aperture. There is a filter wheel for calibration C as well which spans the acceptance spectrum at five different wavelengths so that the response of the detector could be monitored with time.

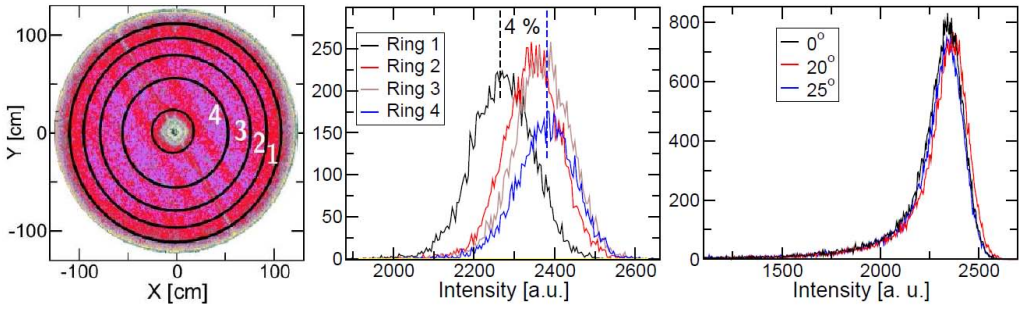

Figure 3.1 Measurements of the drum uniformity with a CCD camera. Left: CCD image of the drum at a normal viewing angle. Middle: Histogram of pixel intensities for different annular regions defined on the left image. Right: intensity independence for different viewing angles. See [102].

3.2 Absolute Calibration Light Source

To perform the absolute calibration of a whole telescope camera we use a large drum, 2.5 m in diameter and 1.4 meters deep, which has the front face made of Teflon. Teflon is a very good diffuser of light across a broad part of the spectrum including ultraviolet light. Each point on the drum face emits light in a uniform manner making the face a Lambertian source so that the light intensity does not depend on the viewing angle. The intensity of a surface element with an area A is $I_0 A\cos(\theta)$ where θ is the angle with respect to the normal to the surface and I_0 is the intensity in the direction of the normal. On the other hand, the area viewed at an angle θ from some distance d could be expressed as $A\cos(\theta) = d^2\omega$, where ω is the solid angle for which the area is seen from the distance d. As one can see then, the intensity is expressed as $I_0 d^2\omega$, and does not depend on the viewing angle. The uniformity of the light emitted by the surface is checked with a CCD camera by taking pictures at different viewing angles. Figure 3.1 shows the results of such a measurement suggesting good uniformity of $\pm 2\%$ and Lambertian property of the Teflon face surface across a region 2.2 m in diameter, the size of the telescope aperture. The drum can be put into the aperture of the fluorescence telescope and every PMT of the cameras will see the whole drum

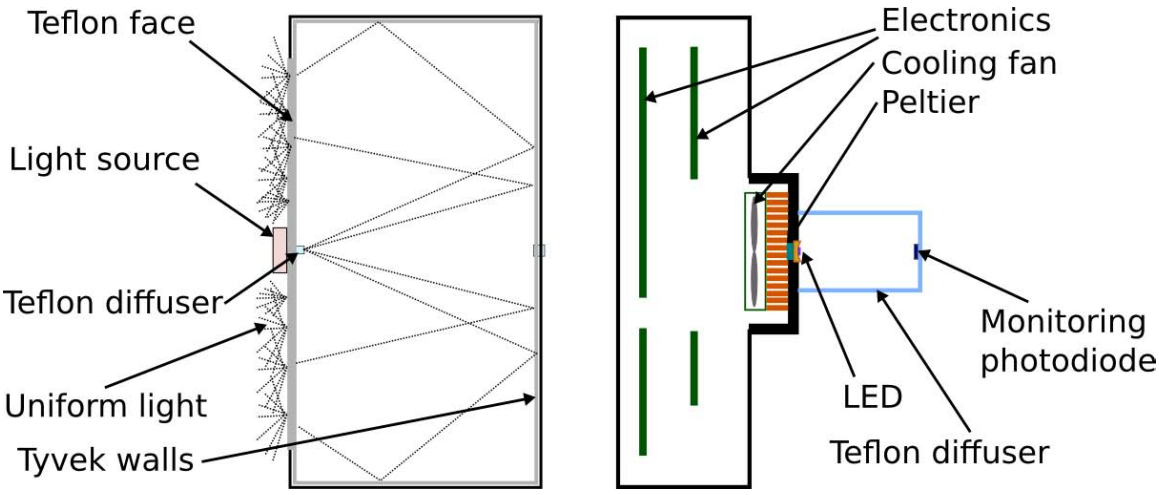

Figure 3.2 Schematics of the drum (left) and the light source (right) with the most important components shown.

face and will receive the same photon flux.

The inside of the drum is a hollow cylinder with the walls covered with Tyvek®, a material which reflects light diffusively. There are two holes in the drum, one is in the center of the front face and the other is in the center of the rear face. Each of the holes can be used to feed light into the drum. The light then gets reflected once or several times from the walls and then comes out from the Teflon front face into the telescope aperture. The intensity of the light that is fed into the drum should be adjusted in a such way that the output intensity is close to the intensity of light in the aperture produced by real atmospheric showers. Figure 3.2 shows the main components of the drum and the light source. The light source will be described in the next section.

We have used different light sources to illuminate the drum depending on the type of the calibration. Historically, different types of LEDs have been used for the absolute calibration at single wavelengths, at 375, 380 and finally at 365 nm. We used 365 nm high-power LEDs for the most recent absolute calibration campaigns in 2010. A xenon flasher is used for the multi-wavelength calibration across the whole region

of FD spectral acceptance. The xenon flasher feeds light into a monochromator which in turn is attached to the drum and feeds the light at a particular wavelength into it.

3.2.1 LED Light Source and Electronics

It turned out that the technique for the absolute calibration that has been used in the past (see [82, 102, 103]) had some drawbacks related to the use of LEDs in the direct current regime since the peak of intensity can shift upto 10 nm due to the heating of the LED junction and ambient temperature effects. Subsequent studies showed that this can be avoided by using the LED in the pulsed mode at all times and a Peltier device coupled to the LED for additional temperature stability. That required revision of the procedure which is now different than the one described in [104].

Custom electronics now control the LED. The electronics and the LED are enclosed in a single box called the light source which can be easily mounted on the drum. We use a 365 nm high-power LED by Nichia. The LED sits in a Teflon enclosure that provides uniform light illumination inside the drum. A Peltier unit is located just under the LED and has feedback from a thermistor so that it can keep the LED at constant temperature. A monitoring photodiode is placed in the middle of the enclosure so it can collect direct light from the LED. It has been shown that the area under LED pulses is stable within 0.5% in the pulsed regime if the Peltier controller is working.

The electronics consists of two main boards. The first one is a board which has a programmable logic device (PLD). The PLD allows driving four digital-to-analog converters (DACs). Each DAC can supply a current of up to 1A to an LED. The waveform of the signal is digitized at 100 mega samples per second with a memory buffer of 2048×16 bits meaning that one can shape the pulse form with different current values in 10 ns bins for the total length of up to $\sim$20 μs. The board also

has two analog-to-digital converters (ADCs) capable of digitizing a signal in 10 ns bins. The second board hosts a 600 MHz BlackFin BF537 processor and controls the PLD board. There is a Linux operating system installed on the second board and an Ethernet connection. A lightweight web server runs on the board so that one can submit pulse amplitude, duration and rate remotely via a web page. Only one DAC channel was used for the 365 LED in the course of the absolute calibration campaigns in 2010. The signals from a calibration PMT (see next section) and from the monitoring photodiode were read and digitized by two ADCs. ADCs have a constantly running buffer which saves individual pulse traces that can be then saved onto a remote computer via the network connection.

For the purposes of absolute calibration we used rectangular pulses with a width of 5 μs although pulses of other shapes have been tried as well: such as triangular, gaussian and very narrow 100 ns pulses, which allowed a test of the linearity of the FD PMTs and their after-pulsing. Figure 3.3 shows the web interface with a rectangular pulse submitted as well as response from the monitoring photodiode digitized by an ADC. We conducted linearity studies for different pulse amplitudes given in arbitrary units of the DAC, and the PMT response showed very good linearity in the whole range of possible DAC settings that we use for calibration pulses.

3.2.2 Absolute Calibration in Laboratory. Drum Intensity Measurement

The goal of the absolute calibration is to provide calibration constants or conversion factors between the absolute number of photons detected by a PMT and its digitized ADC response for every pixel of all cameras. Once the absolute calibration constants are known for the calibration night one can calculate them for any night of cosmic

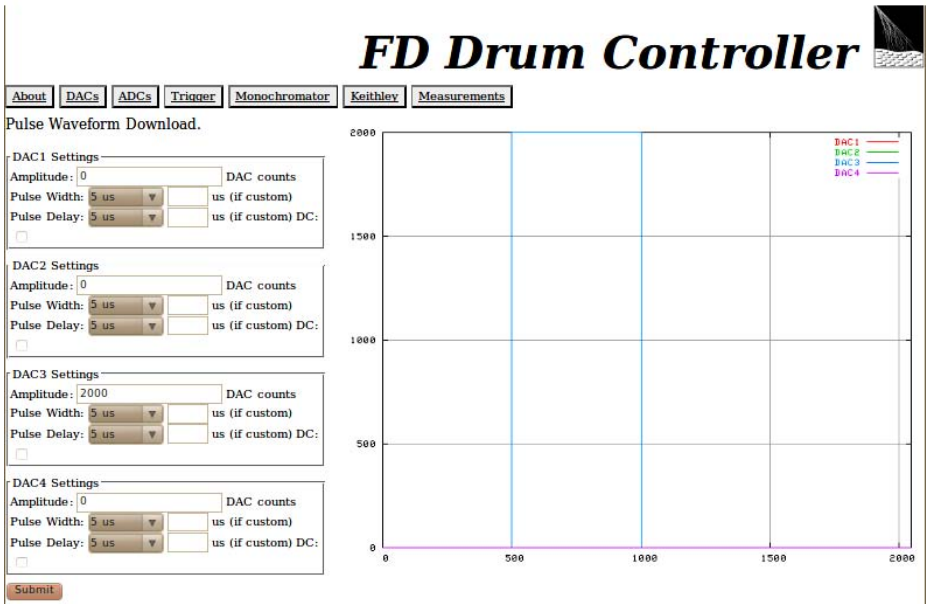

Figure 3.3 Web interface

ray data taking using relative tracking by Calibration A.

We use silicon photodiodes calibrated by the National Institute of Standards and Technology (NIST) to make an absolute measurement. One can easily convert charge collected by the NIST photodiode into the power or absolute number of photons per unit of time hitting the photodiode. The disadvantage of the photodiode is that its sensitivity is not nearly enough to measure the photon flux from the front surface of the drum. The design of the drum presumes that its intensity must be comparable with that of the fluorescence from real air showers in which case the sensitivity of the photodiode should be 5 orders of magnitude higher. We use a PMT to detect light pulses from the drum. One can measure arbitrary PMT response which then needs to be calibrated with the NIST photodiode. We solve this problem of matching the dynamic range between a PMT and a photodiode by using a long dark hall and the well known fact that electromagnetic radiation attenuates as $1/r^2$ with distance.

As the first step, we measure the intensity of the drum with a calibration PMT from a large distance of approximately 15 m in a long dark (meaning that there are

no light leaks that can affect the background photon flux) hall located at the Pierre Auger Observatory. Figure 3.4 shows the setup. The hall is connected to an optical table through a hole in the wall. The optical table has a movable top cover which makes it completely dark, and we call it a dark box. The PMT is mounted inside the dark box and with a viewing angle that only allows it to see the whole drum through the hole. From the distance of 15 meters the drum can be considered a point source. There are also curtains in the middle of the dark hall which play a role of baffles to fight specular reflections from the walls, ceiling and floor.

We pulse the drum 1000 times to collect sufficient statistics. The distribution of the pulse areas is gaussian with a mean value expressed in arbitrary units and proportional to the drum absolute intensity. Once this value has been measured we need to convert it into the absolute value of drum intensity. To do this we first perform a set of measurements of the light source intensity at different distances from the calibration PMT in the dark hall. The light source is taken out from the drum and is mounted on a rail so that it is at the same optical axis as the center of the drum. Figure 3.5 shows the setup in detail. The Teflon diffuser on the light source needs to be switched to a different one to allow for less light in order not to saturate the PMT but it is still a point source from the PMT point of view which means that its intensity must behave according to the $1/r^2$ law. We perform several measurements on the rail at different distances from the calibration PMT. All of the measurements fit the $1/r^2$ dependence quite nicely as shown on the left plot of Figure 3.6.

The last stage of the measurement occurs inside the dark box. We now take the light source from the rail and put it inside the dark box. The calibration PMT is replaced by the NIST calibrated photodiode and the distance from the light source is 1 m or less, so that an appreciable amount of charge can be collected by the photodiode and therefore it gives an absolute measurement. The light source is now mounted on

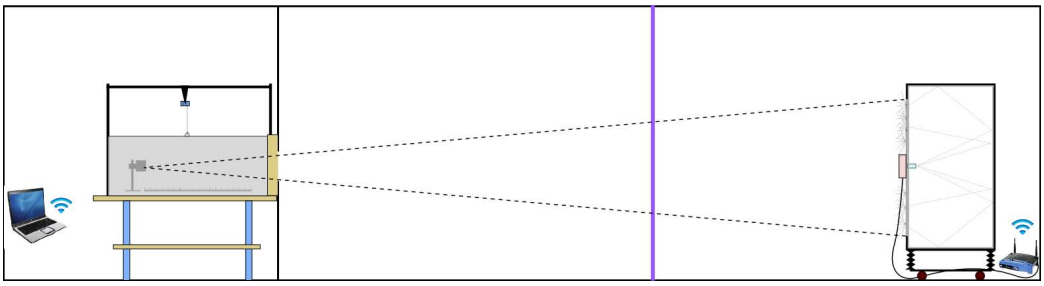

Figure 3.4 Dark hall in Malargue. Measurement of the drum intensity with a calibration PMT

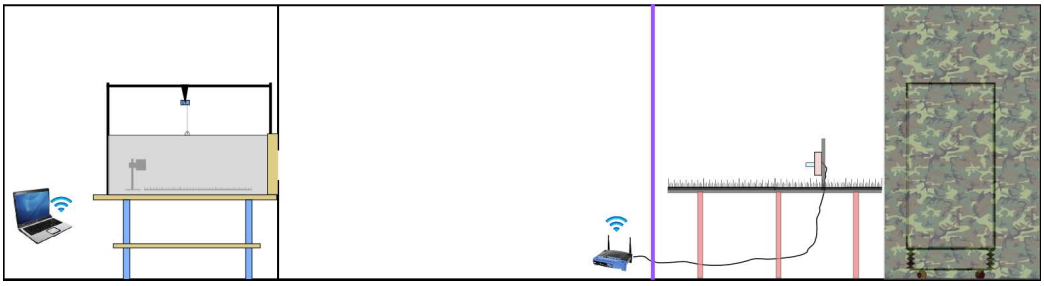

Figure 3.5 Measurement of the light source intensity on on the rail

a stand fixed to a mechanical actuator which can be controlled remotely, and the distance between the photodiode and the light source is read out digitally. Figure 3.7 shows the setup. We preform a series of measurements at the rate of 1 Khz and it has been shown that the total amount of the collected charge does not depend on the pulsing rate as shown on the right plot in Figure 3.8. We use a Keithley 6514 electrometer to measure collected charge and read it out digitally via a parallel port. The left plot in Figure 3.8 shows how the charge accumulates from the current of the NIST photodiode in steps of fraction of nC for each pulse of the LED.

The measurements are done at different distances from the NIST photodiode in 10 cm steps in the range where the light source behaves as a point source. An example of the results is shown on the right plot in Figure 3.6. This calibration work was done in June 2010 and the intensity scale is in absolute units of nC of the collected charge at different distances. The measurement can be transferred into the number

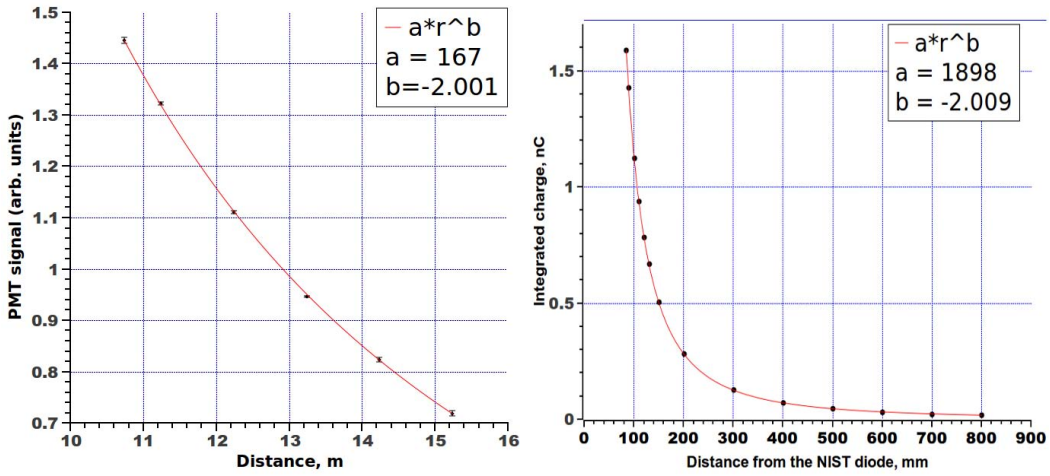

Figure 3.6 Left: light source intensity on the rail for different distances from the calibration PMT. Right: absolute measurement of the light source intensity

of photons per pulse. The measurement fits the $1/r^2$ law very well.

The last step to do is renormalization of the rail measurement so that arbitrary units are calibrated to the absolute measurement in the dark box. Thus it provides us with a conversion factor between the arbitrary units of the calibration PMT and the absolute measurement in nC of charge by the Keithley electrometer. Figure 3.9 summarizes the results of the calibration work done in the laboratory during the calibration campaign of June 2010. All of the measurements on the rail and from the dark box lie on the same curve that fits $1/r^2$ law very well. One can easily see the photodiode charge corresponding to the drum intensity. The measurement of the drum does not lie on the same curve since there is a change of the diffuser, although it is irrelevant since both the rail measurements and the drum intensity measurement are done with the same calibration PMT. Once we know the equivalent charge for the drum, one can calculate the absolute number of photons at 365 nm that are uniformly emitted by the drum front face per steradian per pulse.

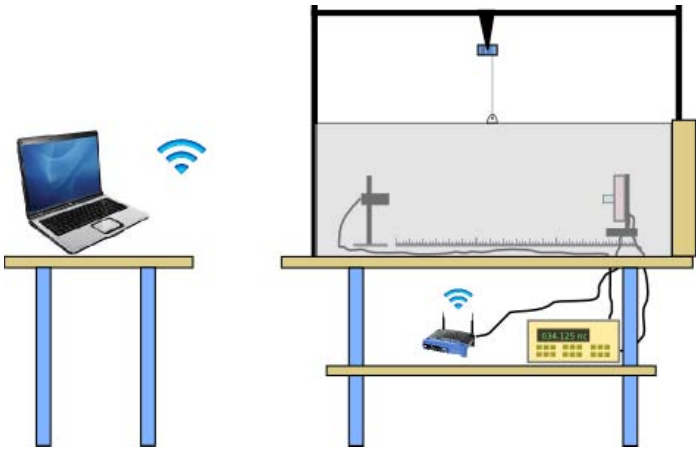

Figure 3.7 Absolute measurement of the light source intensity

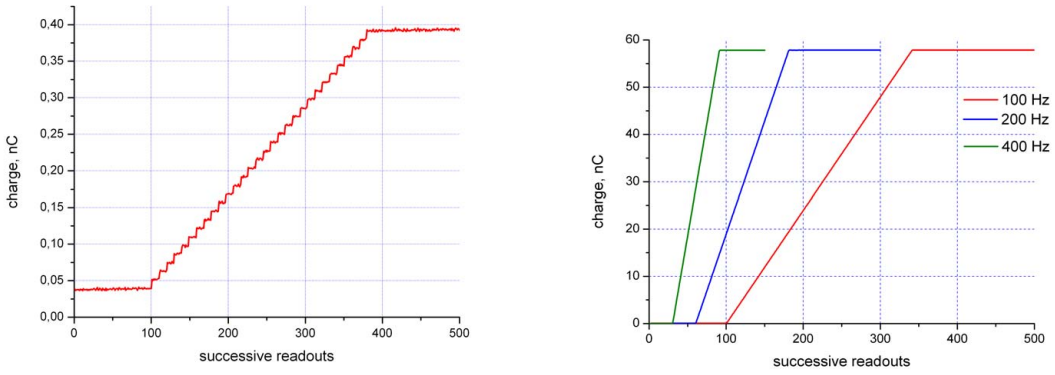

Figure 3.8 Integration of the NIST calibrated photodiode current using the Keithley 6514 electrometer in Q-mode. Left: 30 pulses of the LED at the rate of 1 Hz, and the sampling rate is faster than 1 Hz so one can see clear steps when each pulse happens and the accumulated charge increases. Right: 5000 pulses submitted at different rates illustrate independence of the total collected charge from the pulsing rate

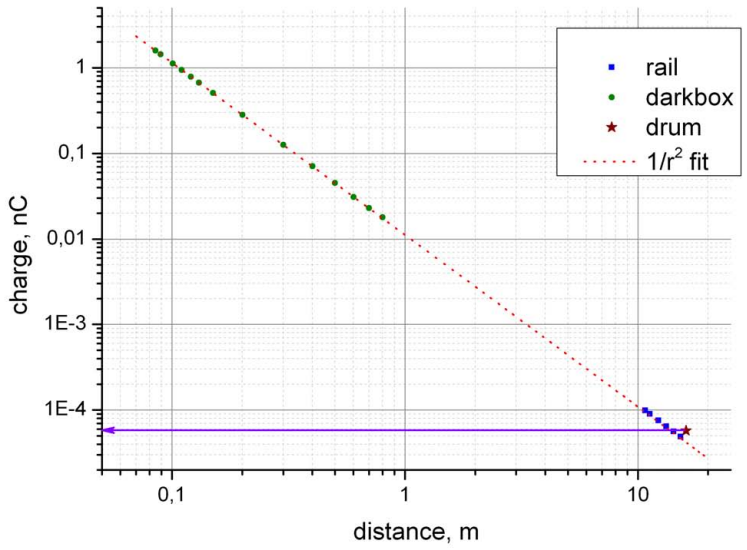

Figure 3.9 Summary of the measurements of the drum intensity from June 2010 calibration campaign plotted on the scale established by the curve from absolute measurements by the NIST photodiode. One can easily see the equivalent charge in nC for the drum

The drum intensity is expressed as follows:

$$I_D = \frac{< Q \times R_{PD}^2 >}{< H_{LS} \times R_{LS}^2 >} \times \frac{H_D \times R_D^2}{A_{PD} \times \int_\lambda E_{LED}(\lambda) \times \epsilon_{cal}(\lambda) d\lambda} \left[\frac{photons}{sr \times pulse} \right] \tag{3.1}$$

Equation (3.1) utilizes the fact that the product of the detector response and the squared distance between it and the light source should stay constant. Thus by measuring this constant quantity several times corresponding to different distances both on the rail and in the dark box, we can calculate the average and reduce the error. The term $< Q \times R_{PD}^2 >$ then corresponds to the set of measurements done in the dark box, whereas $< H_{LS} \times R_{LS}^2 >$ corresponds to the rail measurement. Their ratio provides the conversion factor which is the multiplied by the PMT response to the drum, $H_D \times R_D^2$. The area, A_{PD}, and the spectral response, ϵ_{cal}, of the calibration photodiode are provided by NIST. Finally, the energy of the LED photons is $E_{LED}(\lambda) = hc/\lambda$, and the integration takes into account broadening of approximately

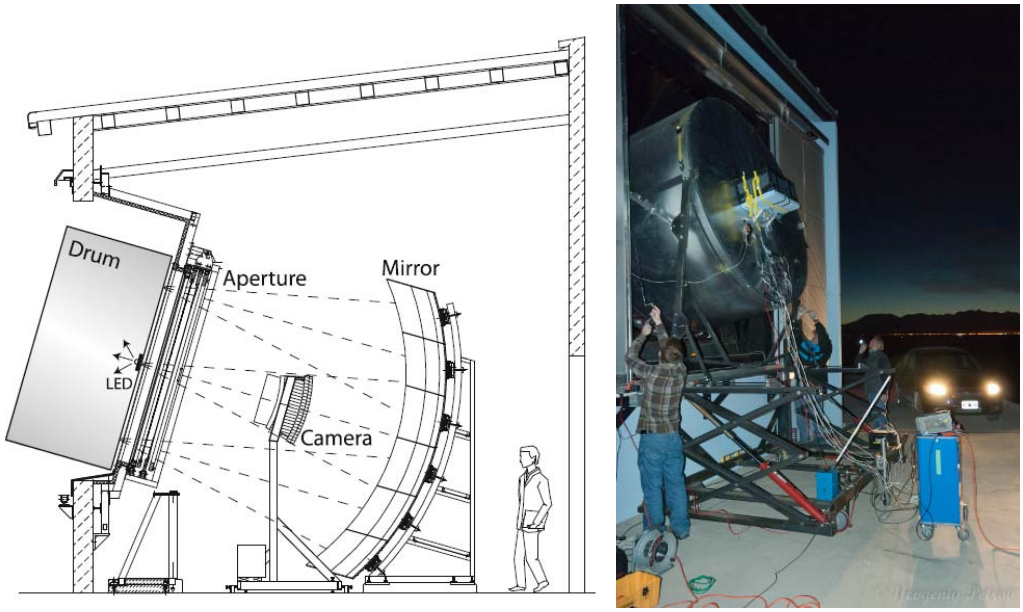

Figure 3.10 Absolute calibration light source, the "drum". Left: schematics of the drum in the telescope aperture (from [82]). Right: photograph of the drum being lowered into the aperture of one of the Los Leones telescope bays.

10 nm of the LED spectrum around the nominal value of 365 nm, which is a correction factor of 2.5% as opposed to considering the spectrum being a delta-function at 365 nm.

3.2.3 Calibration of Fluorescence Detectors

The last part of the absolute calibration at a single wavelength consists of taking the drum to all five fluorescence detector sites, putting it into the aperture and pulsing it with known intensity. The light source electronics provides the telescope electronics with an external TTL trigger so that all pulses are recorded. Figure 3.10 shows schematics and a picture of the drum lowered into the aperture of the telescope. The nominal pulse duration for the absolute calibration is 5 μs which was chosen historically due to necessity of getting statistically meaningful response from the FD PMTs when the lower-power 2 mW 375 nm LEDs were used. The upgrade of the

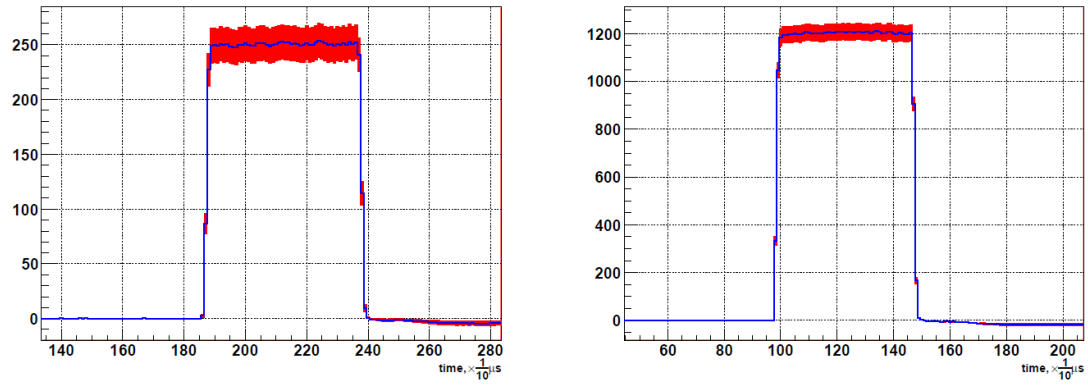

Figure 3.11 An example of average response by the FD PMTs to 400 drum pulses. Left: old calibration in 2005 with a lower-power 375 nm LED. Right: new calibration after electronics and LED upgrade to high-power 365 nm LED. The RMS spread in each time bin is shown in red.

light source LED to 0.3 W 365 nm LEDs allowed for getting a higher response from the PMTs and better statistics. Figure 3.11 compares the response by the FD PMTs to the old (left) and new (right) LED.

Another important step of the calibration in the field is to flat-field the cameras periodically. Flat-fielding is done by electronic adjustment of the PMT gains in the camera so that the response of the PMTs is uniform across the whole camera and there are no big outliers.

One calibration campaign lasts for about two weeks. In the course of the campaign all of telescope buildings are calibrated with 1-2 nights spent at each building and intermediate checks in the dark hall to measure the drum intensity and ensure its stability in the course of the campaign. We performed the most recent absolute calibration with the upgraded light source in the course of three campaigns in 2010. All four main telescope sites were calibrated in January and then another time in June except Loma Amarilla which was not operating due to a severe lightning strike in April. Loma Amarilla and three telescope of the HEAT extension were calibrated successfully in November.

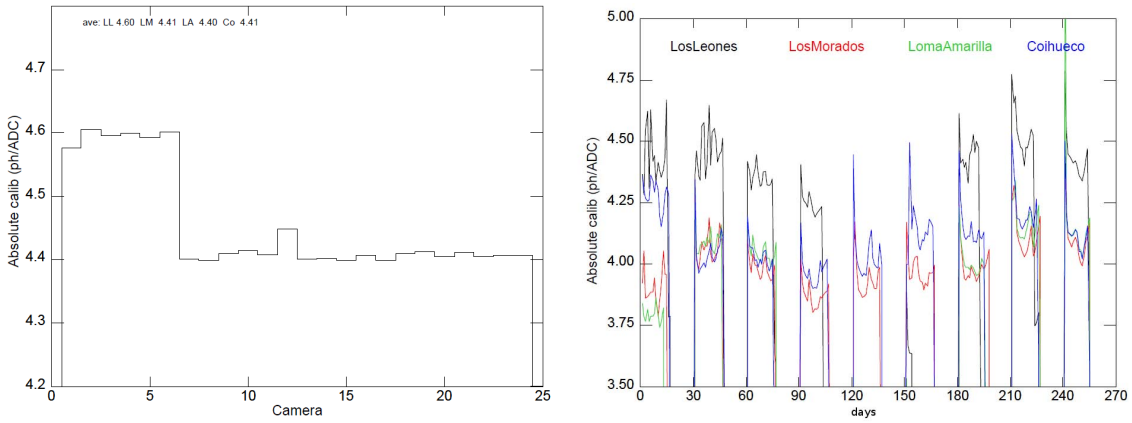

Figure 3.12 Left: average absolute calibration constants for all 24 main fluorescence telescopes. The change of 5.7% between the first six telescopes and the rest has been precisely measured and is due to the changes done in the laboratory to the light source. Right: an example of the tracking of the calibration constants by the ratio of nightly Calibration A for the period of nine months since January 2011. The plots are taken from [105].

3.3 Absolute Calibration Results

We analyze the FD response by integrating the area under each pulse for all pixels in the cameras and then getting an average response from a large number of pulses (400 in practice) after background subtraction. On the other hand, knowing the drum absolute intensity and geometry of the drum and the camera, one can calculate how many photons hit each PMT per pulse in its solid angle. It yields the calibration constants for each pixel in all cameras expressed as number of photons per ADC count. To see the behavior of all cameras we plot calibration constants averaged over 440 pixels of each camera and 400 pulses. The left plot of the Figure 3.12 shows average calibration constants for all cameras after the January 2010 calibration. The flat-fielding was done and one can see relatively flat response across all cameras in all telescopes. The discontinuity of 5.7% between the first 6 telescopes of Los Leones and the 7th telescope at Los Morados is caused by the change which was made in between field calibrations to the light source in the lab. This discontinuity was investigated

and accounted for in the successive calibration campaign in June 2010. Of course, each PMT has its own individual constant. There is a calibration database that keeps track of all constants for all pixels and tracks their evolution with time using the ratio of the FD response to Calibration A for particular nights of real shower measurements and Calibration A done at the time of calibration. The right plot of Figure 3.12 illustrates how Calibration A tracks the FD response over time and can follow the seasonal effects, PMT degradation and any other changes. For example, the lightning strike at Loma Amarilla site causes calibration constants to be completely off-scale for a while before everything was repaired.

3.4 Systematic Uncertainties

The following factors give rise to the systematic uncertainty of the absolute calibration: generic light source uncertainty, uncertainty associated with the replaceable diffuser on the light source, Teflon has the temperature dependence of transmittance, uncertainties on the measurements of the drum intensity with the PMT, on the rail and in the dark box, uncertainties in the calibration of NIST photodiode provided by NIST, uncertainties in the calibration of the electrometer and its readout; and finally there are uncertainties associated with the calibration at the telescopes: calculation of the area under FD pulses, reflections in the camera and uncertainty from the overlap between the LED spectrum centered around 365 nm and the shape of the camera acceptance. All of these factors are summarized in Table 3.1, where we combine them in quadrature. The final systematic uncertainty is then 5%.

Table 3.1 Systematic uncertainties of the absolute calibration

Calibration stage	Quantity	Uncertainty (%)
Drum setup	Light source stability	0.5
	Diffuser	2.0
	Teflon temperature dependence	1.0
$\frac{1}{r^2}$ measurement	Dark box measurement	0.2
	Rail measurement	1.0
	Drum intensity measurement	0.6
NIST Photodiode	NIST calibration	1.0
	Active area	0.1
FD data analysis	Pulse area	3.0
Camera aperture effects	Reflections	2.0
	Convolution between FD acceptance and LED spectrum	1.0
Total		5.0

Chapter 4

Energy and Arrival Direction Reconstruction of Ultra High Energy Cosmic Rays

The Pierre Auger Observatory is a hybrid detector which combines large statistics of the data collected by the surface detector and calorimetric measurement performed by the fluorescence detector. The dataset of events when they are detected by both the surface and fluorescence detectors is called hybrid. The energy of the events detected by the surface detector is calibrated using the energy measurement from the fluorescence detector. In this chapter I will describe how the hybrid reconstruction is done and how the surface detector energy scale is then calibrated to the energy from the fluorescence measurement.

4.1 Hybrid Reconstruction

Figure 2.5 shows how an EAS is detected by many pixels along the shower axis. The first step of the reconstruction is determining the geometry of the shower. The red line on the figure is the intersection of the camera surface with the so called shower-detector plane (SDP). The pointing directions of the triggered pixels must converge on the shower axis and the red line represents the best fit with the pointing directions

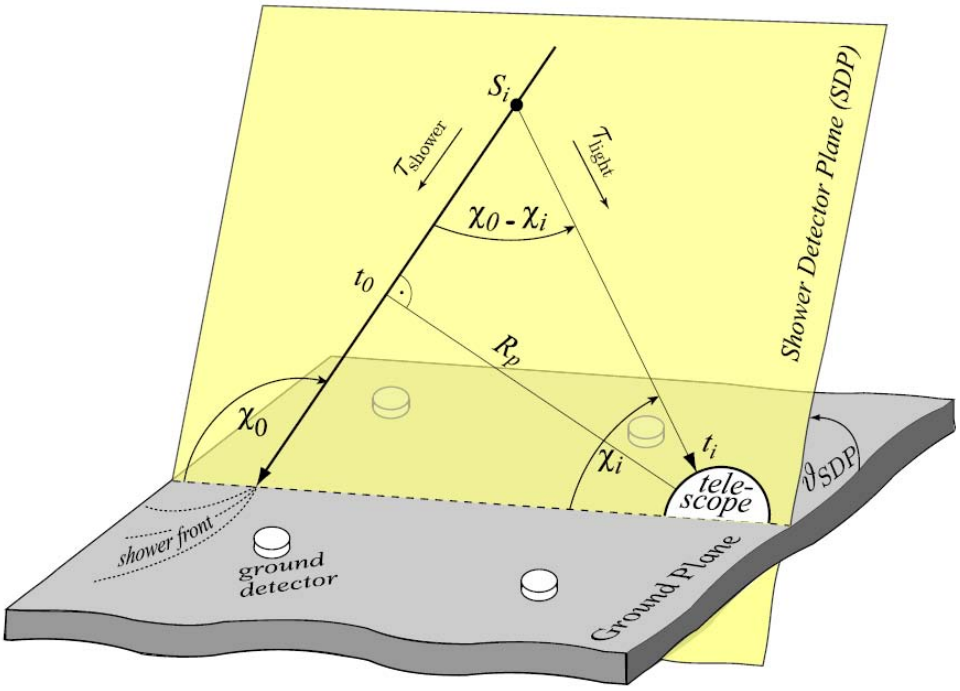

Figure 4.1 Surface detector plane geometry and reconstruction of the position of a shower axis. From [106]

being the closest distance to the SDP. The uncertainty in the angular orientation of the SDP is determined by comparing with the well known geometry reconstructed with the laser shots by the central laser facility. The uncertainty in the SDP is 0.1-0.2 degrees. Once the SDP is established one needs to know the orientation of the shower axis in this plane. Figure 4.1 shows the geometry of the SDP and a possible orientation of a shower axis. The axis can be unambiguously defined by the shortest distance to the telescope, R_p, and by the angle χ_0 which it makes with the horizontal plane. Each pixel pointing direction makes an angle χ_i with the horizontal plane and, as one can see, an angle of $\chi_0 - \chi_i$ with the shower axis. One can show that the fluorescence light from a point S_i on the axis arrives at the i-th pixel at time, t_i, which is expressed as:

$$t_i = t_0 + \frac{R_p}{c} \tan\left(\frac{\chi_0 - \chi_i}{2}\right), \tag{4.1}$$

where t_0 is defined as the time when the shower front passes at the distance R_p from the detector. To determine the t_0, R_p and χ_0 parameters, one determines a best-fit with χ^2 minimization between the expected t_i, χ_i and observed ones. Once we know the shower geometry parameters above, we can also convert them into impact point, where the shower axis cross the horizontal plane, arrival direction and ground impact time. The assumptions used to derive equation (4.1) are the following: the shower disk is approximated as a point moving at the speed of light, the fluorescence light is emitted instantaneously and propagates with the speed of light in vacuum and along a straight line without any scattering. An analysis in [106] shows that the uncertainty in timing due to those approximations is of the order of 100 ns which translates into a typical angular uncertainty of 0.05° but in some case could be up to 0.1°. This kind of uncertainty cannot affect the results significantly in this dissertation since the angular window that I use for the analysis is much bigger (see Chapter 6).

The problem with the reconstruction according to the equation (4.1) arises from the fact that for some showers (for example, for small angles between the shower axis and telescope eye axis), the angle χ does not change fast enough over the whole track length in a camera meaning that all the measured χ_i and t_i are grouped together so that the fit becomes degenerate. This situation is shown on the Figure 4.2. The red line shows a fit done using the FD data only. There are multiple curves one could fit the FD data with.

The hybrid reconstruction allows for breaking this degeneracy by using the timing information from the surface stations that trigger for the same event. The blue curve in the Figure 4.2 shows the geometry reconstruction with the SD data included in the fit. Most of the events that are seen by the telescopes also trigger the SD, except some with energies too low to trigger the SD, but in that case the trigger is sent from the FD allowing for the hybrid reconstruction. A specific analysis devoted to the angular

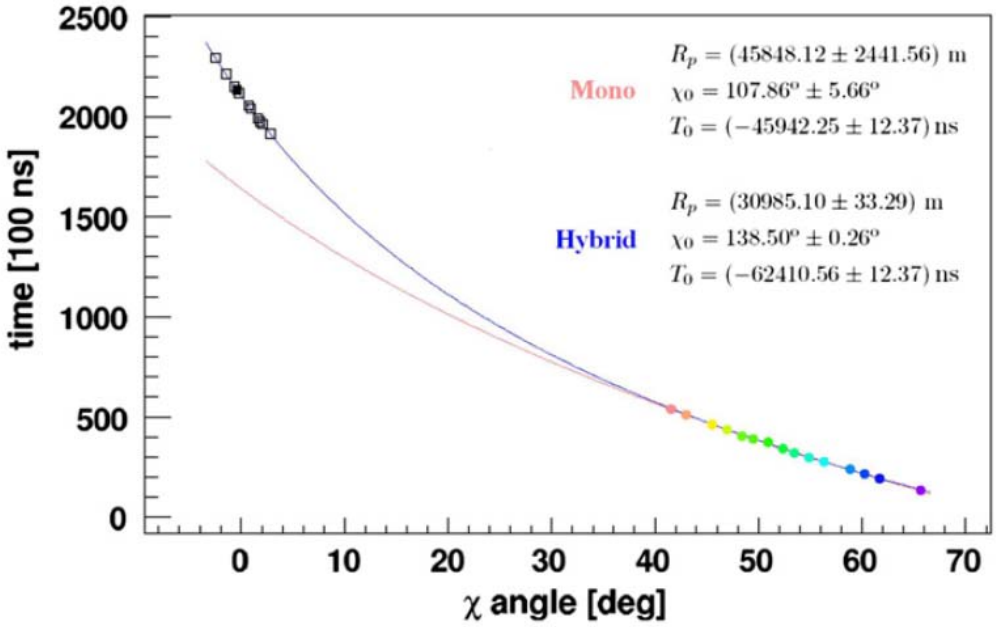

Figure 4.2 Principle of the hybrid reconstruction. Color points represent the data from the FD. Black squares is the SD data. From [82]

resolution of both the fluorescence and surface detectors has been done in [107]. The angular uncertainty of the hybrid reconstruction of the arrival directions depends on the energy and goes down from 0.8° at $10^{17.5}$ eV to 0.6° at 10^{18} eV and to 0.5° at 10^{19} eV.

The next step of the reconstruction is determining the energy deposited by the shower in the atmosphere and ultimately the energy of the primary particle. One can calculate the deposited energy from the signal in the triggered camera pixels and by taking into account light attenuation in the atmosphere. Besides direct fluorescence light there is also a fraction of Cherenkov light both direct and scattered as well as multiple-scattered fluorescence that contribute to the signal. The details of the longitudinal profile and energy reconstruction are given in [108]. Here I only give a brief description. Figure 4.3 shows an example of the reconstruction. One starts with the absolute photon flux at different times as the shower front moves across the

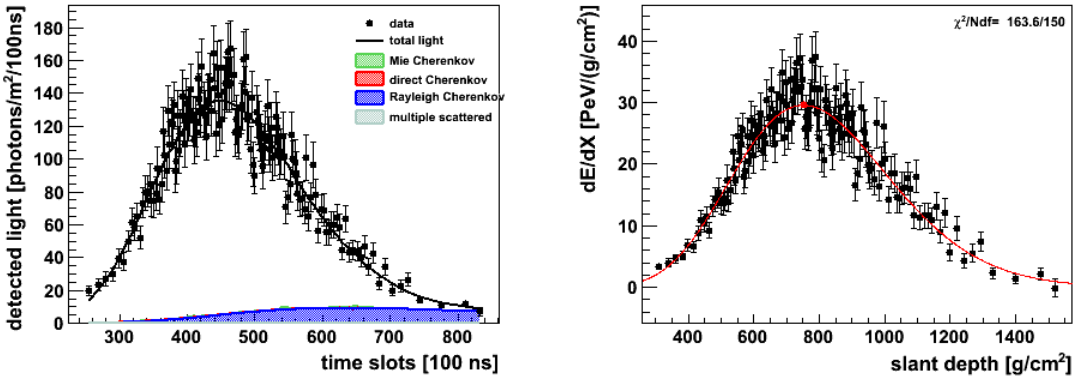

Figure 4.3 Example of a reconstruction of a real shower. Left: measurement of the light collected by the pixels along with different contributions from other sources. Right: reconstructed energy deposit along the shower axis where the red line is a Gaisser-Hillas fit. The energy of this shower was $(1.94\pm0.09)\times10^{19}$ eV and X_{max}=752±11 g/cm^2

camera (or several adjacent cameras). Also, different contributions of the Cherenkov light and multiple scattering are shown. After subtracting those contributions we can calculate the energy deposited per unit of slant depth along the shower axis as shown on the right plot, the shower energy profile. The total energy deposited in the atmosphere by the fluorescence light could be found if we integrate the profile. At first, the profile is fitted with so called Gaisser-Hillas function introduced in [109]. It has been shown in [110] that it is well suited to describe the longitudinal profile of an EAS. The function has the from of:

$$f(X) = w_{max}\left(\frac{X - X_0}{X_{max} - X_0}\right)^{(X_{max}-X_0)/\lambda} e^{(X_{max}-X)/\lambda}, \tag{4.2}$$

where w_{max} is the maximum energy deposit that occurs at the shower maximum, X_{max}. Also, there are two parameters, X_0 and λ, responsible for the shape of the curve. The best fit is based on χ^2 minimization between the experimental points shown as black squares in the figure and the Gaisser-Hillas function. The energy reconstructed by integrating the fit is not quite the total energy of the primary particle yet, since a part of the energy is carried away by neutrinos and high energy muons.

This contribution is estimated based on shower simulations and has been shown to be on the order of few percent for different composition of the primaries [111]. This contribution is added to finally get the total energy of the shower or the energy of the primary particle.

The total systematic uncertainty of the energy measurement by the fluorescence detector adds up from the fluorescence yield (14%), reconstruction uncertainty (10%) and finally the absolute calibration, which used to be quoted as 9% but has been reduced to 5% with the new calibration describe in the previous chapter. The total systematic uncertainty on the energy scale is therefore 18% adding in quadrature.

4.2 Reconstruction of Arrival Direction and Energy by Surface Detector.

4.2.1 Arrival Direction

The vast majority of the observatory events are surface detector events only. One needs to reconstruct their arrival directions and shower size using the data from the surface detector alone. The reconstruction of arrival direction is purely geometrical and is based on fitting the timing of the signals at different WCDs as a shower front passes though them. It is is an iterative process. In the first approximation, the shower front can be considered as a plane perpendicular to the shower axis. By minimizing the χ^2 of timing at different triggered stations, one can determine the orientation of the shower plane with respect to the local horizontal coordinate system[1].

[1]The horizontal coordinate system uses azimuth, ϕ, and zenith angle, θ, (or alternatively, elevation above the horizon)

The point where a shower axis intercepts the ground is called a shower core. In the first approximation, a shower core is found as a spatial weighted average of the signal in the triggered stations. Once an approximate orientation of the shower axis and the core position are known, another fit is done with more realistic shape of the shower front, a parabola. The χ^2 is minimized again and the direction of the shower axis, same as the arrival direction of the primary particle, is found in terms of the azimuthal and zenith angles in the local horizontal coordinates.

The angular resolution is defined as an angular window around an imaginary point source on the sky so that it contains 68% of the arrival directions of the showers originating from that source. The angular resolution of the surface detector also depends on the energy since the number of triggered stations increases with the energy. The analysis in [107] concludes that the angular resolution is better than 1° for high multiplicity events which have more than 5 triggered stations, and energy above 10 EeV. This is the energy range that is considered in the current work. The angular resolution does not affect the results that are presented below in Chapter 6.

4.2.2 Shower size and Energy Calibration

Footprints of showers induced by the UHECRs occupy a very large area on the ground. The lateral particle density, i.e. the density of particles in the plane perpendicular to the shower axis, at any stage of the shower development, and on the ground in particular, can be described by the lateral distribution function (LDF). The integral of the LDF gives the total number of particles at that stage. Economic constraints dictate that for large surface arrays one can only sample particle density by measuring signals at several triggered stations inside the shower footprint. Figure 4.4 shows an example of the signals recorded in WCDs at different distances from the core. Knowledge of the exact LDF would give the total number of particles and therefore

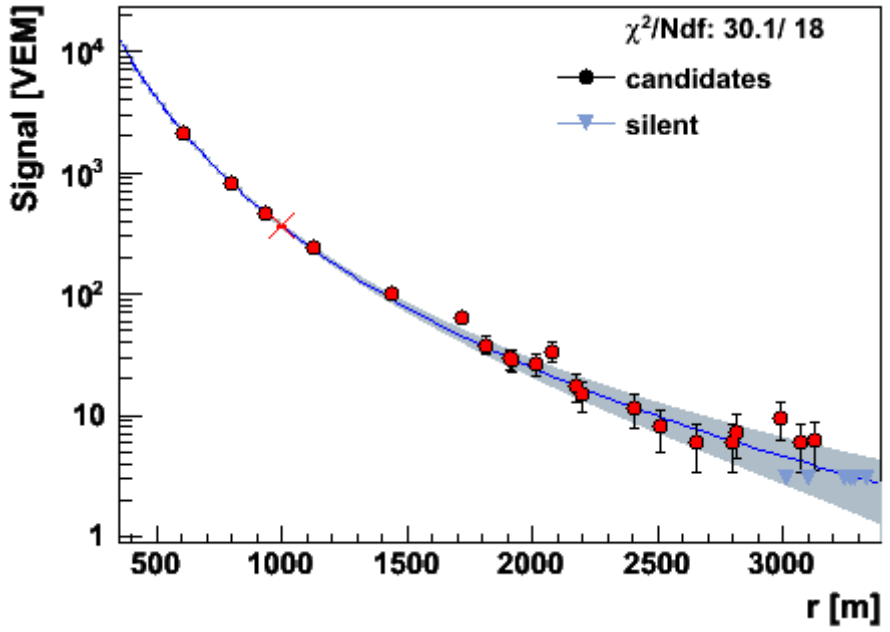

Figure 4.4 Example an event detected by the surface detector. The signal values at the triggered station are shown as red dots along with the LDF fit (blue line) with a functional form given by the equation (4.3). The signal at 1000 meters is marked with a red cross.

the size of the shower, from which one can deduce the energy of the primary particle.

The main difficulty is that the exact form of the LDF is unknown and one can fit many different functional forms given the experimental data points in Figure 4.4. Fortunately one does not need to know the exact form of the function. Hillas [112] showed that one can use a signal value at some particular distance from the shower core from which the shower size can be calculated. The signal fluctuates very little at that optimal distance and does not depend much on the LDF shape. The signal at that distance is determined by the geometry of the surface detector. It has been shown in [113] that this distance is close to 1000 m in the case of the Pierre Auger Observatory with its triangular grid and 1500 m separation between the WCDs. Figure 1 in [113] illustrates that the signal at the optimum distance stays constant

for different possible LDF fits. Combination of the T5 fiducial trigger and the fact that the separation between adjacent WCDs is 1500 m ensures that the signal at 1000 m from the core could be always found by interpolation of the signals in triggered stations. The signal at 1000 m is denoted as $S(1000)$. To find the numerical value of the $S(1000)$ one needs to choose a form of the LDF to use. In the case of the Pierre Auger Observatory the LDF of choice is a "NKG" function introduced by Nishimura, Kamata [114] and Greisen [115]. It has the following form:

$$S(r) = S(1000) \left(\frac{r}{1000}\right) \left(\frac{r+700}{1700}\right)^{\beta}. \tag{4.3}$$

A χ^2 minimization is done between measured signals and signals predicted by the LDF in equation (4.3) to find the best fit, and the value $S(1000)$ is interpolated from it. Once the signal $S(1000)$ is known from the fit, one can relate the the size of the shower and the energy of the primary particle. It is done based on a Monte Carlo simulation of the shower development in the case of a purely surface detector. The Pierre Auger Observatory is different in this sense since it is a hybrid detector. It is possible to calibrate $S(1000)$ with a calorimetric measurement of the energy by the fluorescence detector. The most recent update of the energy calibration is described in [116]. I will describe the main steps below.

Showers attenuate in the atmosphere. Thus S(1000) depends on the slant depth at some stage of development, and that translates into dependence on the zenith angle. This dependence is called an attenuation curve. The constant intensity cut (CIC) method is used to extract the shape of the attenuation curve from the data. The description of the method can be found in [116, 117]. The method is based on an assumption that the flux of the cosmic rays is isotropic[2] and the geometric acceptance of the Pierre Auger Observatory is known above the energy where the detector is fully

[2]The isotropy of the flux (at least at the energies below 50 EeV) is supported by the observations [118]

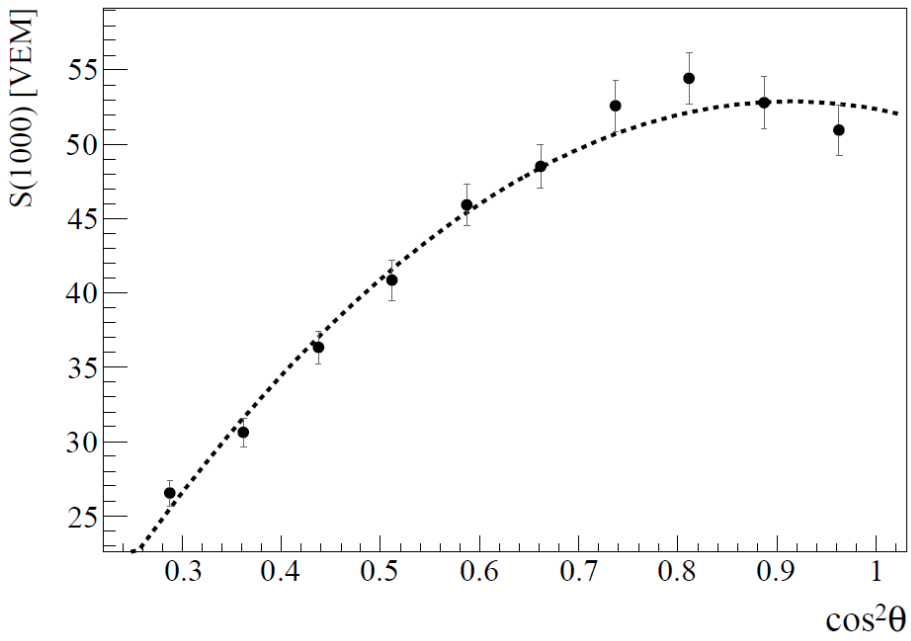

Figure 4.5 Attenuation curve for the Auger surface detector data for the vertical showers. The fit is done with $x = \cos^2(\theta)\cos^2(38°)$. From [116]

efficient. Isotropy of the flux leads to the fact that it is the same number of events that is detected for different zenith angles above a certain energy but their $S(1000)$ values are different due to attenuation. The distribution of events in zenith angle is proportional to $\sin(\theta)\cos(\theta)$ which follows from an expression for the area of an infinitesimal element of a spherical surface in spherical coordinates and from the projection of the detector plane perpendicularly to a shower axis. It means that it is constant with respect to $\sin^2(\theta)$. If one defines the intensity as the number of events with $S(1000)$ above a certain value per unit of $\sin^2(\theta)$ then it naturally decreases with $S(1000)$. One can plot intensity curves as a function of the cut in $S(1000)$ for different bins of the zenith angle and then extract attenuation curve taking $S(1000)$ values for different zenith angle bins but for the same intensity.

The attenuation curve is shown in Figure 4.5 as the value of $S(1000)$ for different bins in zenith angle. One can do a fit to the points and relate $S(1000)$ to any reference

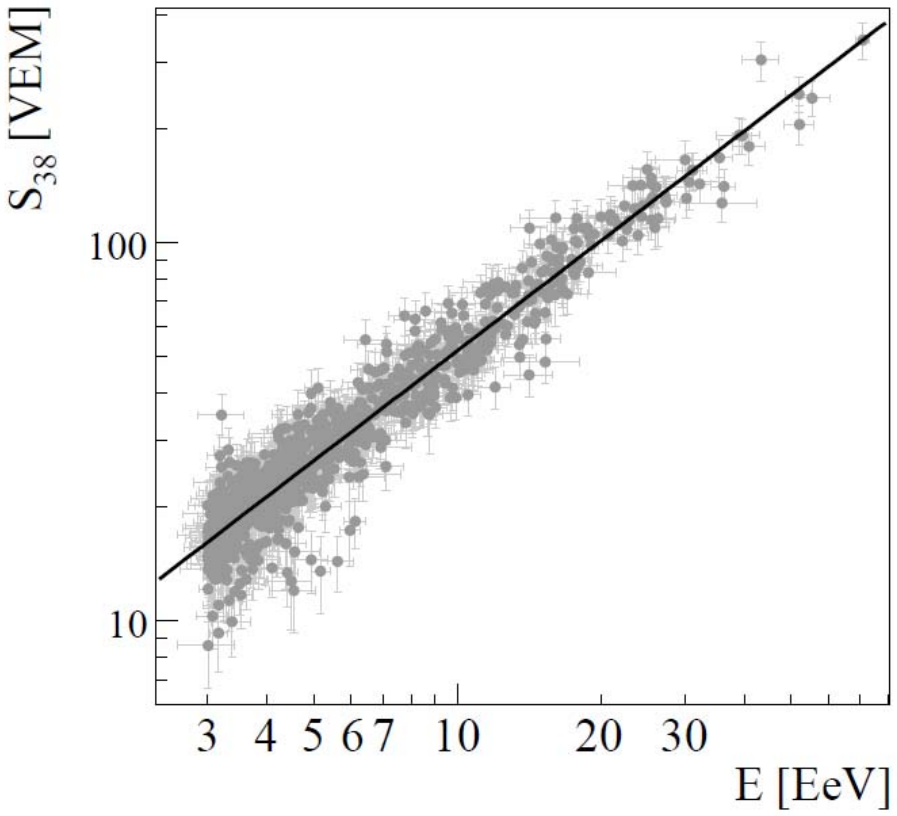

Figure 4.6 Correlation between SD and FD energy estimators. From [116]

signal for some zenith angle. The Pierre Auger Collaboration chose this angle to be the median of the distribution of the real vertical events in zenith angle that equals to 38°. The fit is also shown at the Figure 4.5. The fitted attenuation curve, $CIC(\theta)$, can be used for any event to convert its $S(1000)$ into $S_{38} \equiv S(1000)/CIC(\theta)$ where $CIC(\theta) = 1 + ax + bx^2$, $x = \cos^2(\theta) - \cos^2(38°)$ with a and b being parameters of the fit. The last step of finding the energy is calibration of S_{38} with the energy given by the calorimetric measurement from the FD. Hybrid events are used for the calibration with a series of cuts applied to them to ensure good quality of the sample (see [116] for details). The sample is composed of "golden" hybrid events defined as events, for which an energy estimator can be reconstructed independently from both the SD and FD data. There are 839 hybrid events that are used in the calibration.

The correlation between $S(1000)$ and the energy from the FD is shown in Figure 4.6. The best fit is a power law, $E_{FD} = AS_{38}^{B}$ where $A = (1.68 \pm 0.05) \times 10^{17}$ eV and $B = 1.035 \pm 0.009$ according to the most recent analysis reported in [116].

The systematic uncertainty of the SD energy scale translates from the FD systematic energy uncertainty which was given in the previous chapter. The energy resolution depends on the energy range as one can see from Figure 4.6 and is quoted in [116]. The energy uncertainty decreases from ≈16% for the events just above 3 EeV to 12% for events above 10 EeV.

Chapter 5

Galactic Magnetic Field and Its Influence on Propagation of Ultra High Energy Cosmic Rays

The first two sections of this chapter give background on the subject of the galactic magnetic field. The current state of the theory and measurements are described. The third section describes the recommended constraints on the galactic magnetic field from different astronomical measurements. Finally, the last section introduces the models of the galactic magnetic field that will be used in the current work.

5.1 Origins of Galactic Magnetic Field

There are two theories that explain the origin of the large-scale galactic field, mean field dynamo theory and primordial field theory. They both consider evolution of the Galaxy and magnetic field formation starting from the time when the Milky Way was formed 13.6±0.8 billion years ago [119]. Reviewing at the history of the research in this area one can say that both approaches were independent at first and both of them encountered a problem explaining the origin of the "seed" fields needed for both models. This fact as well as the possibility for the dynamo mechanism to play an essential role in the field enhancement in any scenario leads to a combined point

of view where elements of the two approaches are currently merging to provide a coherent picture of the origin and evolution of the galactic magnetic field [120]. Let us now consider the first and most developed theory, the dynamo action, which has been successfully applied not only to galactic fields but also to magnetism of the Earth and Sun as well as to plasma behavior in laboratory fusion experiments.

The galactic dynamo theory was independently proposed by Parker [121, 122] and Vainshtein and Ruzmaikin [123]. It states that the field was formed by a turbulent dynamo mechanism through amplification of some initial "seed" fields pre-existing in the matter that later formed the Galaxy (so called protogalaxy). After formation of the Galaxy, the mean field dynamo existed in the galactic interstellar medium where two types of motion were present: toroidal differential rotation around the Galactic center; and cyclonic motions triggered by supernova explosions. Qualitatively the process might be explained as follows [124, 125]. Let us assume there was a weak magnetic field with the magnitude of about 10^{-2} μG coherent at the scale of the protogalaxy. The protogalaxy is usually modeled as a uniform ball of neutral gas and plasma with the diameter approximately 10 times larger than the current diameter of the Galaxy, which is 30 kpc.

Interstellar plasma motion is governed by the equations of magnetohydrodynamics. For a moving conducting medium Ohm's law is expressed as $\mathbf{E} + \mathbf{U} \times \mathbf{B} = \eta \mathbf{J}$. Interstellar plasma can be shown to have very low resistivity η [126, p. 175] and so the right hand side of the Ohm's law becomes zero. Under this condition, it can be easily shown by using Faraday's law and Stoke's theorem that the magnetic flux through any closed loop stays constant as any part of the loop moves along with the plasma velocity $\mathbf{U}$. In other words, the density of the magnetic field lines remains the same throughout the plasma volume, so-called "flux freezing."

Once the protogalaxy has collapsed into a galactic disk, its magnetic field, which

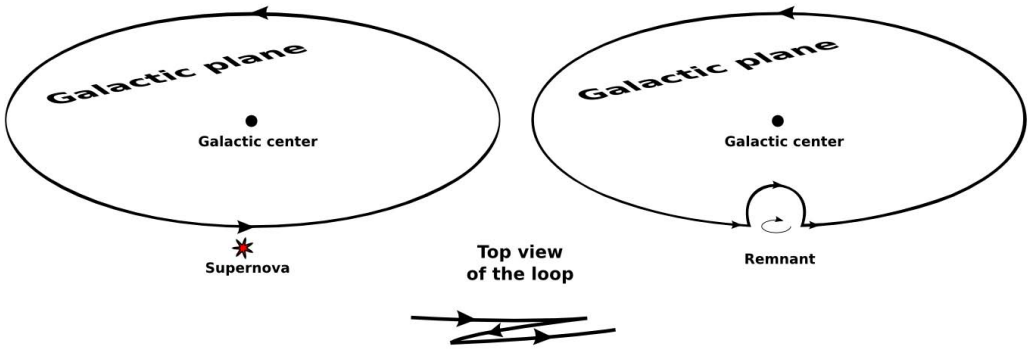

Figure 5.1 Magnetic field amplification in the Galaxy

is frozen in the interstellar plasma, gains an azimuthal, or else called toroidal, component due to differential rotation of the galactic matter. Let us consider a single field line going in the toroidal direction. It turns out that cyclonic motions due to supernovae provide crucial conditions necessary for the magnetic field amplification. If a supernova explodes below the magnetic field line, the line then becomes expelled above the original path and forms a loop following the supernova remnant boundary. The remnant material rotates with the Galaxy before the explosion, and following the explosion its rotation is slowed down by the fast expansion when the moment of inertia quickly grows. This causes the end points of the loop to rotate so that there is a negative radial component of the velocity at the beginning of the loop and a positive one at the end. The process is shown schematically in Figure 5.1. After that, differential rotation makes the beginning point move faster than the end of the loop, and it now causes the original line to go back and forth, twice in the same direction and once in the opposite if looking from top. The part of the line that has opposite direction lies above the plane formed by the original toroidal line. If the supernova remnant is powerful enough, it can expel this piece of the line leaving essentially doubled magnetic field in the galactic plane. This process of the field folding can be repeated with another supernova remnant and so on.

Quantitative description of the formation of the galactic magnetic field is based on the magnetic differential equation which can be derived from the Maxwell equations. By splitting the magnetic field vector and gas velocity into mean and turbulent parts it then becomes possible to solve the magnetic differential equation for the mean field. The solutions describe drag of the field lines as well as the cyclonic motions resulting in the field amplification [127]. Also, there are both symmetric and antisymmetric solutions with respect to the galactic plane and these symmetries are reflected in the names of the different models of the galactic magnetic field which will be introduced later in this chapter.

The primordial field theory was originally proposed by Fermi in 1949 [60]. Recent detailed simulations are described in [128]. In short, the theory assumes existence of a non-uniform primordial magnetic field with the magnitude of $10^{-6}\mu$G [124, 125]. The linear size of the region of the primordial field ($\sim$100kpc) is an order of magnitude larger than the current size of the Galaxy ($\sim$10kpc) so that the primordial field gets amplified by a factor of 10^5 during the collapse in which the Galaxy forms. First, the spherical protogalaxy collapses into a smaller sphere (10kpc) which gives a factor of 1000 amplification, and then further collapse adds a factor of 100 since the final state is a disk of the same diameter but with a thickness of 100 pc. Differential rotation takes over after that and amplifies the field to its current values.

In conclusion, both theories described above encounter difficulties in explaining not the amplification mechanisms themselves but the initial conditions required by those mechanisms to get the currently observed coherent galactic field. In order for amplification to work, a magnetic field of at least $10^{-6}\mu$G must have existed in the protogalaxy with a coherence length of about 1 kpc after the collapse. How exactly this could be achieved is still an open question, but the general scheme is that the "seed" fields of $10^{-13}\mu$G - $10^{-15}\mu$G are produced by means of the so called

Biermann battery [129] and then those are amplified by means of turbulent dynamo in the protogalaxy [130, 131]. It seems that more advanced theory will combine both approaches and extensive simulations [124].

5.2 Measurements of Galactic Magnetic Field. Different Techniques

5.2.1 Starlight Polarization

The first evidence of the existence of the galactic magnetic field appeared from starlight polarization measurements in the late 1940's when a large-scale field was discovered in the interstellar medium [132]. It turns out that starlight gets polarized when it passes through the areas of space filled with dust. The mechanism of how such polarization happens is explained qualitatively as follows.

Even though the dust adds up to just one percent of the interstellar matter, it is responsible for about 30% of the energy radiated by the Galaxy due to re-radiation of the absorbed ultraviolet light in the infrared and sub-millimeter ranges. The incoming light polarizes dust grains making them electrical dipoles responsible for the re-radiation where different processes contribute such as absorption, scattering and interference in the direction of light propagation. If a grain is not perfectly spherical then absorption for electric field is higher along the main axis of the grain, and hence the originally unpolarized incoming optical light becomes preferably polarized in the direction of the smallest dimension of the grain. On the other hand, according to the Kirchhoff law at thermal equilibrium, the emissivity of a body equals its absorptivity leading to sub-millimeter re-radiation being polarized along the main axis of the grain. This mechanism would not produce an overall polarization in the case of

a large cloud of randomly oriented dust grains, but it turns out that this situation changes if a coherent magnetic field is present in the same region of space.

Polarization maps of the non-thermal galactic radio background and of the Faraday rotation (to be discussed below) show that on average the galactic magnetic field lies in the plane of the Galaxy. This fact combined with the starlight polarization measurements, where one can also clearly see that the polarization planes are aligned with the galactic plane, allows one to conclude that on average the dust grains orientation is not random but rather aligned with the large scale coherent field. How this alignment happens could be explained under the assumption that the dust grains are rotating paramagnets [133]. Paramagnetic properties could be attributed to the presence of iron ions or hydrogen atoms both possessing non-zero magnetic moments, whereas the rotation of the particles could be initiated by escape of the hydrogen molecules from the grain surface in the case of even small, 0.1%, variation of its properties [134]. The axis of rotation tends to align itself with the magnetic field due to dissipation of rotational moment component perpendicular to the field when reversals of the grain magnetization happen in the course of rotation [127].

Thus starlight polarization measurements provide a nice tool to look at the magnetic field orientation. However, an ambiguity in sign remains.

5.2.2 Synchrotron Radiation

Synchrotron radiation, well known from the accelerator physics, is also produced in the Galaxy by relativistic (non-thermal) particles orbiting in the galactic magnetic field. The radiated power depends on the charge and the mass of a particle as q^2/m^2, and thus electrons make the main contribution. First observations of the cosmic synchrotron radiation were made in the early 1960's [135].

The intensity of the cosmic synchrotron radiation depends on the non-thermal

(cosmic ray) electron density n_{CR} and the strength of the magnetic field perpendicular to the line of sight. The cosmic ray electron spectrum follows a power law with spectral index s, and the synchrotron intensity at frequency ν is given by the integral along the line of sight:

$$S(\nu) = \sigma(\nu, s) \int_l n_{CR} B^{(s+1)/2} dl \tag{5.1}$$

where the emissivity $\sigma(\nu, s)$ $\nu^{-(s+3)/2}$ is a power law, from which it follows that the synchrotron intensity is a power law, too. The typical value of the cosmic ray spectral index is 3.

There are several ways one could make estimates of the magnetic field from the synchrotron radiation data [127]. Estimates of the field strength could be made from direct measurements of the product $B^{(s+1)/2} KL$ with L being the source dimension along the line of sight and K is a coefficient depending on n_{CR} in a particular energy range. Also, a field strength estimate could be made by assuming equipartition of energy between the relativistic motion of electrons and magnetic fields in the source region. Relativistic electrons absorb synchrotron radiation which was emitted deeper in a source, and that leads to a dip in the emission spectrum at low frequencies with the characteristic frequency being dependent on the magnetic field value and the angular size of the source, ν_0^{s+4} $B^{1/2} \alpha^{-2}$. Finally, synchrotron emission is linearly polarized with polarization degree defined as the ratio of intensities of the polarized and total emissions. The polarization degree depends on the presence of the random fields as well as on the effect of Faraday rotation (discussed later), and it leads to the fact that the polarization degree rarely exceeds 10 – 20 % in spiral galaxies.

Approximate methods described above may be usefully applied to some compact sources in particular directions, but the general structure of the field cannot be reliably derived from these simple arguments. Our position inside the galactic disk requires 3D modeling in order to determine the correct configuration of the field. In regards to

the synchrotron radiation surveys such modeling consists of trying different models of the GMF and cosmic ray density in order to get a synchrotron intensity map which corresponds to the measured data. Description of the modern synchrotron radiation surveys as well as several analysis papers based on them will be given in section 5.3

5.2.3 Rotation Measures

Most of our knowledge about the galactic magnetic fields comes from the measurements of Faraday rotation of linearly polarized light from pulsars and extragalactic radio sources. As opposed to the synchrotron radiation described above, Faraday rotation provides us with a measurement of the line-of-sight component of the field.

The plane of rotation of linearly polarized light rotates as it propagates through a magnetized medium. The angle by which the polarization plane is rotated with respect to its initial value is proportional to the square of the wavelength, and the coefficient of proportionality is called a rotation measure (RM).

$$\phi = \phi_0 + RM\lambda^2 \tag{5.2}$$

where the rotation measure (in radians per square meter), RM, for a pulsar at some distance D (in parsecs) is given by the following integral along the line-of-sight [136]:

$$RM = \frac{e^3}{2\pi m^2 c^4} \int_0^D n_e(s) B \ ds = 0.81 \int_0^D n_e(s) B \ ds \tag{5.3}$$

where the free electron density, n_e, is given in particles per cm^3, B is the line-of-sight component of the field in microgauss.

Pulsars are very well suited for the RM measurements since the distance to them can be estimated reasonably well, and as opposed to extragalactic radio sources they do not have an extended magnetic field, the effects of which are difficult to separate from the intrinsic Faraday's rotation due to the magnetic field of our Galaxy. Even

more appealing is the fact that n_e-weighted average value of the line-of-sight field (in microgauss) can be directly obtained from pulsar measurements as following,

$$\overline{B} = 1.232 \frac{RM}{DM} \tag{5.4}$$

where DM is the dispersion measure or the number of free electrons per unit area between us and the pulsar (in parsecs per cm^3) and is given by

$$DM = \int_0^D n_e(s)\, ds \tag{5.5}$$

In practice both rotation and dispersion measures are measured using some narrow bandwidth $\Delta\nu$ (in MHz) of frequencies over which a pulsar signal is detected. The dispersion leads to the time spread between detection of the beginning and the end of the wave-packet emitted by the pulsar. For a narrow MHz bandwidth and a GHz central frequency the time difference (in μs) becomes [137]

$$\Delta t = 8.3 \Delta\nu\, \nu^{-3}\, DM \tag{5.6}$$

and the dispersion measure is calculated from this equation. Similarly, the RM is calculated from a differential from of the equation (5.2), where $\Delta\phi$ corresponds to the measured change in the angle of polarization plane over the observed spread of the signal's frequencies:

$$\Delta\phi = 2c^2 \Delta\nu\, \nu^{-3}\, RM \tag{5.7}$$

To extract information about the field the following approach is used. The sky is divided into different regions so that lines of sight in those regions cross different galactic arms and interarm regions. By plotting rotation and dispersion measures for all pulsars in a given region, it is possible to estimate the field values from the slope of a linear fit. Also, random fields are responsible for the spread in the data points by which it is possible to estimate their magnitude as well.

An insufficient number of measurements and our position within the Galaxy have limited our ability to reconstruct a full three-dimensional configuration of the field using RMs. Nevertheless some local features of the field have been discovered. As in the case of the synchrotron radiation measurements, three-dimensional modeling is needed to infer predictions for RMs first and then compare them with observations. In this way it will be possible to deduce a full three-dimensional picture. Different models have been proposed and tested against RM data from different surveys and will be discussed in section 5.3.

5.3 Current Best Constraints on Galactic Magnetic Field

In this section I describe conclusions about the galactic magnetic field drawn from the astronomical techniques described above. A review of the most important and recent works devoted to this subject is conducted, and then the most promising models of the Galactic magnetic field are described. Different model parameters and ranges of their possible values will be considered. These models with different parameters will define the parameter space to test using propagation of UHECR detected by the Pierre Auger Observatory with a method which will be described in the next chapter.

Analysis of starlight polarization confirms that the galactic magnetic field predominantly lies in the plane of the Galaxy as concluded in the analysis of a large dataset containing nearly 7000 stars done by Heiles [138], the most comprehensive starlight polarization study to date. The dataset represents a compilation of many measurements for both northern and southern hemispheres done by Mathewson and Ford [139]. The huge advantage of this dataset was high repeatability of the measurements from different observers and use of a specifically designed telescope. Using

the least-square fit the local radius of curvature and pitch angle are found from the data. The pitch angle is an angle lying in the galactic plane and by which the field vector at a given point of space is different from the azimuthal unit vector of the cylindrical coordinates connected to the galactic center (see Figure 5.3). If the field vector points outside (inside), the circle defined by some radius ρ then the pitch angle is positive (negative). The results of Heiles are 8.8±1.8 kpc for the radius of curvature and -7.2°±4.1° for the pitch angle. The field lines correspond to spirals. Let us now look at what RMs have revealed so far about the galactic magnetic field.

Rotation measures have been systematically measured since the 1970's. RMs have helped to qualitatively understand many features of the GMF. For example the local direction of the field toward galactic longitude $l \sim 90°$ was inferred from RMs in several studies [140–142].

At this point, it is useful to give the reader a general idea about the spiral structure of the Milky Way. The modern theory of galaxy formation and, in particular, of spiral arms formation is still in the process of development. Spiral arms are believed to be formed as a consequence of interaction of slowly moving density waves and faster interstellar medium. In the 1960's it was shown that such density waves could be shaped into spirals and could form as a result of collective motion of the galactic medium [143, 144]. Collisions between slowly moving density waves and the rest of the galactic medium cause regions of high matter density where star formation happens at high rates. From this fact we can conclude that a precise mapping of such regions is a good tool to map spiral arms themselves. A recent compilation of measurements of star formation regions and corresponding positions of different arms is given in [145], and based on it, a visualization of spiral arms positions within the Galaxy is given in Figure 5.2. This depiction should be useful below to see where different field reversals happen.

A field reversal was identified near the Carina-Sagittarius arm [142, 146, 147]. In studies [148] and [149] it was shown that there is a clockwise field near the Crux-Scutum arm, and there are several reversals happening both inside and outside with respect to the solar system position. A counterclockwise field has been found near the Norma arm in the studies [150, 151]. All these conclusions only allow us to say that the GMF definitely has a pattern and it most probably follows the spiral arms.

Several other studies have been done recently, but give controversial results despite utilizing larger datasets. Han et al. [152] analyzed a large RM dataset of 223 pulsars and found evidence that the galactic field is counterclockwise in the inner arms of Norma, Crux-Scutum and Carina-Sagittarius, with reversals on the boundaries so that it is clockwise in the interarm regions. Such a picture of the field is consistent with bisymmetric models (the field reverses sign under 180° rotation in the plane of the Galaxy) and spiral structure. On the other hand, Vallée [153] has used 354 pulsars mostly from the Web site of the Australia Telescope National Facility (http://www.atnf.csiro.au/research/pulsar/psrcat/) and concluded that a circular clockwise magnetic field with a radial extent of up to 12 kpc gives the best fit to the data except for a 2 kpc wide counterclockwise field located between 4 and 6 kpc. Brown et al. consider yet a different dataset of 148 extragalactic radio sources all situated in the fourth galactic quadrant measured by the southern Galactic plane survey (SGPS). They come to the conclusion that the field is clockwise in the Carina-Sagittarius arm and counterclockwise in the Crux-Scutum arm. This result differs from the results of Han et al.

Synchrotron radiation data come from surveys made in the last 30 years and are usually used in conjunction with RM data with the aim of fitting both of them as well as possible with the same model of the GMF. Sun et al. [154] use three extragalactic source RM datasets to find the best fit regular magnetic field which is then used

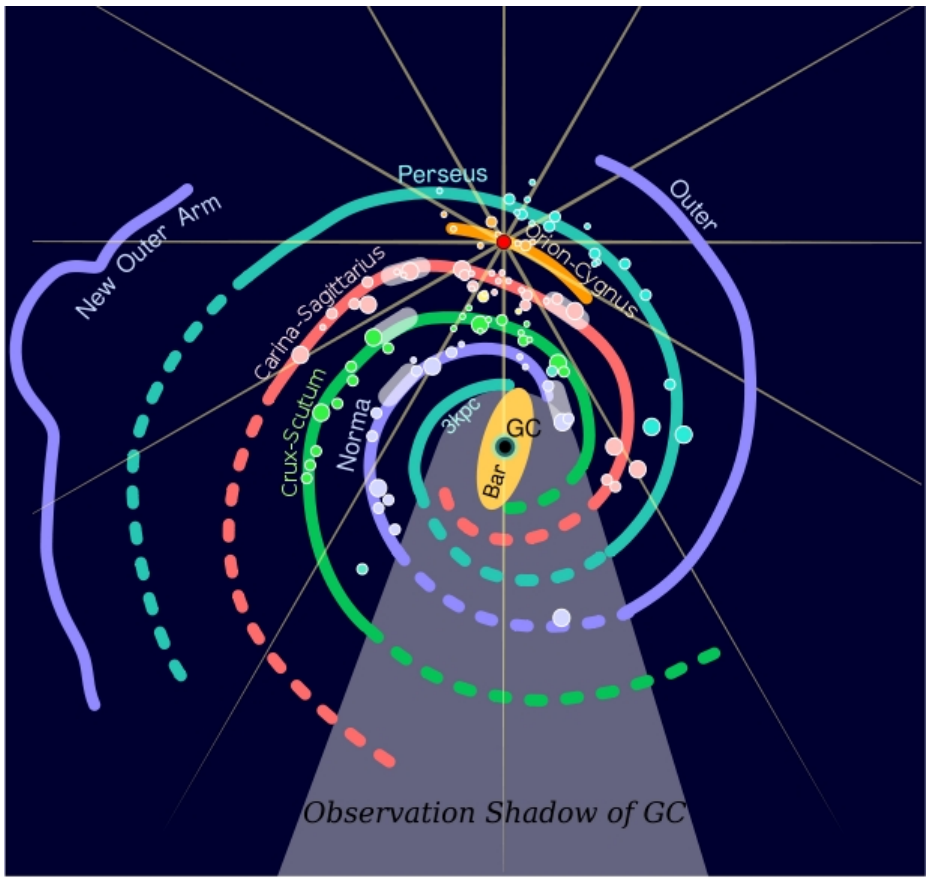

Figure 5.2 Schematic representation of the Milky Way spiral structure. The Sun position is represented by a red dot and yellow rays are the galactic longitude lines incrementing by 30° counterclockwise with respect to the Sun-GC line. The star formation regions are shown as circles of different color corresponding to the color a spiral arm they have been detected in. Based on [145]

with the synchrotron radiation data to constrain the random component of the field and the CR electron density. The first dataset is composed of extragalactic sources at high latitudes (Effelsberg survey), and the other two (CGPS and SGPS) contain sources close to the galactic plane. For the synchrotron data two surveys are used: WMAP 22.8 GHz polarized intensity map; and 408 MHz all-sky total intensity map. The results of the modeling by Sun et al. support an axisymmetric version of the GMF, mixed ring and spiral arm variant, whereas the bisymmetric version does not

fit the data well.

A very similar approach is used in a recent study by Jansson et al. [155]. Cosmic ray and thermal electron models along with different GMF models are fed to a computer code that produces simulated maps of the synchrotron radiation and RMs. The simulated and observed maps are compared using reduced χ^2 and the whole parameter space for each model is sampled using the Metropolis Markov Chain algorithm. In this way the authors test many models that were proposed in different studies including those described above. They conclude that none of the models fit the data well although there is useful information about the field symmetry with respect to the galactic plane - an antisymmetric distribution for the disk field is disfavored whereas, on the contrary, the halo field seems to be antisymmetric.

Polarized WMAP data have been analyzed standalone as well. Page et al. [156] use the 22 GHz K-band and modeled it by introducing a logarithmic spiral magnetic field model and a model for cosmic ray electrons. They compare the magnetic field angle between the model and observations with the help of the correlation coefficient $r = cos(2(\gamma_{model} - \gamma_{data}))$. They have found the model to be in agreement with the synchrotron radiation and a pitch angle of 35°, but as noted in several studies, such a large angle could be explained by influence of a local feature called a north polar spur produced by an expanding shell from a supernova. Another WMAP K-band study has been done by Miville-Deschênes et al. [157]. As opposed to Page et al., instead of the polarization angle they used the polarization fraction to fit the data with a bisymmetric spiral field model, a method that is insensitive to local structures. They obtained a pitch angle of -8.5° as the best fit value which is within the range of results from starlight polarization and RMs.

The review of different studies, given above, concentrates on the field in the galactic thin disk. Measurements of the distributions of stars as a function of distance

from the galactic plane [158] show that there exist two components of the star distribution: one, called the galactic thin disk, with a scale height of 300 pc within 1 kpc of the plane, and another one, the thick disk, with a scale height of 1.4 kpc present at the heights of 1-5 kpc of the plane. Surveys and studies (see [159–166]) of rotation measures from pulsars and extragalactic sources show an antisymmetric pattern at high galactic latitudes as analyzed and discussed in [150,167]. These facts suggest the existence of a large-scale field in the galactic thick disk. The antisymmetric pattern has been recently confirmed with a larger sample of 1800 RMs from Effelsberg survey as shown in [154] where the authors fit a three-dimensional model of a field consisting of two toroidal components (proposed by [168]) located above and below the disk but with opposite azimuthal field directions.

Besides the toroidal field, a dipole field has been suggested by some earlier studies with the vertical component of 0.2-0.3 μG in the solar vicinity [150, 161]. However, recent studies (see [169,170]) with larger samples of sources rule out the simple dipole solution. In [169] a vertical field of 0.30 ± 0.03 μG is derived for the southern galactic hemisphere and of 0.14 ± 0.02 μG in the northern hemisphere but both pointing towards each other. On the other hand in [170], a practically zero vertical field of 0.00 ± 0.02 μG is found at 3σ level towards the north galactic pole and of $0.31 \pm 0.03\mu$G at 9σ towards the south pole within a narrow cone of galactic latitudes, $b \geq 77^{\circ}$. Based on a better care of outliers and small region of averaging the latter study seems to have more credible results. Thus, the dipole field is not included into consideration later; only the toroidal field will be used as the halo component.

The most recent analysis of a large compilation of RMs has been done by Pshirkov et al. [171]. The analysis makes use of two datasets of RMs from extragalactic sources, NRAO VLA Sky Survey (NVSS) which includes data from 37,543 sources, but also

has a large blind spot for declinations below -40° and KNM11 (Kronberg and Newton-McGee 2011) compilation of 2257 sources described in [172]. The first catalog has an advantage of large statistics, but has a relatively large error compared to the second one especially in the region of the galactic plane, so by using two independent datasets authors could make crosschecks and cover the whole sky. The sky is divided in bins of equal area. The RMs are averaged in each bin and the size of a bin is small enough to allow enough variation in the coherent part of the GMF, yet it is big enough to smooth out all the source-to-source fluctuations. The values in each of the bins are compared with the predictions from different models of the GMF. The authors have used the maximum likelihood method, which gives the minimum χ^2 as well as all others that lie within 1σ from the best fit values. The results suggest that the GMF consists of two components: the disk field and the halo field. The anti-symmetric pattern of the RMs above and below the galactic plane is such that the disk field seems to be symmetric with respect to the plane whereas the anti-symmetry can be explained by the toroidal halo field which reverses sign in different hemispheres. The ring type of the disk field is strongly disfavored. The pitch angle varies in the limits from -3° to -7°.

5.4 Modern Galactic Magnetic Field Models

Let us now describe the models of the galactic magnetic field which are compatible with the observational studies described in the previous section. All of the models utilize a right-handed cylindrical coordinate system (ρ, θ, z) with the origin at the galactic center, as opposed to the galactic coordinate system which has the Sun's position as the origin. The corresponding rectangular coordinates (X ,Y ,Z) along with the galactic coordinates and their associated rectangular coordinates (X,Y,Z)

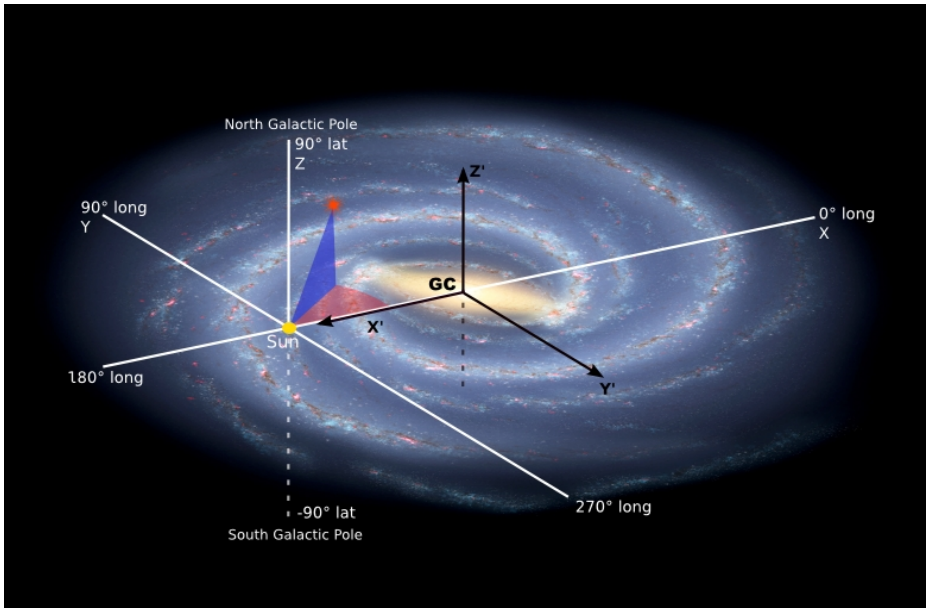

Figure 5.3 Galactic coordinate system and rectangular coordinates associated with the Galactic Center. Red arc spans galactic longitude and blue arc spans galactic latitude

are illustrated in Figure 5.3. (X ,Y ,Z) coordinates are also called galactocentrtic.

As described in the previous section, fields of spiral structure are favored by many RM data samples. Modern spiral field models are characterized by different variations of the logarithmic spiral with a constant pitch angle. The magnitude of the field in general can be expressed as follows

$$B(\rho, \theta, z) = B(\rho, \theta) f(z) = B(\rho) s(\rho, \theta) f(z) \tag{5.8}$$

where the radial and azimuthal dependence, "the spiral," are separated from the vertical dependence reflecting the fact that the Galaxy is a thin disk. A spiral field can be symmetric or antisymmetric under $\theta \quad \theta+\pi$ transformation. The field is called *bisymmetric* (BSS) if antisymmetric, and *axisymmetric* (ASS) if symmetric. The form of the $s(\rho, \theta)$, which describes the form of the spiral, depends on the symmetry. In the case of the BSS field, it is

$$s(\rho, \theta) = cos\left(\theta - \beta \ln \frac{\rho}{\rho_0}\right), \tag{5.9}$$

and for the ASS field, either the absolute value of the cosine is taken as in Stanev's model [173] and in [155], or it is squared as in the Harari-Mollerach-Roulet (HMR) model [174]. Parameters in (5.9) include β representing the amount of spiral winding and related to the pitch angle p as $\beta = 1/\tan(p)$, and ρ_0, which is the position of the field maximum along the galactic longitude line l=180° closest to the Sun. Following [173, 174] it is taken to be 10.55 kpc.

Stanev's model. In [173], Stanev introduced a spiral model where $B(\rho)$ and $f(z)$ have the following form

$$B(\rho) = \frac{3B_0\rho_\odot}{\rho} \text{ for } \rho \geq 4\text{kpc and constant } B(\rho = 4\text{kpc}) \text{ otherwise} \tag{5.10}$$

$$f(z) = \exp\left(-\frac{z}{z_0}\right). \tag{5.11}$$

where $z_0 = 1$kpc for $z \leq 0.5$ kpc and $z_0 = 4$ kpc for $z > 0.5$ kpc (for reference the thickness of the matter in the galactic disk is 0.5 kpc). B_0 is the field normalization value taken in the Solar system vicinity and $\rho_\odot$ is the distance from the Sun to the Galactic center, taken to be 8.5 kpc.

HMR model. Stanev's model has many non-differentiable points where different patches of the field come together, so it was revisited by Harari, Mollerach and Roulet in [174] where all those points are patched with smooth functions so that $B(\rho)$ and $f(z)$ become

$$B(\rho) = \frac{3B_0\rho_\odot}{\rho}\tanh^3\left(\frac{\rho}{\rho_1}\right), \tag{5.12}$$

$$f(z) = \frac{1}{2\cosh(z/z_1)} + \frac{1}{2\cosh(z/z_2)}. \tag{5.13}$$

where $\rho_1 = 2$ kpc and z_1 and z_2 are the scale heights. $z_1 = 0.3$ kpc which corresponds to 0.5 kpc in the Stanev's model.

As follows from the dynamo theory [125, 127] pure spiral solutions can have different symmetry with respect to the galactic plane. The even (symmetric) solution,

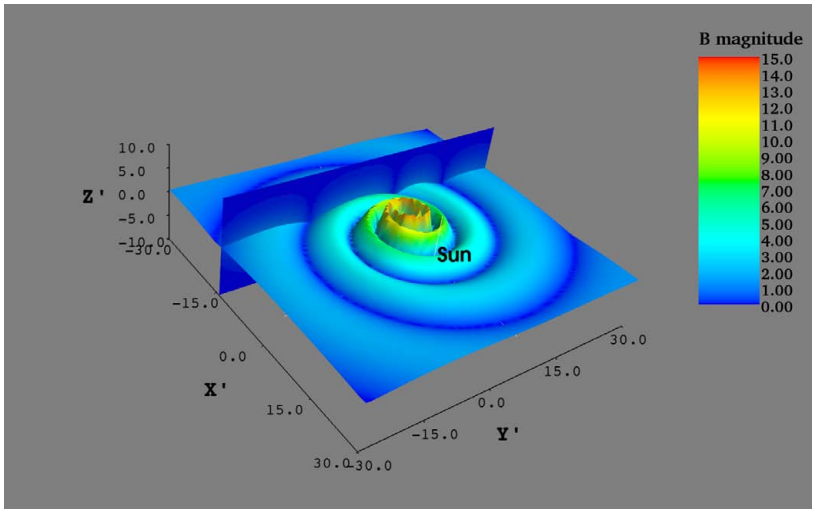

Figure 5.4 HMR BSS_S field model. The parameters used are as follows: B_0 = 3 μG, p = -11°, z_2 = 2 kpc. Two planes show the magnitude profile of the field in μG in the galactic plane and across it. The position of the solar system, which lies in the galactic plane, is labeled directly above. The coordinates are the same as in Figure 5.3

denoted as "_S," corresponds to the field that does not change sign above and below the plane, whereas the odd (antisymmetric) solution, denoted as "_A," represents the field that reverses direction when crossing the galactic plane. This fact is taken into account by introducing an additional $\tanh(z/z_3)$ factor for the antisymmetric case with the z_3 = 20 pc. Therefore there are four possibilities: ASS_A, ASS_S, BSS_A and BSS_S. Figure 5.4 shows an example of the HMR BSS_S field. One can see the spiral structure of the field and its increase towards the Galactic center. The profile plane perpendicular to the galactic plane shows how the field decays according to (5.13).

Besides radial dependences, $B(\rho)$, used in the models above, Han et al. [152] and Sun et al. [154] used the following exponential form which is consistent with the RM data:

$$B(\rho) = B_0 \exp\left(-\frac{\rho - \rho_\odot}{\rho_\odot}\right) \tag{5.14}$$

The cylindrical components of the spiral fields above are expressed as follows

$$\begin{aligned} B_\rho &= B(\rho, \theta, z)\sin(p) \\ B_\theta &= B(\rho, \theta, z)\cos(p) \\ B_z &= 0 \end{aligned} \tag{5.15}$$

The vertical component of the field is absent in the pure spiral models but can be added as a part of a dipole halo field.

Sun+RING model. Sun et al. [154] find a good fit between axisymmetric spiral models and the RMs both for high latitude sources and galactic pulsars. They add some reversals inside the solar circle in the form of several rings. They use the same exponential type of radial dependence as in (5.14) and also vertical dependence, $f(z)$. For the vicinity of the galactic center the model follows Stanev's model and has the field magnitude constant within some radial distance ρ_c from the center. The field does not depend on θ so it is azimuthally symmetric.

$$B(\rho, z) = \begin{cases} B_0 \exp\left(-\frac{\rho-\rho_\odot}{\rho_0} - \frac{z}{z_0}\right) f_{ring}(\rho) & \text{if } \rho > \rho_c \\ B_0 \exp\left(-\frac{z}{z_0}\right) f_{ring}(\rho) & \text{if } \rho \leq \rho_c \end{cases} \tag{5.16}$$

where $\rho_c = 5$ kpc, $\rho_0 = 10$ kpc following [154] and $f_{ring}(\rho)$ factor adds three rings by simply switching the direction of the field within different annuli as following:

$$f_{ring}(\rho) = \begin{cases} +1 & \text{if } \rho > 7.5 \text{ kpc} \\ -1 & \text{if } 6 \text{ kpc} < \rho \leq 7.5 \text{ kpc} \\ +1 & \text{if } 5 \text{ kpc} < \rho \leq 6 \text{ kpc} \\ -1 & \text{if } \rho \leq 5 \text{ kpc} \end{cases} \tag{5.17}$$

Once the magnitude of the field is set by the equations above, the components are given by the same equations as in (5.15). An example of this type of field is shown in Figure 5.5

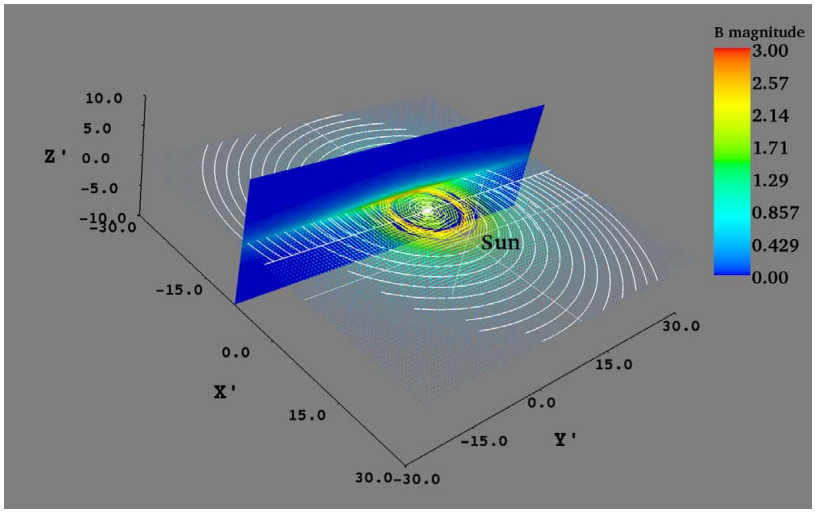

Figure 5.5 Sun+RING model by [154]. The parameters are taken from the paper: $B_0 = 2$ μG, p = -12°, $z_0 = 1$ kpc, $\rho_c = 5$ kpc. White lines represent the field lines. The position of the solar system is labeled and shown by a white cross. The coordinates are the same as in Figure 5.3

Vallée's model. Let us finally consider a pure ring field model proposed by Vallée in [153]. The model is composed of nine circular rings of clockwise field direction (looking from the North Galactic pole) except for one field reversal in one of the rings. The summary of the field is given in Table 5.1, which has been slightly modified from the original table given in [153]. Two parameters are added to vary: firstly, a dimensionless scaling factor, s, which allows varying the overall normalization of the field in the limits between 1 and 6 μG at the Solar system location and, secondly, the vertical attenuation factor, z_0, in a simple form of $\exp(-\ z\ /z_0)$. Figure 5.6 shows Vallée's model.

Toroidal halo. This concludes the description of the regular disk field models. Let us now describe the toroidal field which is a field located above and below the galactic disk and could be added to any of the disk models. In particularly, it was added by Sun et al. to the models described above. The analytical form of the field is given

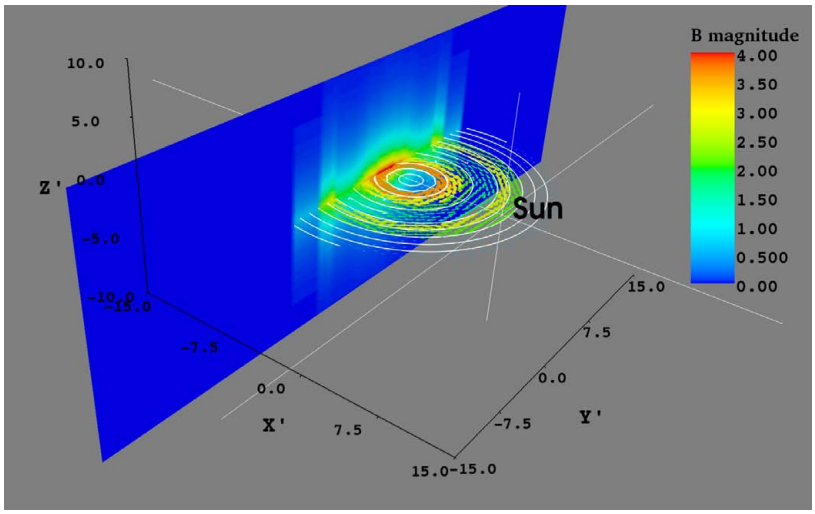

Figure 5.6 Vallée's model from [153]. The vertical attenuation scale $z_0 = 2$ kpc. White lines represent the field lines. The position of the solar system is labeled and shown by a white cross. The coordinates are the same as in Figure 5.3

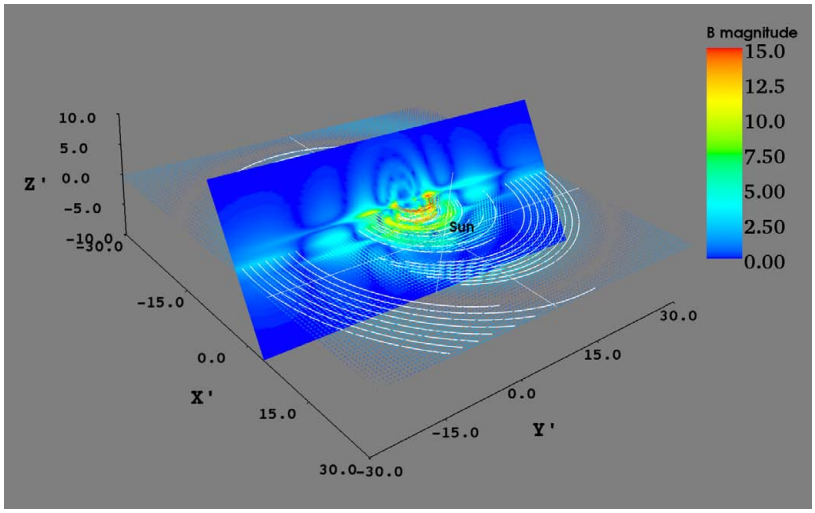

Figure 5.7 HMR BSS_S + toroidal halo. The profile plane is set at an angle of 45° with the respect to the z-axis for better perspective of the field magnitude profile. The parameters for the disk component are the same as in Figure 5.4. The constants for the halo field are $B_0^H = 10$ μG, $z_0^H = 1.5$ kpc and $\rho_0^H = 4$ kpc. The position of the solar system is labeled and shown by a white cross. The coordinates are the same as in Figure 5.3

Table 5.1 Vallée's ring model

Radial distance (kpc)	B (μG)	Field direction
0 – 2	0.9	clockwise
2 – 3	3.8	clockwise
3 – 4	3.1	clockwise
4 – 5	2.2	anticlockwise
5 – 6	1.9	anticlockwise
6 – 7	1.9	clockwise
7 – 8	2.5	clockwise
8 – 9	2.2	clockwise
9 – 12	0.6	clockwise

in [168] and [154]. The field is purely azimuthal and is expressed as follows

$$B_\theta^H(\rho, z) = B_0^H \frac{1}{1 + \left(\frac{z - z_0^H}{z_1^H}\right)} \frac{\rho}{\rho_0^H} \exp\left(-\frac{\rho - \rho_0^H}{\rho_0^H}\right), \tag{5.18}$$

where $z_0^H = 1.5$ kpc, $z_1^H = 0.2$ kpc for $z < z_0^H$ and otherwise $z_1^H = 0.4$ kpc, and $B_0^H = 10$ μG, $\rho_0^H = 4$ kpc. Figure 5.7 shows the combined halo and disk components. One can see the toroidal structure above the main spiral disk field with the maximum strength at 1.5 kpc above the Galactic plane. The direction of the toroidal field is counter-clockwise if looking from above in the northern galactic hemisphere and clockwise in the southern. Since the spiral field has a vertical decay scale of 2 kpc according to (5.13), the disk and halo fields get mixed in this composed model so that there is no pure toroidal structure.

All the field models described above with the exception of Stanev's model (since the HMR model is essentially the same but differentiable, which is better) will be used in the analysis described in the next chapter. Also, as found in [154, 171], the fits between the GMF models and synchrotron data and RM data improve if the disk field is combined with the toroidal halo field. Therefore I test different combinations

Table 5.2 Summary of the GMF model parameters and their ranges. (Please note that the computation time limits do not allow for ranges of values in all models). The bin size is 1 unit for each parameter except for the scaling factor of the Vallée model, for which it is taken as 0.5

Model name	Parameter	Range of values
HMR	Normalization, B_0	1..6 μG
	Pitch angle, p	-7°..-11°
	Scale height, z_2	1..5 kpc
	Model symmetry	ASS_A, ASS_S, BSS_A, BSS_S
Sun+RING	Normalization, B_0	1..3 μG
	ρ_c	4..6 kpc
	ρ_0	8..15 kpc
	Pitch angle, p	-12°
	Scale height, z_0	1 kpc
Vallée	Scaling factor, s	0.5..3
	Scale height, z_0	1..5 kpc
Toroidal field	Halo strength, B_0^H	4 μG
	Radial extent, ρ_0^H	6 kpc
	Off-plane distance, z_0^H	2 kpc

of the disk and halo field as well. Every model will be scanned over its parameter space. Based on the results that have been found in the latest study [171], I set the limits on the parameters for the toroidal field and the field by Sun et al. in order to compare the results and see if the method below can further constrain the model candidates. All the models and their corresponding parameter spaces are summarized in Table 5.2.

Chapter 6

Constraints on Galactic Magnetic Field Models With Two-point Cumulative Autocorrelation Function

The previous chapter described how the galactic magnetic field forms and current best galactic magnetic field models based on astronomical observations. In this final chapter, I describe the interconnection between UHECR propagation and cosmic magnetic fields. The well known autocorrelation function (see [175–177]) method is described in the case of no field. It is used to search for generic anisotropies in the data independently from any source catalog. Based on the autocorrelation function, I perform an analysis on a Pierre Auger Observatory dataset to search for galactic magnetic field models which favor or disfavor clustering of UHECR arrival directions as they arrive to our Galaxy from extragalactic sources.

6.1 Clustering on Extragalactic Sky from Extragalactic Sources

The influence of the cosmic magnetic fields on the propagation of UHECR, if they are assumed to be charged particles, means that it is impossible to study one without the other. The Lorentz force acts on a charged particle as it propagates through space, and the information about cosmic magnetic fields becomes encoded in the amount of deflection experienced by the particle. On the other hand, the source positions of the UHECR are not known, and their apparent locations on the sky are expected to be different from how they would be seen by an observer outside the Galaxy due to magnetic deflections.

Recent results from the Pierre Auger Observatory [46,48,98,178], namely evidence for the GZK cutoff in the energy spectrum and correlation of arrival directions with the extragalactic matter distribution, suggest an extragalactic origin of UHECR. In general, there are three contributions to magnetic deflections preventing seeing a source of UHECRs: deflections due to intrinsic magnetic fields at the source site itself, deflections in the extragalactic[1] magnetic field (EGMF), and deflections in the GMF. Additionally, there is an angular uncertainty of a detector, but it is quite small compared to other deflections being, as mentioned above, 0.6° in the case of the Pierre Auger Observatory. Given cosmological distances of tens and hundreds of megaparsecs to possible sources, possible intrinsic deflections are included in the source definition so that we are left to deal with the effect of the EGMF and GMF.

The results in Section 1.4 are based on the consideration of propagation of protons

[1]The word "extragalactic" here refers to the fact that the field is considered outside the disk and halo matter of a galaxy. In many papers, a word "intergalactic" is used referring to the space in between galaxies.

along straight lines neglecting the effects of extragalactic magnetic fields. The EGMF is still poorly known. The structure of the EGMF is complex and probably correlates with the large scale structure of the Universe. This view was intensively explored in numerical simulations by Ryu [179, 180]. According to the simulations, the EGMF consists of relatively strong fields inside galaxy clusters on the order of 1 μG with the field around them of 0.1 μG, and those clusters are connected by filaments of a weaker field of about 10 nG which is nevertheless significant in terms of the influence on the UHECR propagation. The remainder of space consists of voids where the magnitude of the field is very low, less than 10^{-12}G, making it irrelevant for propagation of UHECR. If this picture was real then UHECR propagation would be impossible to treat in a statistical way and the observed flux as well as arrival directions would strongly depend on the exact details of the local EGMF structure within the GZK sphere for those UHECR that happen to be contained inside clusters of galaxies and filaments. Also, one can imagine those UHECR which travel through the regions of voids meaning that their propagation would not be affected at all.

On the other hand, the opposite scenario is that the EGMF forms a more irregular pattern so that the EGMF consists of patches of randomly oriented uniform fields. The coherence length of the fields is taken to be the average distance between galaxies which is 1 Mpc. Measured fields in the Coma and Virgo clusters could be used for normalization, and the field distribution is smoothed to fill the voids. In this case, the magnitude varies gradually from 0.1 – 1μ G inside galaxy clusters, to 10^{-9} – 10^{-8} G inside filaments, to 10^{-10} G in the voids [181]. In this case UHECR initial directions get smeared by random walk with an rms angle of

$$\alpha_{rms} = 0.35^{\circ}\frac{ZB_{-9}}{E_{20}}\sqrt{Dl_{coh}} \tag{6.1}$$

where the magnetic field B_{-9} is in nG, energy E is in units of 100 EeV, and distance

D is in Mpc as well as the coherence length l_{coh}. A strict derivation of (6.1) is given in [182].

In this work, I assume that the EGMF are described by this latter scenario. Therefore, a source from within the GZK sphere is expected to be smeared from being a point source to a blob of some angular size as it would be seen on the extragalactic sky. By extragalactic sky I mean a sphere in galactocentric coordinates introduced in 5.4. The diameter of the sphere is such that the galactic magnetic field does not influence UHECR propagation outside the sphere. In practice, it is set at 20 kpc. For example, an angular size of a proton source 100 Mpc away is then estimated to be 5 degrees for an energy cut of 50 EeV using (6.1).

An observatory located at Earth detects deflected cosmic rays after they have propagated through the GMF. The magnitude of the galactic field is big enough so that arrival directions from a single source as we observe them on the Earth's sky could be focused or de-focused. By backtracking the cosmic rays detected by the Pierre Auger Observatory through different magnetic field models, one can find a subset of models that produce statistically significant clustering on the extragalactic sky. The main idea of this study then is to find out if there is significant clustering of the arrival directions as they would be seen not from the Earth's sky but on the extragalactic sky, and to constrain the GMF if such clusters exist and deviate from what one would expect from an isotropic distribution. Thus, constraints are set on the parameter space of a particular model in the sense that only some part of the parameter space might be found compatible with the hypothesis of extragalactic origin of UHECR, random EGMF with nanogauss magnitude, and 1Mpc coherence length. The analysis is done assuming pure proton composition. Also, an implicit assumption is that the distribution of sources of the UHECRs is anisotropic within the GZK sphere otherwise it would make no sense to compare with an isotropic

distribution.

If there are no significant clusters found one can at least confirm which GMF models are completely compatible with isotropy even in the pure proton scenario and also check them for heavier composition up to pure iron composition, in which case the deflections are expected to be so large that backtracking should not be able to reveal any sources due to random deflection. Of course, it would be interesting if significant sources are found, meaning that if the random component does not exceed some limit then they are real extragalactic sources.

The next section describes what statistical measure or metric is used to characterize clustering and therefore constitutes a criterion used to constrain the GMF.

6.2 Autocorrelation as Measure of Clustering

One of the main results of the reconstruction of the data collected by the Pierre Auger Observatory is a sky map of UHECR arrival directions along with their energies. A standard statistical method to search for anisotropies in such data was borrowed by astrophysicists from astronomers where it was used to study the distribution of galaxies (see, for example, [175]). It is called autocorrelation function statistics. In this work I make use of a two-point cumulative autocorrelation function.

Being applied to the Pierre Auger Observatory highest energy events plotted on the sky, the two-point cumulative autocorrelation function expresses the total number of pairs of arrival directions of UHECR above some energy cut at some angular separation from each other, α, otherwise called "angular window," on the sphere representing the sky in galactic or equatorial coordinates. An example is given in Figure 6.1 where one can easily count 3 pairs of arrival directions within a 9 degree angular window. A rigorous definition for the two-point cumulative autocorrelation

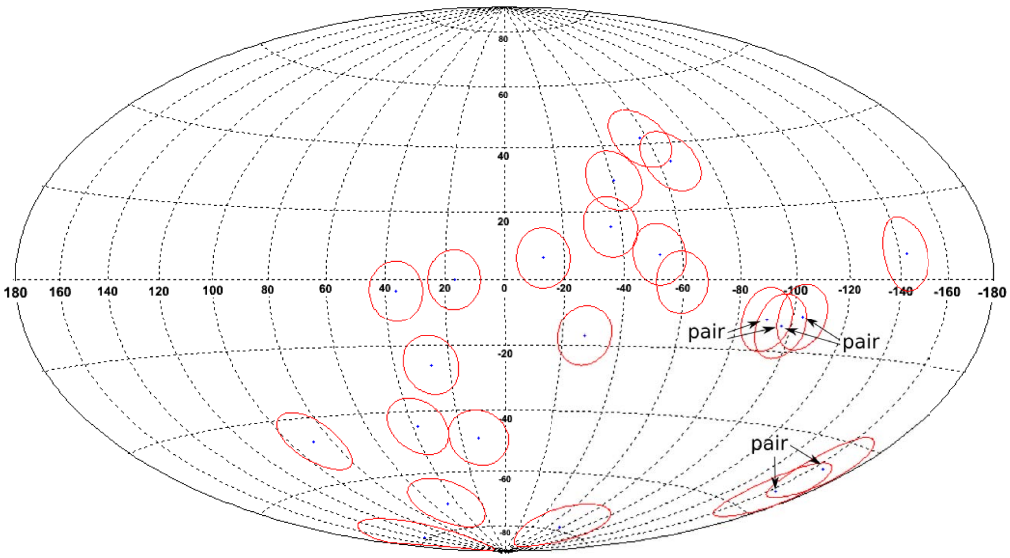

Figure 6.1 Example of UHECR arrival directions with 9 degree angular windows drawn around them. There are 3 pairs within the specified angular distance. Aitoff projection of the galactic coordinates

function is the following:

$$n_{pairs}(\alpha) = \sum_{i=2}^{N} \sum_{j=1}^{i-1} \Theta(\alpha - \alpha_{ij}), \tag{6.2}$$

where N is the total number of events, α_{ij} is the angular distance between events i and j on the sky, Θ is Heaviside step function, and the limits are such to avoid double counting.

The two-point autocorrelation function gives a measure of how tightly events are clustered on the sky. The higher the number of pairs, the higher the amount of clustering, providing evidence that there are cosmic ray sources on the sky with the characteristic angular scale of α. The statistical significance for the number of pairs is calculated based on comparison with the large number of "toy" Monte Carlo (MC) simulations wherein for each simulation, a set of arrival directions is simulated with randomized isotropic arrival directions weighted by the acceptance function of an observatory. If the source angular scale and the energy cut were well known then

the significance would be represented by the fraction of the MC simulations which produced the same or greater value of the autocorrelation function (6.2). This fraction is called an autocorrelation signal, and that is how it will be referred to in the text.

The matter of how to calculate the statistical significance in a proper way is not trivial. For example, the statistical significance of doublets and a triplet of the highest energy events observed by AGASA was based on the autocorrelation function (6.2), where α was taken to be 2.5° degrees based on the angular resolution of the detector [176, 183]. However, we cannot set a strict a priori limit on the angular scale since we don't know the angular size of unknown sources unless we make an implicit assumption that they are point sources. Also, there is a problem of setting the energy cut so that only events with the energy above it are included in the analysis. Finley and Westerhoff in [177] reanalyze the dataset of AGASA employing more elaborate analysis. They performed a scan in the parameter space of angular windows and energy cuts so that for each angular window taken within some broad range, an energy cut is made on the dataset and then the autocorrelation signal is calculated. In practice, the energy cut is done by sorting all the events in the dataset according to the energies in descending order. Doing it this way is independent from the absolute energy scale since only the order of the events is important. The results of such a scan can be represented by a two-dimensional profile plot with the number of events or, alternatively, value of the energy cut on one axis and angular window on the other axis.

Let us consider a scan done with the real data and discuss some of the issues related to the energy resolution and statistical significance of the results. For the previous such analysis, see [184]. The scan in Figure 6.2a represents the data from the 1st of January 2004 up to 15th of April 2011 above 30 EeV. It shows several regions where the autocorrelation signal is less that 10^{-1}. There is a global minimum at 109 events

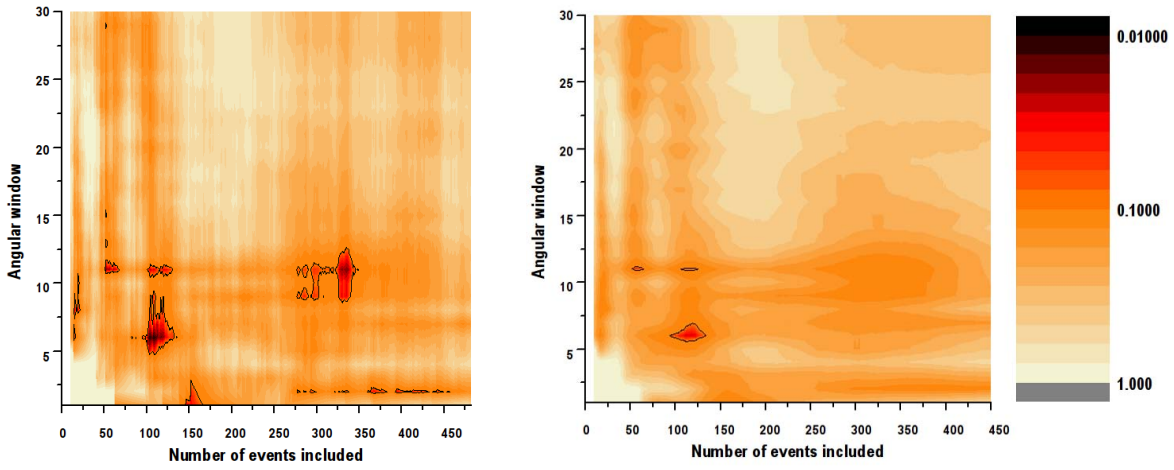

(a) Real data **(b)** After energy smearing

Figure 6.2 Two-point autocorrelation scan of the Pierre Auger Observatory data above 30 EeV collected from January 1, 2004 up to April 15, 2011 (left) and its average (right) for 100 simulations with each event energy smeared according to its energy resolution. The scan in energy starts from the top 10 events. The number of events starting from the top of the list corresponds to the energy cut: 15 events - 80 EeV, 32 events - 70 EeV, 64 events - 60 EeV, 121 events - 50 EeV, 227 events - 40 EeV.

and 6° with the autocorrelation signal of 0.012 meaning that only 1.2% of random arrival directions would give the same number or more pairs. The absolute number of pairs corresponding to the minimum is 39. The standard Auger reconstruction called the "Herald" is used for the analysis here and below: the zenith angle is less than 60° and the energy is calculated based on the constant intensity cut and latest FD calibration.

A question arises of how stable the results are with respect to the energy resolution of the detector. In order to answer it, I perform 100 scans absolutely identical to the scan with the real dataset, but with the only difference being that now the input datasets contain events with their energies randomly picked from a gaussian distribution with the mean corresponding to the measured energy for each event and

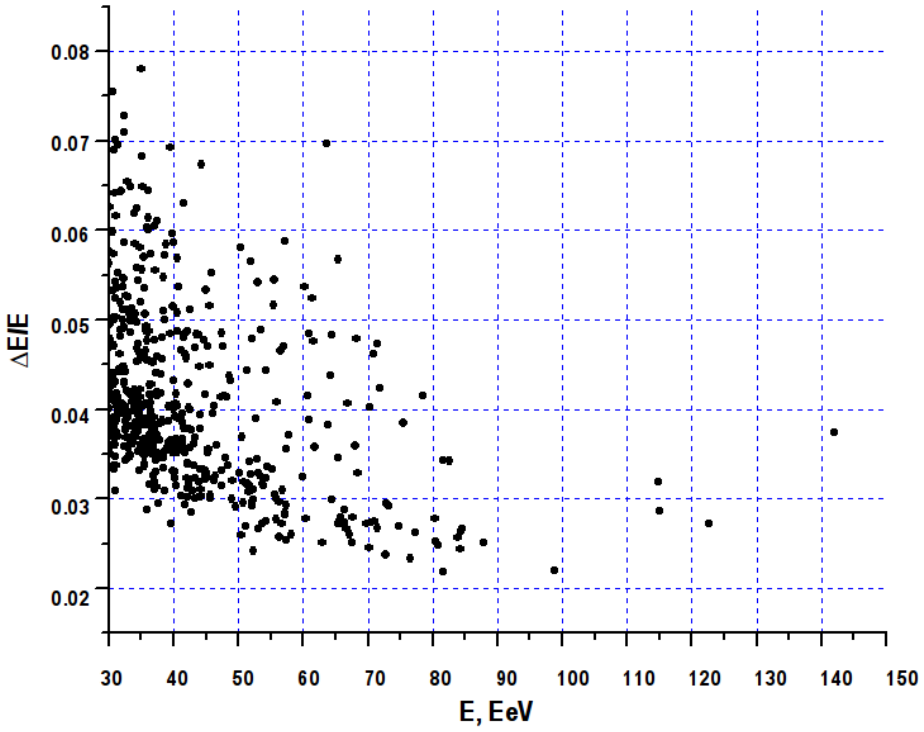

Figure 6.3 Individual relative uncertainty of the Herald reconstruction above 30 EeV

the standard deviation being equal to the individual uncertainty for that event. Figure 6.3 shows relative individual uncertainty, $\Delta E/E$, for events above 30 EeV. The uncertainty is calculated through the error propagation in the equations for energy calculation in the Herald reconstruction.

Each dataset is sorted in energy and therefore the only difference from the original dataset is that some events in the list get switched and the overall order changes. The average of 100 scans is shown on Figure 6.2b where for each point of the profile plot an average of 100 scan is taken. As can be seen the general structure is simimar to the scan with the real data. The global minimum stays approximately at the same position although the value of the autocorrelation signal gets reduced

to 0.059 or 6% chance of coming from isotropic distribution. The other minima get smeared away. The global minimum under consideration has been always present in the Auger dataset at the highest energies, however its value has been reduced by 2 orders of magnitude in the last years [48,98] due to detection of more and more events distributed in a more isotropic manner.

6.3 Backtracking of Charged Particles. CRT code for Backtracking.

I use a cosmic ray tracking code, called CRT, capable of both backtracking and forward tracking of charged particles through any user-defined model of the galactic magnetic field. The description of the code could be found in [185, 186]. The code is based on the numerical integration of the Lorentz force equation. The integration is done via the 5th order Runge-Kutta method [187].

The most useful feature of the code is its relative simplicity in terms of adding user-defined models of the GMF. The description of the models will be given in the next section. To verify that the models are implemented in the code without mistakes a modification was made to the "getfield" routine so that it produces an output file in the data format of the Visualization Toolkit (VTK) [188] which is then visualized in three-dimensions by use of data the visualization tool called Mayavi [189]. The three-dimensional visualization exposes the vector field of a particular model, as well as their magnitude, and their components in any plane and from any point of view outside the Galaxy. This three dimensional visualization is also very useful for investigating the results of the autocorrelation analysis later. Figure 6.4 shows an example of backtracking of the UHECRs starting from a detector located in the Solar system and until their trajectories leave the GMF. The illustration shows trajectories for

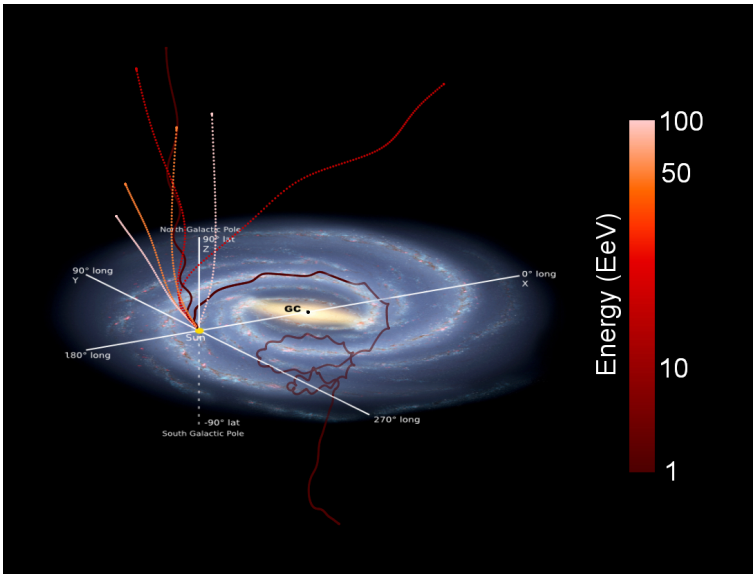

Figure 6.4 An example of backtracking for protons of different energies: 1, 10, 50 and 50 EeV. The galaxy is represented schematically. The trajectories are calculated with the CRT code. The GMF model used in this example is HMR BSS_S with $B_0 = 3$ μG, $p =$ -11°, $z_2 = 2$ kpc, and a toroidal halo field has been added as well with $B_0^H = 10$ μG, $z_0^H = 1.5$ kpc and $\rho_0^H = 4$ kpc (the description and plots of the models are given in Section 5.4)

eight protons with energies of 1, 10, 50 and 100 EeV. For each energy, two different initial arrival directions are taken: (90°, 0) and (0, 90°) in galactic coordinates. As one can see, the lowest energy protons are deflected the most, especially the one that arrives in the galactic plane after traveling along the spiral arm all the way from the region of the south galactic pole. The deflections above 50 EeV are less, which is important for the success of the method described below since otherwise the random component of the GMF would have led to complete scrambling of arrival directions and the backtracking approach would be useless.

6.4 Autocorrelation Analysis on Extragalactic Sky

The autocorrelation scan considered in the section 6.2 contains a global minimum at 51.3 EeV and 6°, and it is the only minimum which does not disappear even when the energy resolution is taken into account. Computational time restrictions make it impossible to perform autocorrelation scans for each point of the multidimensional parameter space of the magnetic field models. Therefore, we have to choose our cuts a priori, and it is reasonable to make the cut at 51 EeV and an angular window of 6° for the following autocorrelation analysis with the GMF included.

The main goal is to find the magnetic field model, if any, which favors clustering on the extragalactic sky. It means that such a field has to de-focus UHECR as they propagate toward the Earth or, on the other hand, to focus them in the case of backtracking. I will use the word "focusing" below in relation to models that favor clustering on the extragalactic sky since I use backtracking and not forward-tracking. As a measure of the focusing properties of a field I simply use a ratio between the number of pairs of arrival directions on the Earth's sky and on the extragalactic sky after backtracking. The ratio is calculated for each point in the parameter space for the same energy and within the same angular window chosen as described above. For the HMR BSS_S(A) and ASS_S(A) models, there are 150 points in the parameter space to scan over. The scanning has been done in one unit steps for the field normalization, pitch angle and vertical field scale in the limits defined in the Table 5.2. It is rather hard to visualize the results in three dimensions and analyze them. I use the VTK [188] visualization framework along with the convenient graphical interface called Mayavi2 [189] which allows any type of cuts and three dimensional rotations to easily see the whole parameter space with each point corresponding to a different configuration of the magnetic field. In order to achieve

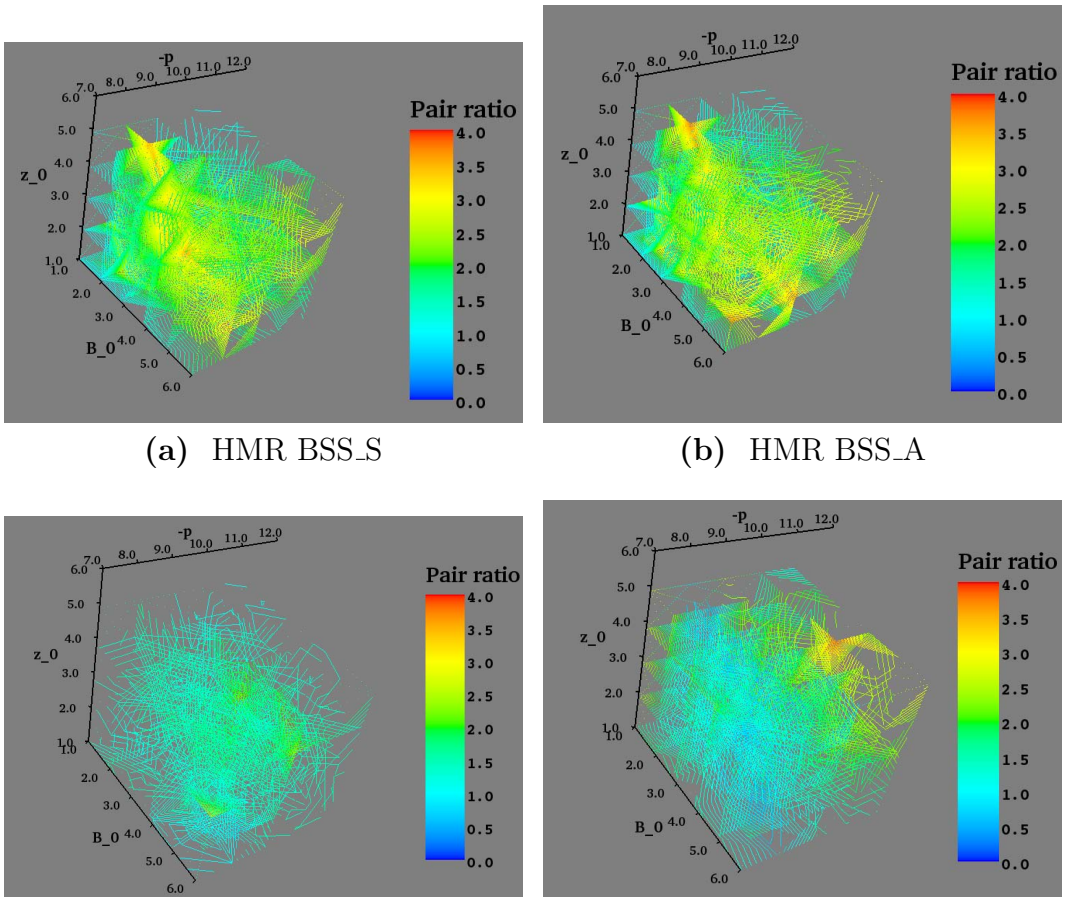

(a) HMR BSS_S **(b)** HMR BSS_A

(c) HMR ASS_S **(d)** HMR ASS_A

Figure 6.5 Ratios of the number of pairs within a 6° degree angular separation in the parameter spaces of the models HMR BSS_S(A), HMR ASS_S(A) before and after backtracking for the measured Auger data arrival directions above 51.3 EeV. The units and names of the axes could be found in the Table 5.2.

better visualization, a Delaunay triangulation filter is applied on the data which does not change the values but allows for plotting contours in between points.

Figure 6.5 shows the three-dimensional plots with the ratios calculated for the angular window of 6° and the energy cut of 51.3 EeV. The scale on all of the plots is the same and goes up to 4.0 since the ratio does not exceed 4.0 for any model. Figure A.1 shows the comparison between all four different models under consideration. One

can see that in general all models show some focusing for most points of the parameter space since only 65 points out 600 have the ratio less than 1.0. ASS_S(A) models rarely exceed the values of 2.0 whereas BSS_S(A) models have 17 points of the parameter space with a ratio above 3.0, so in general BSS type of models, where the field flips its direction under $\theta \quad \theta + \pi$, reveal more focusing in comparison. A closer look at the parameter spaces for each model reveals that the focusing in the BSS model mainly happens along the pitch angle plane of -8° where the ratio for many points becomes above 3.0. The maximum of 3.5 at (B_0,p,z_0)=(4 μG,-8°,3 kpc) occurs for BSS_S (_S meaning that the field is even with respect to the galactic plane), and the maximum for BSS_A (_A meaning that the field is odd with respect to the galactic plane) is 3.75 at (6 μG,-7°,2 kpc), whereas most of the other large ratio numbers above 3.0 lie in the -8° plane as well.

The ratio of the number of pairs indicates the relative focusing properties of the fields, but the next step is to determine the significance of the focusing. The autocorrelation function described in the previous section is a measure of such significance. Now we apply it not on the Earth's sky but on the extragalactic sky. The procedure is the following: first the real dataset of events is backtracked through a given field model and then a large number, taken to be 10^5, of datasets with isotropic distribution weighted by experiment's exposure, is backtracked through the same field model with the same parameters. This procedure of backtracking the real data and 10^5 isotropic MC data sets is repeated at each of the points in the parameter space for a given field model, and the autocorrelation signal is calculated at each point in the model parameter space.

Figure 6.6 shows the autocorrelation signal for the backtracked arrival directions within a 6° degree angular separation and above 51.3 EeV. It is calculated for all points in the parameter space of the four models considered above. As one can see

the differences between the significance of the autocorrelation signal are striking on the different plots. Only the plot for the HMR BSS_S model exhibits the same structure in the autocorrelation signal as it does above in the pair ratio. This structure follows the plane in a parameter space corresponding to a pitch angle of -8°. The minimum of the autocorrelation signal is 0.0009 whereas the corresponding minimum at the Earth's sky is 0.012. The minimum is at (5 μG,-7°,4 kpc), whereas the maximum of the pair ratio is at (4 μG,-8°,3 kpc).

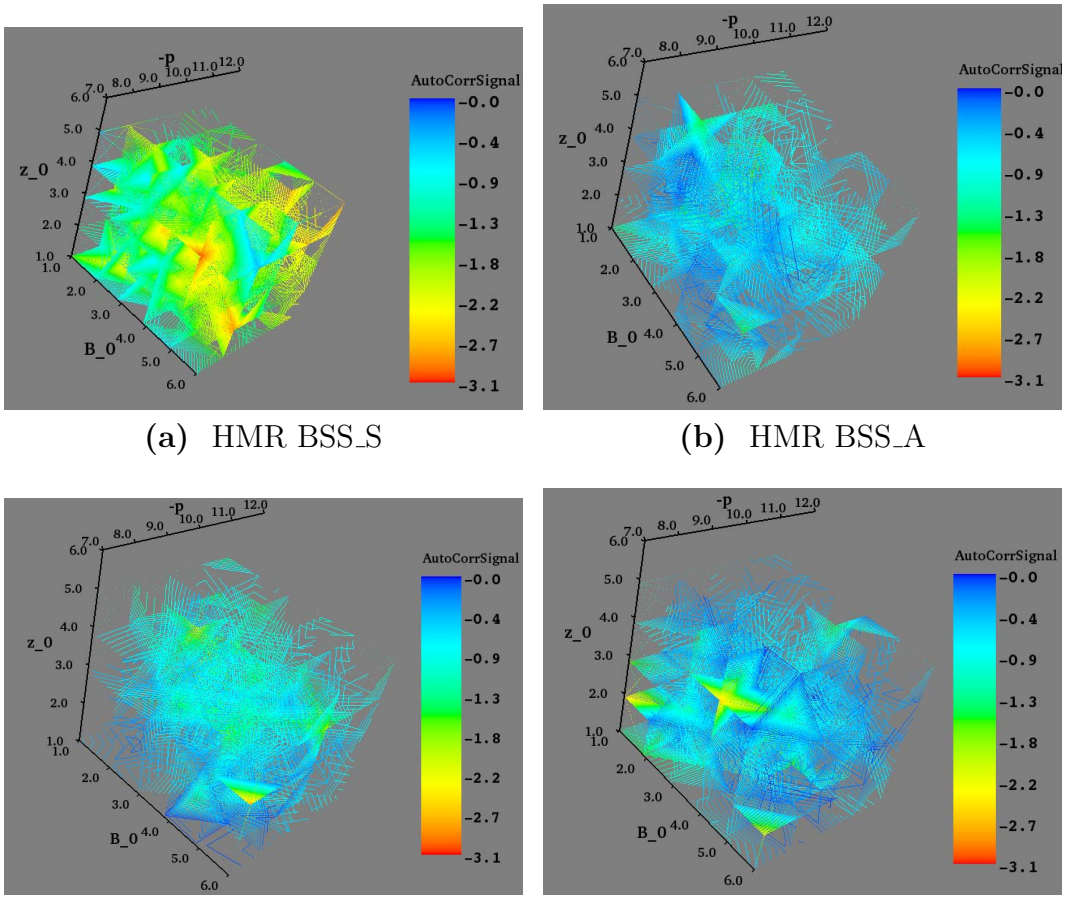

(a) HMR BSS_S **(b)** HMR BSS_A

(c) HMR ASS_S **(d)** HMR ASS_A

Figure 6.6 Autocorrelation signal in the parameter spaces of the models HMR BSS_S(A), HMR ASS_S(A) after backtracking of the measured arrival directions above 51.3 EeV. The units and names of the axes could be found in the Table 5.2.

If one adds the toroidal halo fields to the models above, it requires a scan over three additional parameters so that it becomes impossible to scan through all the combinations from the computation point of view. Nevertheless, the toroidal field has been tested for a special case. I use a typical toroidal field with the following values of the parameters: $B_0^H = 4\mu$G, $\rho_0^H = 6$kpc and $z_0^H = 2$ kpc. The values are chosen according to the results from the latest study of the rotation measures in [171], where these values are within one sigma interval from the best fit for any field symmetry as one can see from the Table 2 in [171]. The results for the pair ratios and autocorrelation signal are represented on Figures A.2 and A.3 respectively. As one can see, the toroidal field increases focusing for particular points of the parameter space. The maxima of the pair ratios, approximately four-fold increase in the number of pairs per 6 degree angular window, happens at (B_0,p,z_0)=(4 μG,-8°,3 kpc), (5 μG,-8°,5 kpc), (3 μG,-7°,3 kpc) and (4 μG,-10°,5 kpc) for BSS_S, BSS_A, ASS_S and ASS_A correspondingly. The autocorrelation signal global minima correspond to the above points of the pair ratio maxima for the BSS_S and ASS_S models and equal to $\log_{10}(0.00073)$=-3.1 and $\log_{10}(0.0009)$=-3.0 correspondingly which is better than the 3σ deviation from the isotropic expectation. On the other hand, the minimum of the ASS_A model does not coincide with the pair ratio maximum and it equals $\log_{10}(0.0087)$=-2.1, not a 3σ level, and the signal at (4 μG,-10°,5 kpc) is equal to $\log_{10}(0.068)$=-1.2. Thus, ASS_A symmetry does not have any candidate models that strongly favor clustering. There is no coincidence between the autocorrelation minimum and pair ratio maximum for the BSS_A version as well, so it is not favorable either.

The results for the Sun et al. model do not show any significant focusing in the pair ratio, nor was there a pronounced minimum in the autocorrelation signal. There is no global maximum for the pair ratio since it is degenerate for a number

of points of the parameter space, but it does not exceed 1.3 for any of them. The autocorrelation signal also has many regions in parameter space with close values — the lowest one being $\log_{10}(0.0038)$=-2.4 for (B_0,p,ρ_c,ρ_0,z_0)=(3 μG, -12°, 6 kpc, 12 kpc, 1kpc). The field has also been tested with addition of the toroidal halo field. Again, computational time restrictions dictated me to analyze only a specific case: the disk field parameters had fixed values at (B_0,p,ρ_c,ρ_0,z_0)=(2 μG, -12°, 5 kpc, 10 kpc, 1kpc) and were taken from [154], whereas two of the parameters, B_0^H and z_0^H, varied in the limits given in the table 5.2, and ρ_0^H was fixed at 6 kpc. The results do not reveal any "hot spots" in the parameter space of both the pair ratios and autocorrelation signals, as one can see on Figure A.4.

Finally, the results of the scans in the parameter space of the Vallée model show practically no focusing with the pair ratio close to unity for all points and no significant autocorrelation function either. Figure A.5 depicts this fact clearly.

6.4.1 Error Propagation from Energy Resolution

A question arises about the stability of the results from the previous section with respect to the energy resolution. It is even more important in the case of the back-tracking since now it is not merely a matter of the order of the events in the list as it was described in the Section 6.2 since the propagation of each cosmic ray depends on its energy. I use the same approach as in Section 6.2, i.e. using the individual energy resolutions to produce 100 datasets where the energies of the events are now distributed according to a gaussian of width equal to the energy resolution. The same number of events is maintained in each dataset which can shift the lowest energy for some of them below the nominal 51.3 EeV cut.

It is practically impossible to do the checks on all of the points of the parameter spaces of all models. I do the estimate of the spread of the autocorrelation signal only

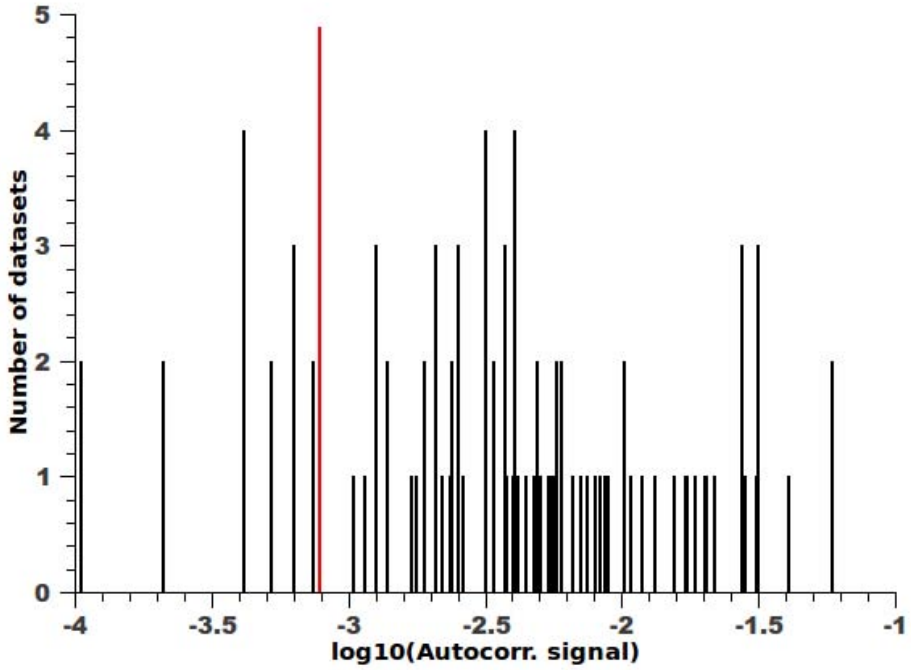

Figure 6.7 Spread in the autocorrelation signal due to the finite energy resolution for HMR BSS_S model and toroidal halo field with the following parameters: (B_0,p,z_0)=(4 μG,-8°,3 kpc) of the HMR BSS_S model with the toroidal field of $B_0^H = 4\mu$G, $\rho_0^H = 6$kpc and $z_0^H = 2$ kpc. The red line shows the value of the autocorrelation signal for the real dataset. The total number of datasets used is 100 but 3 of them are not included in this histogram since they gave the autocorrelation of 0 and could not be plotted in the logarithmic scale.

for the points of the global minima of the autocorrelation signal for different models. The spread of the autocorrelation signal is shown on Figure 6.7 for the HMR BSS_S model with the toroidal field. This spread affects the position of the maximum for the pair ratio. I take the dataset corresponding to the highest autocorrelation signal (meaning it is the closest to isotropy) in Figure 6.7 and then calculate the pair ratios in order to see how the field focusing properties change. The global maximum of the pair ratio remains at the same field parameters with its value reduced however. On the other hand, another point with a pair ratio value very close to the maximum

appears at (B_0,p,z_0)=(3 μG,-8°,4 kpc). The values of the pair ratios for the two points are 2.07 and 2.05, correspondingly, so we observe that the energy spread makes the region of favorable models to include some of adjacent points of the parameter space.

6.4.2 True Significance Calculation

The results obtained above are based on the a priori selection of the angular window and energy cut obtained as a global minimum of the scan shown in Figure 6.2. As already mentioned above and shown in [177], the true significance, or the probability of obtaining a given autocorrelation signal by starting from an isotropic distribution, needs to be calculated. In the case of no magnetic field the procedure involves generating a large number of isotropic datasets and treating each of them in the same way as the real data by repeating the scan in energy cut and angular window. One then can count how many of the scans produce a global minimum of the autocorrelation signal with the same or smaller value than the value at the minimum for the real data. I extend this approach to include the galactic magnetic field.

The first step is to do the procedure described above on the Earth's sky. As one can see in the previous section, the best model candidates have an autocorrelation signal at a level of 3σ deviation from the isotropy. Hence, one can fix the number of scans with isotropic datasets equal to 10000[2] which would be enough to see true significance at the 3σ level. One saves 10000 datasets with the number of events corresponding to the energy cut at the global minimum of a particular scan and the corresponding angular window is saved as well. We treat each such dataset in exactly the same way as we treat the real data. So, once we have all isotropic datasets on the Earth's sky, we need to do the backtracking and see how many of them will give the same or better clustering on the extragalactic sky.

[2]the exact number of the datasets is 10032 due to computational reasons

The backtracking of each of the isotropic datasets is done through the same models that gave the best clustering and were discussed in the previous section. For each dataset and model we seek a global maximum of the pair ratio in the parameter space of the corresponding model, and it has to be larger than 1.0 as well to ensure enhancement of clustering on the extragalactic sky. The last step is then to calculate the autocorrelation signal for the pair ratio global maximum which is done by backtracking of 10^5 isotropic realizations in the exact same way as was described in section 6.4. Finally, we calculate the fraction of the cases out of the total 10000 where the autocorrelation signal is the same or smaller than the signal produced by the real dataset. The fraction represents the true statistical significance of the results. The values of the true significance are shown in the next section along with the overall conclusions.

6.5 Conclusions

Using a two-point cumulative autocorrelation function, I analyzed different models of the galactic magnetic field with regard to their ability to focus backtracked UHECR. The models that favor such clustering have a global maximum of the pair ratio value in their parameter space, and have been checked against isotropy to make sure that the clustering is above that expected from the isotropic case. The model candidates along with the corresponding pair ratio and logarithm of the autocorrelation signal are summarized in Table 6.1. The BSS_S symmetry of the HMR model is favored in general in the case of the pure spiral disk fields. Addition of the toroidal halo field enhances clustering so that two field models are favorable in this case, both being HMR models with BSS_S and ASS_S symmetries. Thus, the vertical odd field symmetry of the spiral field is rejected by the data. The models with annular structure such as

Sun et al. and Vallée are not favored. The results of the astronomical observations,

Table 6.1 Favorable Models of the Galactic Magnetic Field

Model name	Favored parameters	Pair ratio from data	$\log_{10}$(Autocorr. signal) from data	True significance (%)
HMR BSS_S	(B_0,p,z_0)=(5 μG,-7°,4 kpc)	1.8	-3.0	2.5
HMR BSS_S + toroidal halo	(B_0,p,z_0)=(4 μG,-8°,3 kpc)	4.0	-3.1	2.5
HMR ASS_S + toroidal halo	(B_0,p,z_0)=(3 μG,-7°,3 kpc)	3.9	-3.0	5.3

and especially the latest results from the rotation measure surveys described in [171], suggest that the magnetic field of the Galaxy has a spiral structure in the disk and a toroidal halo field going in opposite azimuthal directions above and below the galactic plane. However, those measurements were unable to distinguish between "BSS" and "ASS" type of symmetries leaving both as possible candidates. The results of the current work show a clear difference between the "BSS" and "ASS" symmetries, with the BSS being preferable in the case of a pure disk field without a toroidal field. If one adds the toroidal halo field, the situation changes so that there are favorable candidates belonging to both classes of symmetries.

Recent studies mentioned above do not consider models with the odd vertical symmetry which is one of the possible solutions of the dynamo theory. In the case of the combined spiral and toroidal fields, there is degeneracy between BSS_S and ASS_S symmetries, but they both have even vertical symmetry (_S), and the odd symmetry is excluded. The ring models are disfavored by this work with and without addition

of toroidal fields.

The fifth column of the Table 6.1 gives the true statistical significance of the autocorrelation signal for the best models. Thus the pure spiral field of the BSS_S type and its modification with the toroidal field both show the same clustering with 2.5% (2.3σ) chance of being from an isotropic realization. The significance decreases for the ASS_S field with the toroidal field to 5.3% (2.0σ). The significance of the autocorrelation signal minimum and corresponding clustering of the arrival directions on the Earth's sky has been calculated too. For the Earth's sky the significance is 33.5% which is compatible with an isotropic distribution at 1σ level. This fact shows very strong focusing properties of the selected galactic field models. The models in Table 6.1, at their optimal parameter point, indicate the most clustering of all the models considered. As mentioned above, the method does not reference any source catalog.

Finally, Figures A.6, A.7 and A.8 show the sky maps of the measured Auger data arrival directions above 51.3 EeV at the Earth's sky, and after backtracking in Aitoff projection in the galactic coordinates. One needs to take into account that there could be many sky maps that look similar and have a lot of clustering, so that one cannot draw conclusions just by looking at such maps. The autocorrelation analysis above selected only those fields that give statistically significant clustering which excludes random lensing. On the other hand, once high statistical significance has been established for particular models from the Table 6.1, one can give physical interpretation to the corresponding sky maps.

Figure A.6 shows the resulting clustering for a pure spiral field, the BSS_S symmetry. One can see that most of the clustering happens in the region of the sky along the galactic longitude $l \approx -80^\circ$ and between the galactic latitudes $b \approx 20^\circ..60^\circ$. This region does not correspond to the position of the super-galactic plane, which goes

at galactic longitudes between $l \approx -40°..-60°$ in the same quadrant of the sky, and where the most of the extragalactic matter is situated within the GZK horizon, and is believed to be a possible source of extragalactic UHECRs. It does not coincide with the position of a very bright radiogalaxy Centaurus A either, which is located at a distance 3.8 Mpc, at $l \approx -50°$ and $b \approx 20°$. A deflection by a coherent extragalactic magnetic field (filamentary structure), which hasn't been considered in this work might be responsible for such a shift if the true source correlates with the matter.

The effect of adding the toroidal field is much more drastic on the backtracked directions. It makes most of the events cluster to the northern galactic hemisphere after backtracking so that the toroidal field acts as a "lens" (see Figures A.7 and A.8). For comparison, Figure A.9 shows the situation for BSS_A model with the toroidal field added so that one can see the difference between the effect of the field vertical symmetry. In this case the arrival directions are equally focused in both hemispheres and have less clustering in total, which explains the difference between even and odd vertical symmetries of the spiral field. These large deflections are explained by the fact that 4μG toroidal field directs backtracked protons to the central region of the spiral field, and then a very strong spiral field of these models make them deflect to much higher extent than one would typically assume for protons at these energies. The existence of a toroidal field is nevertheless strongly supported by the most recent surveys of rotation measure as described in the previous chapter, in [171].

The study described in this dissertation and other recent works [190, 191] that consider full three-dimensional structure of the galactic magnetic field and its effect on the propagation of the UHECR show that using cosmic ray data alone it is possible to constrain the galactic magnetic field in a way that is complimentary to the traditional astronomical observations both in terms of determining favorable parameters of the spiral field such as pitch angle, magnitude normalization, and selecting

symmetries of the field. The statistics and energy resolution are nevertheless not enough currently to select unambiguously the right model of the field with all its parameters determined. Future advances in observational instrumentation will solve the mysteries of the galactic magnetic field structure and origin of UHECRs. For example, the Square Kilometre Array [192] would allow for conducting an all-sky survey of rotation measures for 20000 pulsars and 20 million extragalactic polarized sources [193]. Planned JEM-EUSO mission [194] to detect UHECR fluorescence in the atmosphere by looking down from the International Space Station should be able to detect $\sim$1000 showers above 50 EeV in one year of operation drastically improving the statistics at these energies. Those type of measurements combined will allow for precise backtracking of the arrival directions of large UHECR dataset to reveal the positions of the true sources of the extragalactic UHECRs.

Bibliography

[1] S. Kirkham, *The ministry of beauty* (P. Elder and company, 1907).

[2] McLennan and Burton, Phys. Rev. **16,** 184 (1903).

[3] Rutherford and Cooke, Ibid. **16,** 183 (1903).

[4] V. Hess, *Nobel Lectures. Physics 1922-1941* (Elsevier Publishing Company, Amsterdam, 1965).

[5] R. A. Millikan, Proc. Natl. Acad. Sci. USA **12,** 48–55 (1926).

[6] Popular Science **129,** 134 (1936).

[7] J. Linsley, Phys. Rev. Lett. **10,** 146 (1963).

[8] M. M. Winn, J. Ulrichs, L. S. Peak, C. B. A. McCusker, and L. Horton, Journal of Physics G: Nuclear Physics **12,** 653 (1986).

[9] M. A. Lawrence, R. J. O. Reid, and A. A. Watson, Journal of Physics G: Nuclear and Particle Physics **17,** 733 (1991).

[10] A. V. Glushkov et al, JETP Lett. **85,** 163 (2007).

[11] N. Chiba et al, Nuclear Instruments and Methods in Physics Research Section A: Accelerators, Spectrometers, Detectors and Associated Equipment **311,** 338 – 349 (1992).

[12] D. J. Bird et al, Astrophysical Journal **424,** 491–502 (1994).

[13] R. U. Abbasi et al, Phys. Rev. Lett. **92,** 151101 (2004).

[14] http://www.auger.org/.

[15] The Telescope Array, "http://www.telescopearray.org/," (2008).

[16] W. Axford et al., *Proc. 15th ICRC (Plovdiv)*, (1977).

[17] J. Blümer, R. Engel, and J. R. Hörandel, "Cosmic rays from the knee to the highest energies," Progress in Particle and Nuclear Physics **63,** 293–338 (2009).

[18] E. Berezhko and L. Ksenofontov, JETP **89,** 391 (1999).

[19] K. Kobayakawa et al, Phys. Rev. D **66,** 083004 (2002).

[20] T. Stanev, P. Biermann, and T. Gaisser, Astronomy & Astrophysics **274,** 902 (1993).

[21] P. Biermann, N. Langer, E. Seo, and T. Stanev, Astronomy & Astrophysics 369 (2001).

[22] L. Sveshnikova et al., Astronomy & Astrophysics **409,** 799 (2003).

[23] S. Swordy, *Proc. 24th ICRC (Rome)*, (1995).

[24] A. Lagutin et al., Nucl. Phys. B (Proc. Suppl.) **97,** 267 (2001).

[25] V. Ptuskin et al., Astronomy & Astrophysics **268,** 1993 (726).

[26] S. Ogio and F. Kakimoto, *Proc. 28th ICRC (Tsukuba)*, (2003).

[27] R. Roulet, ArXiv Astrophysics e-prints , astro-ph/0310367.

[28] J. Hörandel, Astropart. Phys **21,** 2004 (241).

[29] J. Hörandel, Astropart. Phys **19,** 2003 (193).

[30] V. Berezinsky, S. Grigorieva, and B. Hnatuk, Astropart. Phys **21,** 617 (2004).

[31] V. Berezinsky, A. Gazizov, and S. Grigorieva, Phys. Lett. B. **612,** 147 (2005).

[32] J. F. Carlson and J. R. Oppenheimer, Phys. Rev. **51,** 220–231 (1937).

[33] W. Heitler, *Quantum Theory of Radiation*, 2nd ed. (Oxford University Press, 1944).

[34] B. Rossi and K. Greisen, Rev. Mod. Phys. **13,** 240–309 (1941).

[35] R. Engel, D. Heck, and T. Pierog, Annual Review of Nuclear and Particle Science **61,** 467–489 (2011).

[36] H. Barbosa, F. Catalani, J. Chinellato, and C. Dobrigkeit, Astroparticle Physics **22,** 159 – 166 (2004).

[37] R. Engel, D. Heck, and T. Pierog, Annual Review of Nuclear and Particle Science 61 (2011).

[38] C. Meurer, J. Blmer, R. Engel, A. Haungs, and M. Roth, Czechoslovak Journal of Physics **56,** A211–A219 (2006).

[39] A. Hillas, *Proc. 16th ICRC (Kyoto)*, 8 (1979).

[40] T. Stanev, *High Energy Cosmic Rays*, 2nd ed. (Springer, 2009).

[41] J. Matthews, Astropart. Phys. **22,** 387 (2005).

[42] F. Arqueros, J. R. Hoerandel, and B. Keilhauer, "Air Fluorescence Relevant for Cosmic-Ray Detection - Summary of the 5th Fluorescence Workshop, El Escorial 2007," NUCL.INSTRUM.METH.A **597,** 1 (2008).

[43] J. R. Patterson and A. M. Hillas, J. Phys. G: Nucl. Phys **9,** 1433 (1983).

[44] B. Antokhonov *et al.*, "TUNKA-133: A new array for the study of ultra-high energy cosmic rays," Bulletin of the Russian Academy of Sciences: Physics **75,** 367–370 (2011), 10.3103/S1062873811030075.

[45] J. Abraham et al., Science **318,** 939 (2007).

[46] J. Abraham et al, Astroparticle Physics **29,** 188 – 204 (2008).

[47] J. Abraham et al, Phys. Rev. Lett. **100,** 211101 (2008).

[48] P. Abreu et al, "Update on the correlation of the highest energy cosmic rays with nearby extragalactic matter," Astroparticle Physics **34,** 314 – 326 (2010).

[49] J. Abraham et al, Astroparticle Physics **31,** 399 – 406 (2009).

[50] K. Shinozaki et al, Astrophys. J. **571,** L117 (2002).

[51] M. Risse et al, Phys. Rev. Lett. **95,** 171102 (2005).

[52] G. Rubtsov et al, Phys. Rev. D **73,** 063009 (2006).

[53] M. Ave, J. A. Hinton, R. A. Vazquez, A. A. Watson, and E. Zas, Phys. Rev. Lett. **85,** 2244 (2000).

[54] M. Ave, J. A. Hinton, R. A. Vazquez, A. A. Watson, and E. Zas, Phys. Rev. D **65,** 063007 (2002).

[55] J. Abraham et al, "Upper limit on the cosmic-ray photon flux above above 10^{19} eV using the surface detector of the Pierre Auger Observatory," Astroparticle Physics **29,** 243 – 256 (2008).

[56] G. Gelmini, O. Kalashev, and D. V. Semikoz, JCAP 11 (2007).

[57] G. Gelmini, O. Kalashev, and D. V. Semikoz, , astro-ph/0506128.

[58] J. Ellis, V. E. Mayes, and D. V. Nanopoulos, "Ultrahigh-energy cosmic rays particle spectra from crypton decays," Phys. Rev. D **74,** 115003 (2006).

[59] M. Risse and P. Homola, Mod. Phys. Lett. A **22,** 749 (2007).

[60] E. Fermi, Phys. Rev. **75,** 1169 (1949).

[61] P. O. Lagage and C. J. Cesarsky, Astronomy & Astrophysics **118,** 223–228 (1983).

[62] E. G. Berezhko, Astroparticle Physics **5,** 367–378 (1996).

[63] A. M. Hillas, Ann. Rev. Astron. Astrophys. **22,** 425 (1984).

[64] S. Hümmer, M. Maltoni, W. Winter, and C. Yaguna, Astroparticle Physics **34,** 205 (2010).

[65] J. P. Rachen and P. L. Biermann, Astronomy and Astrophysics **272,** 161 (1993).

[66] P. L. Biermann and P. A. Strittmatter, ApJ **322,** 643 (1987).

[67] L. Drury, Reports on Progress in Physics **46,** 973 (1983).

[68] F. Halzen and E. Zas, Astrophysical Journal **488,** 669 (1997).

[69] C. A. Norman, D. B. Melrose, and A. Achterberg, ApJ **454,** 60 (1995).

[70] A. A. Penzias and R. Wilson, Astrophysical Journal **142,** 419 (1965).

[71] D. Allard and R. J. Protheroe, Astronomy & Astrophysics **502,** 803 (2009).

[72] J. Abraham et al, Phys. Rev. Lett. **104,** 091101 (2010).

[73] G. T. Zatsepin and V. A. Kuzmin, Sov. Phys. JETP Lett. **4,** 78 (1966).

[74] K. Greisen, Phys. Rev. Lett. **16,** 748 (1966).

[75] D. J. Fixsen, E. S. Cheng, J. M. Gales, J. C. Mather, R. A. Shafer, and E. L. Wright, The Astrophysical Journal **473,** 576 (1996).

[76] C. L. Bennett *et al.*, ApJ **583,** 1 (2003).

[77] G. Hinshaw *et al.*, The Astrophysical Journal Supplement Series **180,** 225 (2009).

[78] V. S. Berezinskii and S. I. Grigor'eva, Astron. Astrophys. **199,** 1 (1988).

[79] S. Yoshida and M. Teshima, Progress of Theoretical Physics **89,** 833 (1993).

[80] Astroparticle Physics **4,** 253 (1996).

[81] J. Abraham et al, Nuclear Instruments and Methods in Physics Research Section A: Accelerators, Spectrometers, Detectors and Associated Equipment **613,** 29 – 39 (2010).

[82] J. Abraham et al, "The fluorescence detector of the Pierre Auger Observatory," Nuclear Instruments and Methods in Physics Research Section A: Accelerators, Spectrometers, Detectors and Associated Equipment **620,** 227 – 251 (2010).

[83] http://www.google.com/earth/index.html.

[84] X. Bertou, P. S. Allison, C. Bonifazi, P. Bauleo, C. M. Grunfeld, M. Aglietta, F. Arneodo, D. Barnhill, and J. J. Beatty, Nucl. Instr. and Meth. A **568,** 839 – 846 (2006).

[85] http://www.telescope-optics.net/Schmidt-camera.htm.

[86] M. A. L. de Oliveira, V. de Souza, H. C. Reis, and R. Sato, "Manufacturing the Schmidt corrector lens for the Pierre Auger Observatory," Nuclear Instruments

and Methods in Physics Research Section A: Accelerators, Spectrometers, Detectors and Associated Equipment **522,** 360 – 370 (2004).

[87] H. J. Mathes, "The HEAT telescopes of the Pierre Auger Observatory: status and first data," *Proc. of the 32th ICRC (Beijing)*, (2011).

[88] F. Sánchez, "The AMIGA detector of the Pierre Auger Observatory: an overview," *Proc. of the 32th ICRC (Beijing)*, (2011).

[89] G. A. Askaryan, Sov. Phys. JETP **14,** 441 (1962).

[90] G. A. Askaryan, Sov. Phys. JETP **48,** 988 (1965).

[91] H. Falcke et al., Nature **435,** 313 (2005).

[92] D. Ardouin et al., Nucl. Instr. Meth. **A555,** 148 (2005).

[93] J. L. Kelley, "AERA: the Auger Engineering Radio Array," *Proc. 32th ICRC (Beijing)*, (2011).

[94] F. Salamida, "Update on the measurement of the CR energy spectrum above 10^{18} eV made using the Pierre Auger Observatory," *Proc. 32th ICRC (Beijing)*, (2011).

[95] D. F. San Luis, "The distribution of shower maxima of UHECR air showers," *Proc. 32th ICRC (Beijing)*, (2011).

[96] P. Abreu et al, Astroparticle Physics **34,** 627 – 639 (2011).

[97] M.-P. Véron-Cetty and P. Véron, "A catalogue of quasars and active nuclei: 12th edition," Astron. Astrophys. **455,** 773–777 (2006).

[98] J. Abraham et al, Science **318,** 938 – 943 (2007).

[99] J. Abraham et al., Phys. Rev. D **79,** 102001 (2009).

[100] J. Abraham et al., Astroparticle Physics **33,** 108 – 129 (2010).

[101] J. A. J. Matthews, "Optical Calibration of the Auger Fluorescence Telescopes," *SPIE Astronomical Telescopes and Instrumentation*, (2003).

[102] P. Bauleo et al., "Absolute calibration of the Auger fluorescence detectors," *Proc. 29th ICRC (Pune)*, (2005).

[103] R. Knapik, "The Absolute, Relative and Multi-Wavelength Calibration of the Pierre Auger Observatory Fluorescence Detectors," *Proc. 30th ICRC (Merida)*, (2007).

[104] R. Knapik, Ph.D. thesis, Colorado State University, 2009.

[105] J. Brack et al., "Auger Fluorescence Detector Absolute Calibration, January and June 2010," Internal GAP note of the Pierre Auger Collaboration (2011), http://www.auger.org/admin/GAP_Notes/GAP2010/GAP2010_118.pdf.

[106] D. Kuempel, K. H. Kampert, and M. Risse, Astroparticle Physics **30,** 167 – 174 (2008).

[107] C. Bonifazi, Nuclear Physics B - Proceedings Supplements **190,** 20 – 25 (2009).

[108] M. Unger, B. R. Dawson, R. Engel, F. Schssler, and R. Ulrich, Nuclear Instruments and Methods in Physics Research Section A: Accelerators, Spectrometers, Detectors and Associated Equipment **588,** 433 – 441 (2008).

[109] T. K. Gaisser and A. M. Hillas, *Proc. of the 15th ICRC*, (1977).

[110] Z. Cao et al, *Proc. of the 28th ICRC*, (2003).

[111] H. M. J. Barbosa, F. Catalani, J. A. Chinellato, and C. Dobrigkeit, Astroparticle Physics **22,** 159 – 166 (2004).

[112] A. M. Hillas, Acta Phys. Acad. Sci. Hung. **29,** 355 (1970).

[113] D. Newton, Astropart. Phys. **26,** 414 (2007).

[114] K. Kamata and J. Nishimura, Progress of Theoretical Physics Supplement **6,** 93–155 (1958).

[115] K. Greisen, *Progress in Cosmic Ray Physics*, 3 (1956).

[116] T. P. A. Collaboration, "The Pierre Auger Observatory I: The Cosmic Ray Energy Spectrum and Related Measurements," (2011), http://arxiv.org/abs/1107.4809.

[117] N. G. Busca, Ph.D. thesis, The University of Chicago, 2006.

[118] T. P. A. Collaboration, "The Pierre Auger Observatory III: Other Astrophysical Observations," (2011), http://arxiv.org/abs/1107.4805.

[119] L. Pasquini, P. Bonifacio, S. Randich, D. Galli, and R. G. Gratton, Astronomy & Astrophysics **426,** 651 (2004).

[120] R. M. Kulsrud and E. G. Zweibel, Rep. Prog. Phys. **71,** 1 (2008).

[121] E. Parker, ApJ **163,** 255 (1971).

[122] E. Parker, ApJ **163,** 279 (1971).

[123] S. Vainshtein and A. A. Ruzmaikin, Sov. Astron. **16,** 365 (1972).

[124] R. M. Kulsrud, Lect. Notes Phys. **664,** 69 (2005).

[125] R. M. Kulsrud, Annu. Rev. Astro. Astrophys. **37,** 37 (1999).

[126] R. J. Goldston and P. H. Rutherford, *Introduction to plasma physics* (CRC Press, 1995).

[127] A. M. Ruzmaikin, A. A. Shukurov and D. D. Sokoloff, *Magnetic Fields of Galaxies* (Kluwer Academic Publishers, 1988).

[128] A. M. Howard and R. Kulsrud, Astrophysical Journal **483,** 648 (1997).

[129] L. Biermann, Naturforsch **5a,** 65 (1950).

[130] R. Kulsrud and S. Anderson, ApJ **396,** 606 (1992).

[131] R. Kulsrud, R. Cen, J. P. Ostriker, and D. Ryu, ApJ **480,** 481 (1997).

[132] J. S. Hall, Science **109,** 166 (1949).

[133] L. Davis and J. L. Greenstein, ApJ **114,** 206 (1951).

[134] E. M. Purcell, in *in The Dusty Universe*, G. B. Field and A. G. W. Cameron, eds., (N. Watson Academic Press, New York, 1975).

[135] R. Wielebinski, J. R. Shakeshaft, and I. I. K. Pauliny-Toth, The Observatory **82,** 158 (1962).

[136] B. Burke and F. Graham-Smith, *An Introduction to Radio Astronomy* (Cambridge University Press, 2009).

[137] D. R. Lorimer and M. Kramer, *Handbook of Pulsar Astronomy* (Cambridge observing handbooks for research astronomers, Vol. 4. Cambridge, UK, 2004).

[138] C. Heiles, ApJ **462,** 316 (1996a).

[139] D. S. Mathewson and V. L. Ford, MmRAS **74,** 139 (1970).

[140] R. N. Manchester, ApJ **172,** 43 (1972).

[141] R. N. Manchester, ApJ **188,** 637 (1974).

[142] R. C. Thomson and A. H. Nelson, MNRAS **191,** 863 (1980).

[143] C. C. Lin and F. H. Shu, ApJ **140,** 646 (1964).

[144] C. C. Lin and F. H. Shu, Proc. Natl. Acad. Sci. **140,** 229 (1966).

[145] M. J. Reid et al., ApJ **700,** 137 (2009).

[146] P. A. Hamilton and A. G. Lyne, MNRAS **224,** 1073 (1987).

[147] A. G. Lyne and F. G. Smith, MNRAS **237,** 533 (1989).

[148] R. J. Rand and A. G. Lyne, MNRAS **268,** 497 (1994).

[149] J. M. Weisberg et al., ApJS **150,** 317 (2004).

[150] J. L. Han, R. N. Manchester, and G. J. Qiao, MNRAS **306,** 371 (1999).

[151] J. L. Han and R. Wielebinski, Chinese J. Astron. Astrophys. **2,** 293 (2002).

[152] J. L. Han et al., ApJ **642,** 868 (2006).

[153] J. P. Valle, ApJ **619,** 297 (2005).

[154] X. H. Sun, W. Reich, A. Waelkens, and T. A. Enlin, Astronomy & Astrophysics **477,** 573 (2008).

[155] R. Jansson et al., JCAP07 **2009,** 21 (2009).

[156] L. Page et al., ApJS **170,** 335 (2007).

[157] M. A. Miville-Deschnes et al., Astronomy & Astrophysics **490,** 1093 (2009).

[158] G. Gilmore and N. Reid, MNRAS **202,** 1025 (1983).

[159] J. H. Taylor, R. N. Manchester, and A. G. Lyne, ApJS **88,** 529 (1993).

[160] G. J. Qiao, R. N. Manchester, A. G. Lyne, and G. D. M., MNRAS **274,** 572 (1995).

[161] J. L. Han and G. J. Qiao, Astronomy & Astrophysics **288,** 759 (1994).

[162] D. Morris and G. L. Berge, ApJ **139,** 1388 (1964).

[163] R. R. Andreassian, Astrofizika **16,** 407 (1980).

[164] R. R. Andreassian and A. N. Makarov, Astrofizika **28,** 419 (1988).

[165] J. Navarro, R. N. Manchester, J. S. Sandhu, S. Kulkarni, and M. Bailes, ApJ **486,** 1019 (1997).

[166] N. W. Broten, J. M. Macleod, and J. P. Valle, Ap&SS **141,** 303 (1988).

[167] J. L. Han, R. N. Manchester, E. M. Berkhuijsen, and R. Beck, Astronomy & Astrophysics **322,** 98 (1997).

[168] M. Prouza and R. Šmída, Astronomy & Astrophysics **410,** 1 (2003).

[169] A. R. Taylor, J. M. Stil, and C. Sunstrum, ApJ **702,** 1230 (2009).

[170] S. A. Mao et al., ApJ **714,** 1170 (2010).

[171] M. S. Pshirkov, P. G. Tinyakov, P. P. Kronberg, and K. J. Newton-McGee, arXiv:1103.0814v2 (2011).

[172] P. P. Kronberg and K. J. Kronberg, Publications of the Astronomical Society of Australia **28,** 171 (2011).

[173] T. Stanev, ApJ **479,** 290 (1997).

[174] D. Harari, S. Mollerach, and E. Roulet, JHEP **9908,** 22 (1999).

[175] P. Peebles, *The large-scale structure of the universe*, *Princeton series in physics* (Princeton University Press, 1980).

[176] M. Takeda et al, The Astrophysical Journal **522,** 225 (1999).

[177] C. B. Finley and S. Westerhoff, Astroparticle Physics **21,** 359 – 367 (2004).

[178] J. Abraham et al, Phys. Rev. Lett. **101,** 061101 (2008).

[179] D. Ryu, H. Kang, and P. L. Biermann, "Cosmic magnetic fields in large scale filaments and sheets," Astronomy and Astrophysics **335,** 19–25 (1998).

[180] D. Ryu, H. Kang, J. Cho, and S. Das, "Turbulence and Magnetic Fields in the Large-Scale Structure of the Universe," Science **320,** 909–912 (2008).

[181] G. Tanco, "Cosmic Magnetic Fields from the Perspective of Ultra-High-Energy Cosmic Rays Propagation," in *[Without Title]*, Vol. 576 of *Lecture Notes in Physics* (Springer Berlin / Heidelberg, 2001), p. 155.

[182] A. Achterberg et al, "Intergalactic Propagation of the UHE cosmic rays," (1999), astro-ph/9907060.

[183] N. Hayashida et al, (2000), astro-ph/0008102.

[184] M. Ave, P. Ghia, A. Grillo, S. Mollerach, and D. Semikoz, "Search for clustering of ultra high energy cosmic rays from the Pierre Auger Observatory," Internal GAP note of the Pierre Auger Collaboration (2008), http://www.auger.org/admin/GAP_Notes/GAP2008/GAP2008_015.pdf.

[185] M. S. Sutherland, B. M. Baughman, and J. J. Beatty, Astroparticle Physics **34,** 198 (2010).

[186] M. S. Sutherland, B. M. Baughman, and J. J. Beatty, "CRT: A Numerical Tool for Propagating Ultra High Energy Cosmic Rays through Magnetic Field Models," Internal GAP note of the Pierre Auger Collaboration (2010), http://www.auger.org/admin/GAP_Notes/GAP2008/GAP2008_099.pdf.

[187] *Numerical Recipes*, 3rd ed. (New York: Cambridge, 2007).

[188] http://www.vtk.org/.

[189] http://mayavi.sourceforge.net/.

[190] M. S. Sutherland, "A method for establishing constraints on galactic magnetic field models using ultra high energy cosmic rays and results from the data of the Pierre Auger Observatory,", 2010.

[191] M. S. Sutherland, "Back-tracking studies of the arrival directions of UHECR detected by the Pierre Auger Observatory," ArXiv Astrophysics e-prints , http://arxiv.org/abs/1107.4805.

[192] http://www.skatelescope.org/the-science/ska-key-science-projects/magnetism/.

[193] R. Beck, "Measurements of Cosmic Magnetism with LOFAR and SKA,", http://www.mpifr-bonn.mpg.de/staff/rbeck/ursi.pdf.

[194] http://jemeuso.riken.jp/en/index.html.

Appendix A

Extra figures

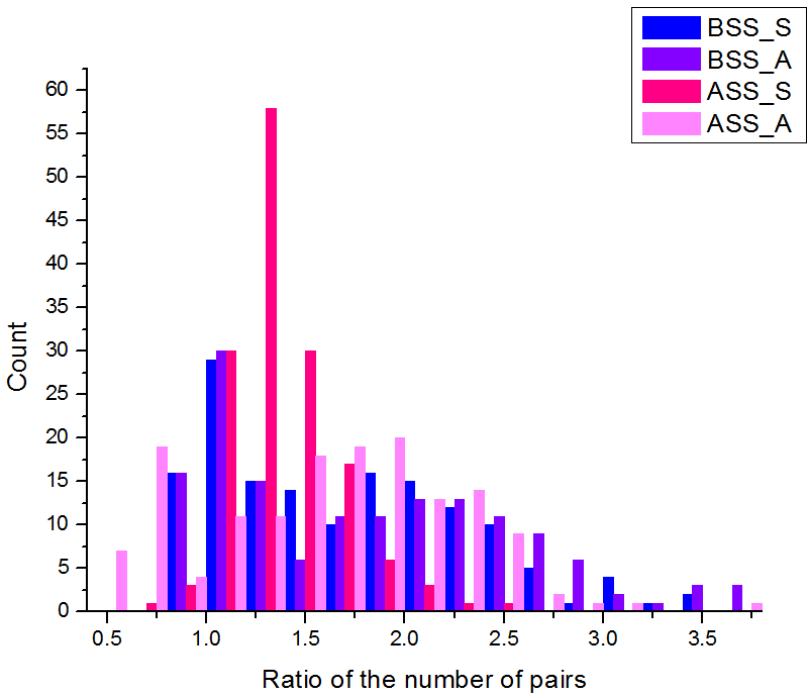

Figure A.1 Distribution of the ratio of the number of pairs for HMR BSS_S(A), HMR ASS_S(A)

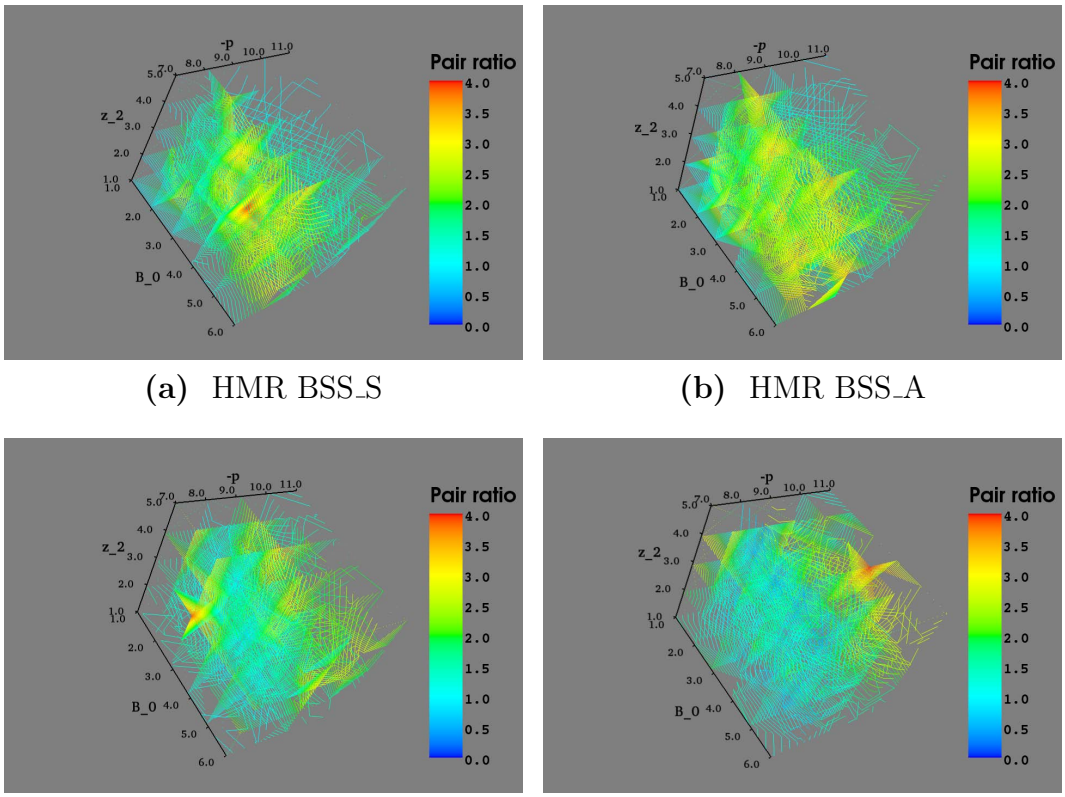

(a) HMR BSS_S **(b)** HMR BSS_A

(c) HMR ASS_S **(d)** HMR ASS_A

Figure A.2 Ratios of the number of pairs for each point in the phase spaces of the models HMR BSS_S(A), HMR ASS_S(A) + toroidal halo field with $B_0^H = 4\mu$G, $\rho_0^H = 6$kpc and $z_0^H = 2$ kpc before and after backtracking. The units and names of the axes could be found in the Table 5.2.

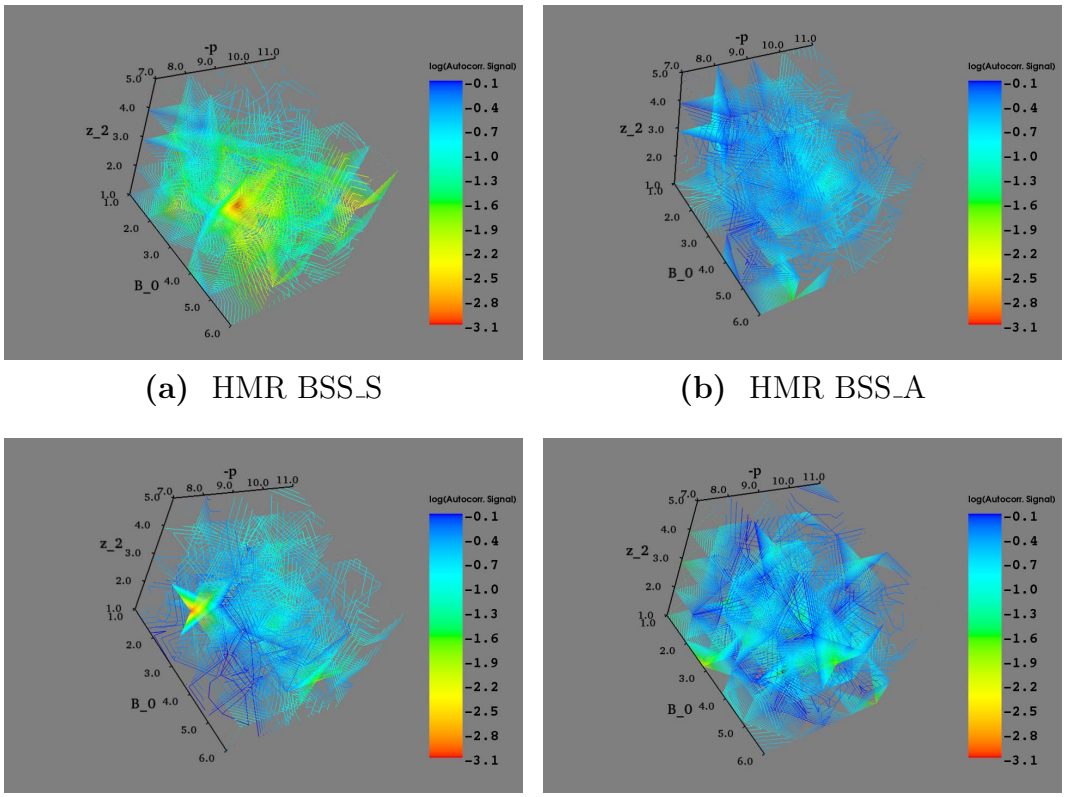

(a) HMR BSS_S **(b)** HMR BSS_A

(c) HMR ASS_S **(d)** HMR ASS_A

Figure A.3 Autocorrelation signal for each point in the phase spaces of the models HMR BSS_S(A), HMR ASS_S(A) + toroidal halo field with $B_0^H = 4\mu$G, $\rho_0^H = 6$kpc and $z_0^H = 2$ kpc after backtracking. The units and names of the axes could be found in the Table 5.2.

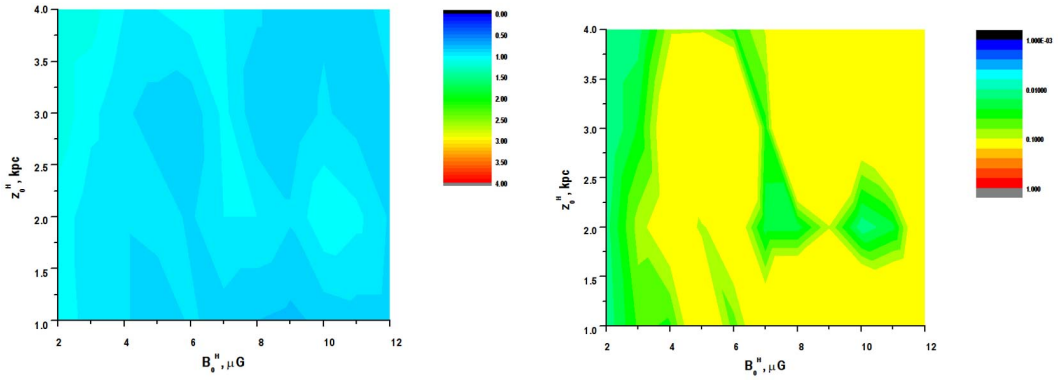

(a) Pair ratio **(b)** Autocorrelation signal

Figure A.4 Pair ratio and autocorrelation signal for each point in the phase spaces of the Sun et al. + toroidal halo field model where the scan has been done on B_0^H and z_0^H parameters of the toroidal field only. The profile is featureless and close to 1.0 for the pair ratio, and it also does not have any significant deviations from the isotropic distribution.

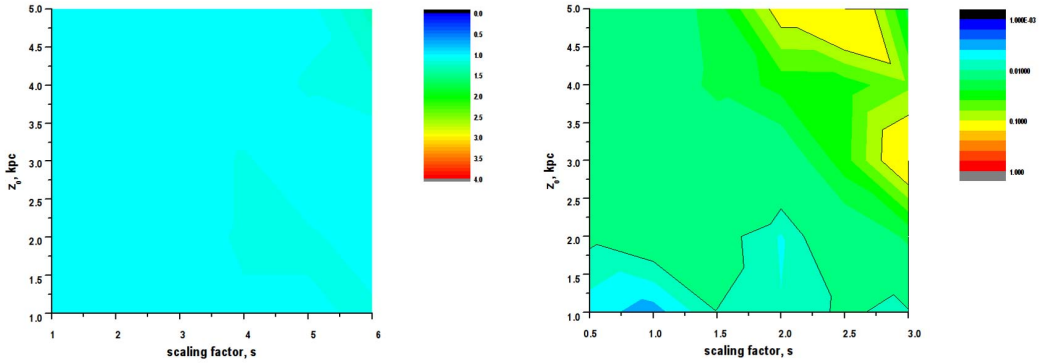

(a) Pair ratio **(b)** Autocorrelation signal

Figure A.5 Pair ratio and autocorrelation signal for each point in the phase spaces of the Vallée model. The profile is featureless and close to 1.0 for the pair ratio, and it also does not have any significant deviations from the isotropic distribution. The scaling factor of s=1.0 corresponds to the nominal values for this model as shown in the table 5.1.

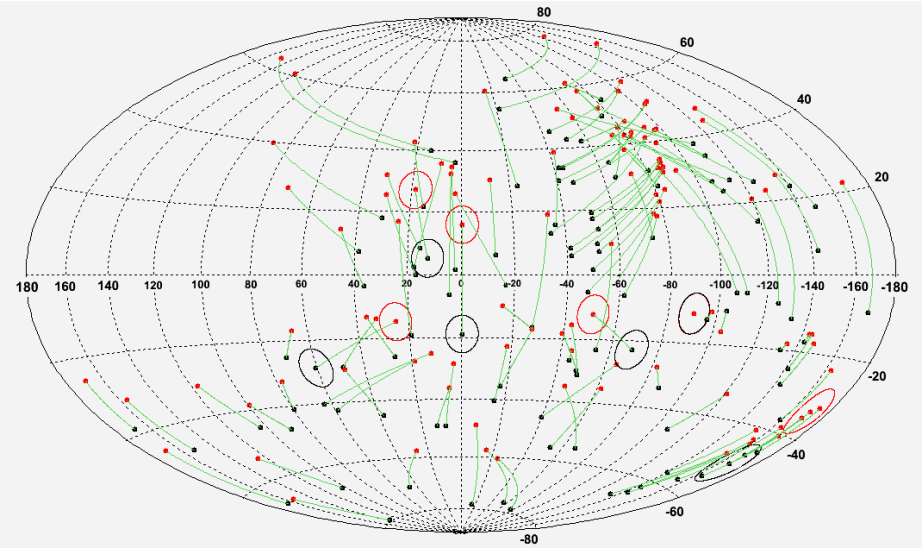

Figure A.6 Sky map in galactic coordinates of the measured Auger data arrival directions above 51.3 EeV at the Earth's sky (black) and after backtracking (red) in the BSS_S model with (B_0,p,z_0)=(5 μG,-7°,4 kpc). Pair ratio is 69/39 = 1.8. Angular windows of 6° are drawn around some observed and backtracked directions just to remind their size on the sky.

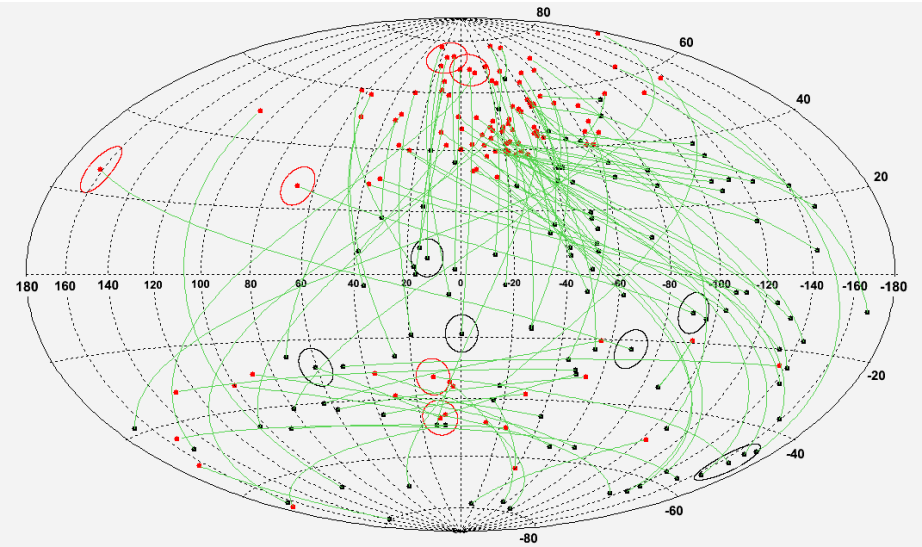

Figure A.7 Sky map in galactic coordinates of the measured Auger data arrival directions above 51.3 EeV at the Earth's sky (black) and after backtracking (red) in the BSS_S model with (B_0,p,z_0)=(4 μG,-8°,3 kpc) + toroidal halo field with $B_0^H = 4\mu$G, $\rho_0^H = 6$kpc and $z_0^H = 2$ kpc. Pair ratio is 156/39 = 4.0. Angular windows of 6° are drawn around some observed and backtracked directions just to remind their size on the sky.

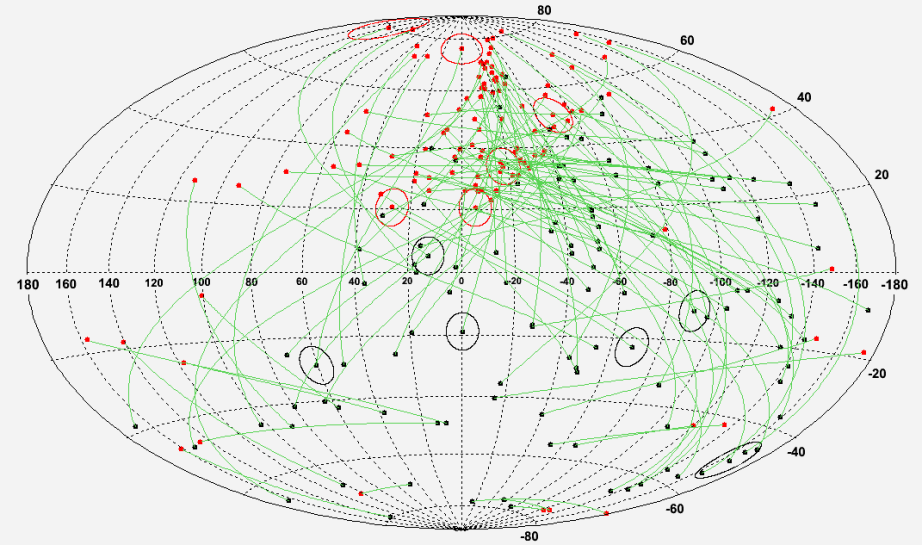

Figure A.8 Sky map in galactic coordinates of the measured Auger data arrival directions above 51.3 EeV at the Earth's sky (black) and after backtracking (red) in the ASS_S model with (B_0,p,z_0)=(3 μG,-7°,3 kpc) + toroidal halo field with $B_0^H = 4\mu$G, $\rho_0^H = 6$kpc and $z_0^H = 2$ kpc. Pair ratio is 152/39 = 3.9. Angular windows of 6° are drawn around some observed and backtracked directions just to remind their size on the sky.

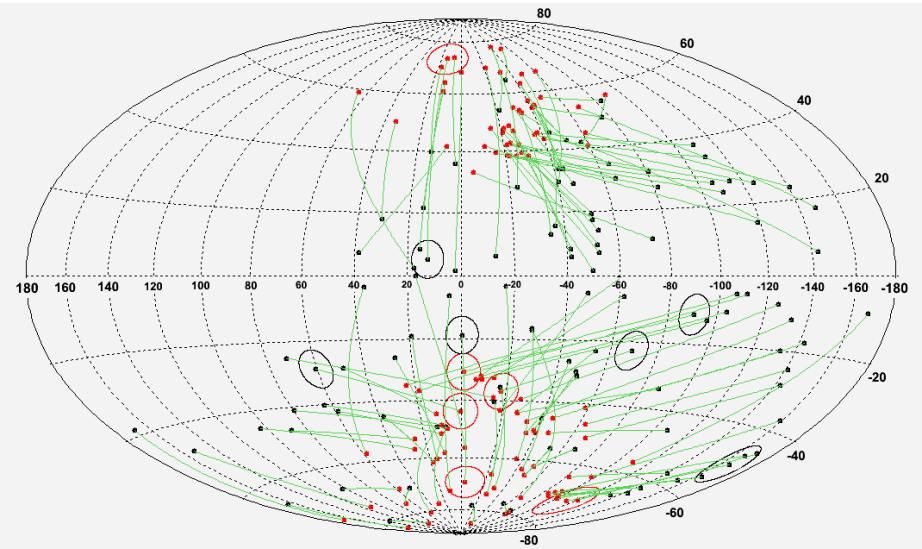

Figure A.9 Sky map in galactic coordinates of the measured Auger data arrival directions above 51.3 EeV at the Earth's sky (black) and after backtracking (red) in the BSS_A model with (B_0,p,z_0)=(4 μG,-8°,3 kpc) + toroidal halo field with $B_0^H = 4\mu$G, $\rho_0^H = 6$kpc and $z_0^H = 2$ kpc. Angular windows of 6° are drawn around some observed and backtracked directions just to remind their size on the sky.